Detection and Characterization of Transiting Giant Planets around Evolved Stars

A thesis submitted in partial fulfillment of
the requirements for the degree of

Doctor of Philosophy

by

Akanksha Khandelwal

(Roll No. 18330001)

Under the supervision of

Dr. Abhijit Chakraborty

Professor

Astronomy and Astrophysics Division

Physical Research Laboratory, Ahmedabad, India.

DEPARTMENT OF PHYSICS

INDIAN INSTITUTE OF TECHNOLOGY GANDHINAGAR

2023

Dedicated to my beloved family...

DECLARATION

I, **Akanksha Khandelwal (Roll No: 18330001)**, hereby declare that, this thesis titled **"Detection and Characterization of Transiting Giant Planets around Evolved Stars"** submitted to Indian Institute of Technology Gandhinagar towards the partial requirement of **Doctor of Philosophy** in **Physics** is an original work carried out by me under the supervision of **Prof. Abhijit Chakraborty** at Physical Research Laboratory, Ahmedabad, India. I have sincerely tried to uphold the academic ethics and honesty. Whenever an external information or statement or result is used, every effort is made to indicate this clearly, with due reference to the literature.

Name: Akanksha Khandelwal

(Roll No: 18330001)

CERTIFICATE

This is to certify that the work contained in the thesis titled **"Detection and Characterization of Transiting Giant Planets around Evolved Stars"** submitted by **Akanksha Khandelwal (Roll No: 18330001)** to Indian Institute of Technology, Gandhinagar has been carried out under my supervision at the Astronomy & Astrophysics Division, Physical Research Laboratory, Ahmedabad and it has not been submitted elsewhere for the award of any degree.

Dr. Abhijit Chakraborty

(Thesis Supervisor)

Senior Professor

Astronomy & Astrophysics Division

Physical Research Laboratory

Navarangpura, Ahmedabad, India

Acknowledgements

I am filled with joy and gratitude as I complete this thesis, reflecting on the journey that began five years ago. Many people have supported me along the way, and I want to express my heartfelt thanks to each of them.

First and foremost, I want to thank my family for supporting my decision to pursue a Ph.D., even though it meant moving out of my home city, a very first in my family. Their love and encouragement have been my pillars of strength. I am truly grateful to my Thesis supervisor Prof. Abhijit Chakraborty for guiding me and helping me grow as an independent researcher. His constant support throughout my Ph.D. years, and without his cooperation, completing this thesis would not have been possible. I am grateful for his encouragement to interact and collaborate with experts. I also want to especially thank Dr. Priyanka Chaturvedi and Rishikesh Sharma for being like mentors, always there to help and discuss ideas during my Ph.D. journey. I am incredibly grateful for their assistance in navigating a completely new subject during my research. Their encouragement and belief in my work have been a driving force behind the completion of this thesis. To the doctoral studies committee (DSC) members, Dr. Arvind Singh Rajpurohit, Dr. Veeresh Singh, and Prof. Kuljeet Kaur Marhas, thank you for your valuable feedback during the half-yearly meetings. It has been truly helpful. I am sincerely thankful to Dr. Arvind Singh Rajpurohit for valuable discussions, teaching me to create impactful slides, attending my mocks, and encouraging constant improvement.

I humbly would take this opportunity to thank the Director PRL, Dr. Anil Bhardwaj, PRL Dean, Academic Committee Chairman, and Registrar for the support and facilities which I received from the institute during my stay at PRL. I am also indebted to all the faculty and staff members of our division for providing a pleasant research environment throughout all these years. I would also like to thank all my Ph.D. course-work instructors who taught me the basics of Astronomy and Astrophysics, which was necessary before I could begin my research work in a specialized field of Astronomy. I sincerely thank the Academic Committee for rigorously reviewing and giving valuable comments/suggestions during the annual reviews at PRL.

I appreciate the help received from my past and current research group members. I would like to acknowledge Mr. Vishal Shah, Kapil bhaiya, Prasad bhaiya, Rishi bhaiya, Kevi, Dishendra, and Nikitha, who have not only helped *me with observations and other technical aspects at various stages of the project but have also shown concern for my work. I have spent a good time with you guys. I also acknowledge the help from my Junior, colleague, and office mate Sanjay Baliwal with whom I took the observations, discussed scientific and personal problems, and always enjoyed the discussions. I also thank my new junior, Shubhendra, for helping me during synopsis time. Special thanks to my collaborators, Priyanka Chaturvedi, Eike W Guenther, Carina M Persson, Malcolm Fridlund, Artie P Hatzes, Massimiliano Esposito, Sireesha Chamarthi, Steve B Howell, Solène Ulmer-Moll, David R. Ciardi, Andrew W. Boyle, Allyson Bieryla, David W. Latham, Monika Lendl, and Christoph Mordasini, for their valuable contributions.*

A major portion of my thesis has been spent at the observatory, Mount Abu, where the entire staff has been very cooperative. I wish to thank Mr. Rajesh Shah, Mr. G.S. Rajpurohit, Mr. Jinesh Jain, Mr. Mathur, Mr. Nafees, Mr. Patwal, Mr. Narayan Singh, Vivek, Ashirvad, Dinesh, Mitesh, Shankar, Vikram, and Vijendra for their help with the observations. Additionally, my gratitude goes to the entire canteen and house-keeping staff at Mount Abu for keeping the environment pleasant during my stay. I want to thank Rishikesh, Kapil, Nikitha, Partha, and Birendra for proof reading this thesis.

When it comes to thanking my friends, I have a long list. Life in PRL has been so lively with friends during five years of my stay in the hostel. The moments spent at the PRL hostel will always hold a special place in my heart. I want to express my heartfelt gratitude to Shivani Di and Harish bhaiya for consistently being there for me. I truly cherish the opportunity to have met you both. Shivani di, thank you for looking out for me and preventing me from having outside food ;). To Partha, I am thankful for your unwavering support through all the ups and downs. I am deeply thankful to my friends Supriya, Ayushi, and Sandeep for taking care of me and being such great company. I also want to thank my friends, Naval, Anju, Namita, Yash, Silpa, Beenal, Meghna, Vikas, Pranav, Deepak Gaur, Naba, Dayanand, Deepak Rai, Sanjit, Siddharth, Sunil, Yogesh, Anupam, and Arijit. A special mention goes to my best friends, Seema, Pooja, Kanchan, Shivali, and Neeraj, for constantly motivating and inspiring me. I also want to express my gratitude to the Lunch group members, including Deepali di, Shivani di, Shubham, Anil, Birendra, Vineet, Kimi, Neha, Trinesh, Aditya, and Sanjay. Your company during my thesis writing was a great stress *reliever. I want to thank all the seniors & juniors in the Astronomy division, especially Archita, Sandeep, Neeraj, Sushant, Vipin, Biswajit, Abhijit, Abhay, Aravind, Arup, Narendra, Goldy, Arijit, and Ashish.*

Last but not least, I am very grateful to God for granting me this wonderful opportunity and for everything I have achieved.

(Akanksha Khandelwal)

Contents

List of Abbreviations

AIC	Akaike Information Criterion
ARIEL	Atmospheric Remote-sensing Infrared Exoplanet Large-survey
BD	Brown Dwarf
BIC	Bayesian Information Criterion
CCF	Cross-Correlation Function
ExoFOP	Exoplanet Follow-up Observing Program
FAP	False Alarm Probability
FFIs	Full-Frame Images
GLS	Generalized Lomb-Scargle
HET	High Eccentricity Tidal
JWST	James Webb Space Telescope
LC	Light Curve
LLRGB	Low-luminosity Red Giant Branch
MIST	Mesa Isochrones and Stellar Tracks
PARAS	PRL Advanced Radial velocity Abu sky Search
PDCSAP	Pre-Search Data Conditioned Simple Aperture Photometry
PRL	Physical Research Laboratory
PSF	Point Spread Function
QLP	Quick Look Pipeline
RGB	Red Giant Branch
R-M	Rossiter-McLaughlin
RUWE	Renormalised Unit Weight Error
SED	Spectral Energy Distribution
SPOC	Science Processing Operation Center
TCES	Tautenburg Coude Echelle Spectrograph

TEPcat	Transiting Extrasolar Planets catalog
TESS	Transiting Exoplanet Survey Satellite
TFOP	TESS Follow-up Observing Program
TRES	Tillinghast Reflector Echelle Spectrograph
TOI	TESS Object of Interest
TSM	Transmission Spectroscopy Metric
RV	Radial Velocity

Abstract

The thesis primarily focuses on the detection and precise mass measurements of transiting giant planets around evolved stars ($\log g_* \leq 4.1$ cgs, Stassun et al., 2019) using the radial velocity (RV) method. Transiting giant planets are gas giants (with $M_P > 0.25M_J$) that orbit their host stars in a way that enables observers on Earth to witness their transits. The RV data were obtained using the PRL Advanced Radial velocity Abu-sky Search (PARAS) high-resolution spectrograph (Chakraborty et al., 2014), coupled with the 1.2 m telescope at Mt. Abu Observatory, India.

In the past, RV surveys primarily targeted slow-rotating (FGK-type) main-sequence stars, as fast-rotating massive stars posed challenges in planet detection due to the scarcity of suitable spectral lines. However, as these massive stars enter the post-main-sequence phase, their rotation rates slow significantly, rendering planet detection around them comparatively easier. This shift in focus opens new possibilities for RV surveys, unveiling the planetary systems around evolved stars and giving the opportunity to study planet occurrence around massive evolved hosts.

Among the transiting giant planets, the ones that orbit very close to their host stars, typically within 10 days, are known as hot Jupiters. Currently, the count of close-in giant planets or hot Jupiters discovered around evolved stars is limited to ∼90, comprising just ∼2% of the total known exoplanets. These planets exhibit a wide range of diversity in density, and many of these (including main-sequence counterparts) have inflated radii, presenting challenges to existing theoretical models. These systems are rare, and many of the planets around evolved stars are engulfed by their host stars. Moreover, the need to deepen our understanding of planetary systems and their evolution in the later stages of stellar evolution motivates the detection of hot Jupiters orbiting evolved stars.

In light of the limited detections and poor modeling of these close-in giant planets around evolved stars, a total of 7 potential exoplanet candidates were shortlisted for this thesis work from the TESS photometric catalogue. Of the 7 candidates studied, 3 exhibited RV variations, prompting further line bisector

analysis to ascertain the origin of these variations. The results consistently supported the presence of planetary companions orbiting each of these evolved stars. However, one candidate requires additional RV data for conclusive confirmation.

The primary outcome of the thesis is the discovery and characterization of two close-in giant planets, namely TOI-1789 b and TOI-4603 b. TOI-1789 b was found to have a mass of $\sim 0.70 M_J$, an inflated radius of $\sim 1.44 R_J$ (density$\sim$0.28 g cm^{-3}), and orbits an F-type metal-rich slightly evolved star with an orbital period of $\sim$3.20 days. Only eight planetary systems, including the TOI-1789, orbiting stars similar to or more evolved than TOI-1789, are known to be located closer to their host stars ($a \leq 0.05$ AU). The calculated tidal circularization timescale for the orbit of TOI-1789 b is $\sim$0.08 Gyr, shorter than the estimated age ($\sim$2.73 Gyr) of the TOI-1789 planetary system, indicating that the orbit has already circularized. On the other hand, TOI-4603 b stands out as one of the most massive ($\sim 13 M_J$) and densest ($\sim$14.1 g cm^{-3}) transiting giant planets known to date and lies in the overlapping mass range of massive giant planets and low-mass brown dwarfs—a valuable addition to a population of less than five known objects in this category. It orbits a metal-rich F-type sub-giant star in $\sim$7.24 days with an eccentric orbit ($e \sim 0.3$), possibly undergoing high-eccentricity tidal migration. The metal enrichment of the planet (Z_P/Z_{star}) is estimated to be $\sim$4.2 based on interior modeling. The planet's orbit has not yet undergone circularization, further representing its consistency with the star's age.

Despite the similar properties of the host stars, TOI-1789 b and TOI-4603 b showcase remarkable differences in density and mass, highlighting the diversity within planetary systems and emphasizing the need for further exploration to better understand their origin and formation mechanisms. A significant contribution from this work is the addition of two close-in giant planets around evolved stars to the limited number of planets studied in the literature previously for the determination of their masses and radii at similar high accuracies.

Keywords: Transiting Giant Planets, Evolved Stars, High-resolution Spectroscopy, Photometry, Radial Velocity.

List of Publications

1. **Khandelwal A.**, Chaturvedi P., Chakraborty A., Sharma R., Guenther E. W., Persson C. M., Fridlund M., Hatzes A. P., Prasad N. JSSV., Esposito M., Chamarthi S., Nayak A., Dishendra, Howell S. B., *"Discovery of an inflated hot Jupiter around a slightly evolved star TOI-1789"*, MNRAS 509, 3339-3354 (2022). DOI: 10.1093/mnras/stab2970.

2. **Khandelwal A.**, Sharma R., Chakraborty A., Chaturvedi P., Moll S. U., Ciardi D. R., Boyle A. W., Baliwal S., Bieryla A., Latham D.W., Prasad N.J.S.S.V., Nayak A., Lendl M., Mordasini C., *"Discovery of a massive giant planet with extreme density around the sub-giant star TOI-4603"*, A&A Letters, 672, L7 (2023). DOI: 10.1051/0004-6361/202245608.

List of Figures

List of Tables

Chapter 1

Introduction

1.1 Exoplanets: A Historical Perspective

Since ancient times, humans have been fascinated by gazing at the night sky, observing the celestial bodies such as stars, the Sun, the Moon, and the planets, all through the naked eye. These observations served practical purposes such as navigation, timekeeping, and the creation of calendars for agricultural planning. For example, an ancient Indian textbook, the “Surya Sidhanta”, contains verses depicting the positions of many stars in the sky dating back to 7800 BC or even earlier. These texts were updated and revised over time, with the last known revision occurring in 570 AD based on historical evidence (see Narayanan, 2010). These positional updates about stars were necessary because ancient Indian astronomers were aware of the Earth’s precessional motion around its rotational axis. This motion causes the dates of equinoxes and solstices to shift over time, requiring periodic adjustments to the positions of stars in the sky at specific intervals (a shift of 1 arcmin on the projected celestial sphere every about 72 years). Furthermore, we humans have been looking for the answers to various fundamental questions, such as the origin of the Universe, the potential existence of extraterrestrial life, the origins of life on Earth, and more. The question of whether planets similar to Earth exist and whether life exists beyond our own planet is one of the most captivating and profound inquiries in the field of astronomy. Fast forward to 300 BCE, a Greek philosopher named Epicurus, founder of Epicureanism suggested in a 'letter to Herodotus' that "There is an infinite number of worlds, some like this world, others unlike it...". Albertus Magnus a.k.a Saint Albert the Great, in the thirteenth century, also pondered the existence of multiple worlds, stating "Do there exist many worlds, or is there but a single world? This is one of the most noble and exalted questions in the study of Nature." An Italian philosopher Giordano Bruno during the sixteenth century, went further, claiming in his book *'De l'infinito, universo e mondi'* that "There are countless suns and countless Earths all rotating around their suns in exactly the same way as seven planets in our solar system. . . " (Bruno, 1584). In the 17th century, Galileo Galilei constructed an advanced (for the era) astronomical telescope and made significant discoveries by using it, including identifying the four largest moons of Jupiter, observing the phases of Venus, and observationally supporting the heliocentric theory as proposed by Nicolaus Copernicus in the 16th century. Concurrently to these notable findings, Johannes Kepler published laws of planetary motion in his renowned book '*Philosophiæ Naturalis Principia Mathematica*.' These three laws provided an explanation for the elliptical orbits of planets around the Sun. However, observational capacities were restricted during that time, and the detection of planets around other stars (exoplanets, van den Bos, 1943; Gold et al., 1973; Boss et al., 2005a) was entirely speculative.

The first claim of exoplanet detection was published in the mid-nineteenth century when a companion was reported around 70 Ophiuchi (Jacob, 1855; See, 1896). Nevertheless, it was later found to be false (Moulton, 1899; Heintz, 1988). In the 1960s, a Dutch astronomer named Van de Kemp announced the discovery of a planet with a size similar to Jupiter in a 24-year orbital period orbiting Barnard's star (van de Kamp, 1963, 1969). Barnard's star is famous for having high proper motion. The planetary signals were later discarded as instrument systematics (Hershey, 1973). Struve (1952) proposed that Jupiter-like planets could exist in orbits as small as 0.02 astronomical units (AU). He suggested that high-precision radial-velocity measurements and transit photometric observations could be used to detect such planets. For many years, astronomers believed Jupiter-mass planets would be found in Jupiter-like orbits at 5 AU. Campbell & Walker (1979) introduced a significant improvement in radial-velocity observations by using an instrument gas cell as the reference frame. This advancement allowed for a 10-fold increase in precision and initiated a 12-year search for Jupiter-like planets around 21 Sun-like stars. Furthermore, following the years, the first verified discovery of two exoplanets using pulsar timing was proclaimed in 1992 by radio astronomers Aleksander Wolszczan and Dale Frail (Wolszczan & Frail, 1992), who detected planets orbiting a millisecond pulsar PSR 1257+12, located 2300 light years away. These planets were found to have a mass only a few times greater than the Earth. The discovery was surprising as astronomers had expected planets to only orbit main-sequence stars (Lissauer, 1993). Three years later, in 1995, two astronomers, Michel Mayor and Didier Queloz, made a groundbreaking announcement. They discovered a gas giant planet in orbit around the star 51 Pegasi, which is situated at a distance of 50 light years from Earth (Mayor & Queloz, 1995). This host star is classified as a main sequence solar-like star and is gravitationally bound to the planet with a mass of 0.46 times that of Jupiter ($0.46M_J$) in its orbit. This planet completes a full orbit around its host in 4.23 days and is located at a close distance with a separation of 0.05 astronomical units (AU). This distance is about one-eighth of the distance between the Sun and Mercury. This discovery led to the introduction of a new category of exoplanets known as 'hot Jupiters,' which possess masses equivalent to or greater than Jupiter but orbit very closely to their parent stars, typically within 10 days. In recognition of this spectacular discovery, the Nobel Prize in Physics was awarded to Mayor and Queloz in 2019. Following this initial discovery, a significant number of hot Jupiters were subsequently detected (Charbonneau et al., 2000; Rabus et al., 2016; Espinoza et al., 2016; Bento et al., 2018a, and many more). The presence of these hot Jupiters questioned prevailing theories of planet formation and evolution, as it was unexpected for Jupiter-like planets to exist in such close orbits. The concept of planetary migration was thus introduced towards explaining the same (see section 1.4.1). The first multi-planetary system (found three planets) was found in 1999 around the ν Andromedae star (Butler et al., 1999), and the first transiting exoplanet, HD 209458 b, was discovered independently by Charbonneau et al. (2000) and

Henry et al. (2000). The transit method has revolutionized various ground and space-based exoplanet missions, leading to the detection of most of the exoplanets discovered so far, expanding the exoplanet catalog, and enabling follow-up observations. Exoplanet research achieved its next milestone when Charbonneau et al. (2002) analyzed the atmosphere of an exoplanet. The first space mission (CoRoT; Baglin et al., 2006a) dedicated to transiting exoplanets was launched in 2006 and discovered the first rocky exoplanet (Léger et al., 2009). NASA's Kepler, K2, and TESS mission (Borucki et al., 2010; Howell et al., 2014; Ricker et al., 2015) contributed significantly to the discovery of thousands of exoplanets. Exoplanets have been widely observed throughout the Milky Way galaxy, leading to the discovery of more than 5400 exoplanets to date over $\sim$ 4000 planetary systems*.

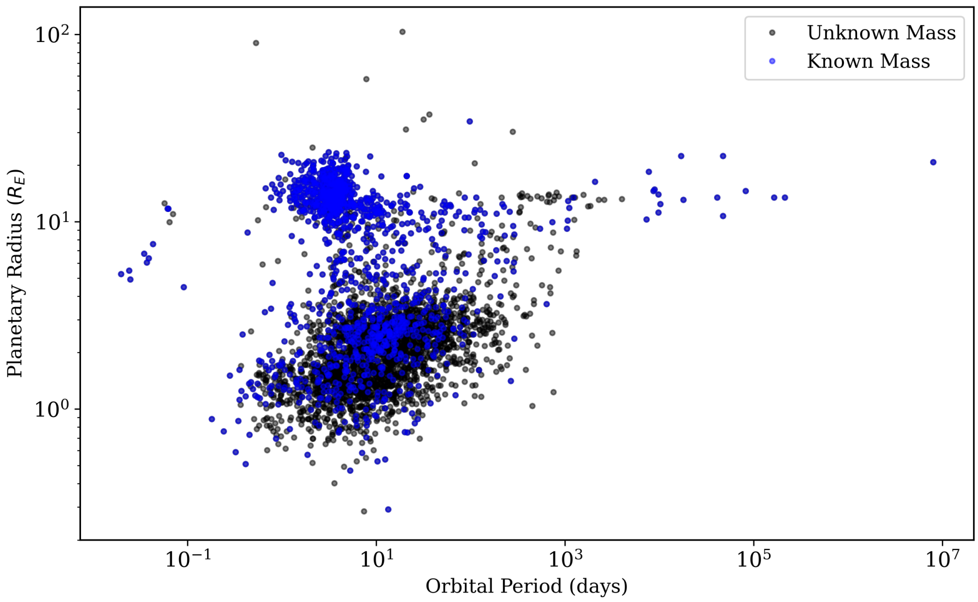

Figure 1.1: The diagram displays known exoplanets as of July 2023 in terms of their radius and orbital period. Only planets with estimates for both of these parameters are included. The color coding in the diagram differentiates between exoplanets with known masses (depicted in blue) and those with unknown masses (depicted in grey). Source: www.exoplanet.eu.

Figure 1.1 presents the statistics of discovered exoplanets as of July 2023, showing their distribution according to radius and orbital period. Only

*www.exoplanet.eu

planets with estimates for both of these parameters are plotted. The plot differentiates between exoplanets with known masses (depicted in blue) and those with unknown masses (depicted in grey). It is noteworthy that ~ 1400 ($\sim 25\%$) out of the 5400 exoplanets have known masses, as evident from the figure. Additionally, the characterization of exoplanets relies on two essential parameters: mass and radius. These parameters are vital for determining the density of a planet, which in turn play a crucial role in understanding the composition, structure, and overall nature of exoplanets. Increasing the number of exoplanets and accurately determining their physical parameters (such as mass, radius, density, etc.) is crucial for understanding the formation and evolution of planetary systems, including our own solar system. This entails both discovering new exoplanets and studying previously known ones. Exoplanets showcase a remarkable range of diversity in their physical and orbital characteristics, serving the idea that the characteristics of our own solar system are merely a singular consequence among a spectrum of potential outcomes. Therefore, a large population of exoplanets is required for comprehensive study.

This thesis focuses on the detection and characterization of the hot Jupiters around evolved stars (Section 1.6). These planets are large gaseous bodies whose formation processes are still not fully understood. In this introductory chapter, the various detection methods that are used in exoplanet discovery and characterization will be discussed. This will be followed by a discussion on giant planets in close-in orbit with an emphasis on their formation, evolution, and physical properties. Furthermore, an overview of exoplanets located around evolved stars will be provided, and finally, the chapter will be concluded by outlining the objectives and structure of the thesis.

1.2 Exoplanet Detection Methods

Astronomers have devised several methods for detecting exoplanets, broadly classified into direct and indirect methods. Direct detection of exoplanets is particularly difficult because the star they orbit is bright enough that it obscures the planet. As a result, scientists have established a number of indirect detection approaches. The two most effective indirect methods for discovering exoplanets are Radial Velocity (RV) and transit photometry. This thesis utilizes both of these methods. The following subsections provide a detailed discussion of the RV and transit photometry method, along with a brief overview of other relevant techniques.

1.2.1 Radial Velocity Method

It is known that if two or more bodies are gravitationally bound, they will orbit around the common center of mass of the system. In a star-planet system, although the star is more massive than the planet, the center of mass does not coincide with the exact center of the star. This results in a smaller reflex orbital motion of the star. The component of the velocity of the star that is along the line of sight to the observer is defined as radial velocity. If the planet's orbital plane is not aligned with the observer's line of sight, the stellar spectral lines will exhibit red shift and blue shift, indicating the position of the star relative to the observer (Figure 1.2). By using the Doppler shift of the emitted light from the star, we can measure its RV.

When a star emits a photon with a wavelength λ_0 in its rest frame, an observer

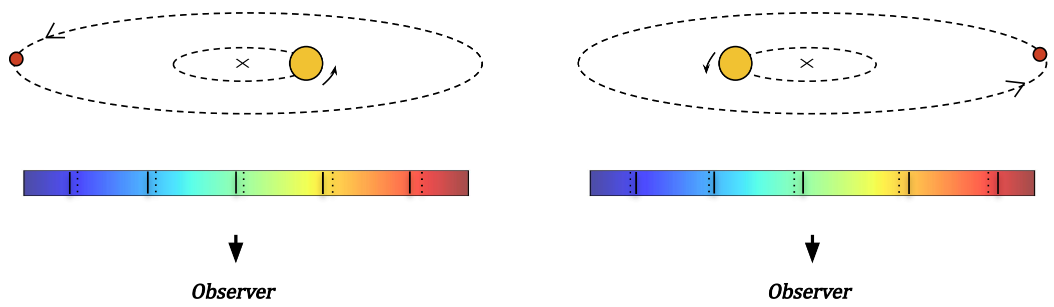

Figure 1.2: The underlying principle of the radial velocity method. The star is represented in yellow, and the planet in brown. In the spectra, the vertical solid lines mark the wavelengths of lines in the rest frame, while the redshift/blueshift is depicted by vertical dotted lines. Left: The star moving away from the observer leads to a redshift observed in the spectra. Right: The star moving towards the observer induces a blueshift in the spectra.

in motion relative to the star perceives the photon at a different wavelength λ. This relationship is described by the equation:

$$\lambda = \lambda_0(1 + z) \tag{1.1}$$

The redshift z is defined as (Wright, 2018, and references therein):

$$z = \frac{1}{\gamma(1 + \frac{V_r}{c})} - 1 \tag{1.2}$$

Here, V_r represents the relative RV between the observatory and the star (i.e., absolute RV), γ is the relativistic factor given by $\gamma = \sqrt{1 - \frac{v^2}{c^2}}$, and v is the scalar relative velocity between the frame of the star and the observatory (not necessarily in the radial direction). The accuracy of these absolute RVs is of order 100 ms^{-1} (Chubak et al., 2012) and is limited by spectrograph wavelength calibration and factors such as internal motions of emitting material and redshifts due to general relativity. Differential RVs, tracking changes in redshift between epochs, offer more precise measurements by minimizing the impact of uncertainties, allowing for over two orders of magnitude improvement in precision compared to absolute redshift accuracy. Moreover, the Earth's rotational and orbital motion induces variations in the measured RV of a stable star over daily and annual cycles. To account for this motion, barycentric correction is applied (see section 2.6.4).

Furthermore, the astrocentric Keplerian orbit of the planet is illustrated in Figure 1.3, and the star's radial velocity ($V_r(t)$), determined by theoretical calculations (Seager, 2010), is given by–

$$V_r(t) = K.[\cos(\theta(t) + \omega) + e\cos\omega] \tag{1.3}$$

$$K = \left(\frac{2\pi G}{P}\right)^{1/3} \frac{M_P \sin i}{M_*^{2/3}} \frac{1}{\sqrt{1 - e^2}} \tag{1.4}$$

In this context, K denotes the semi-amplitude of the RV curve (see Figure 1.3), $\theta(t)$ represents the true anomaly, and ω stands for the argument of periastron. Additionally, P signifies the orbital period, M_P denotes the true mass of the

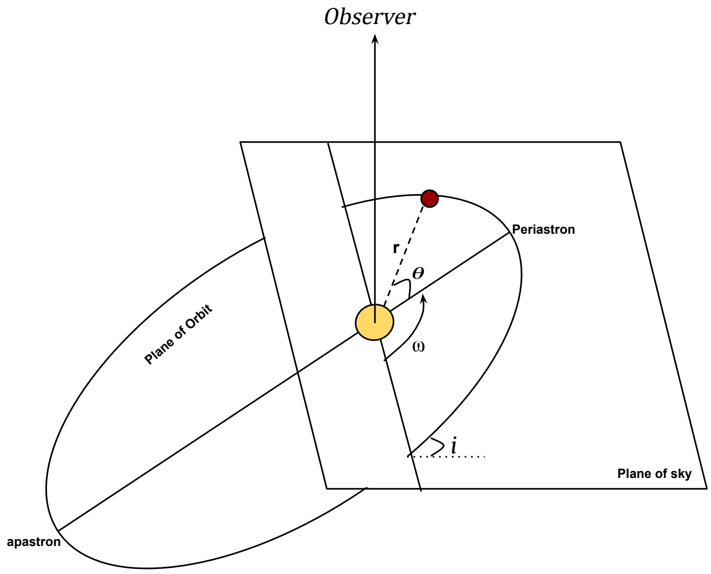

Figure 1.3: A visual representation showcasing the orbital parameters of the star-planet system.

planet, i is the inclination angle, e represents the eccentricity of the orbit, and M_* is the mass of the star. Each RV measurement corresponds to a particular time, and a graph can be generated, indicating the RV of the star as a function of time. Since the star is periodically orbiting around the center of mass, we can observe periodic changes in its RVs, as depicted in Figure 1.4.

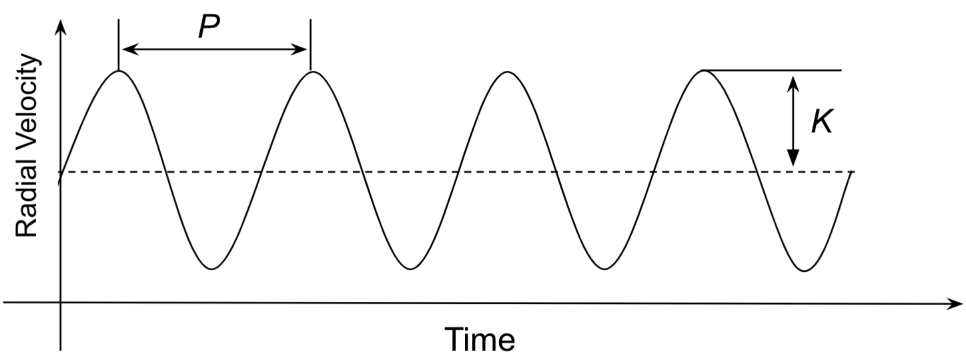

Figure 1.4: RV plotted as a function of time. The orbital period (P) and semi-amplitude (K) of the RV curve are represented.

By examining the RV curve, we can determine the semi-amplitude (K)

of the host star, which is equal to half of the total amplitude of the fitted curve and by rearranging equation 1.4, we can determine the minimum mass of the exoplanet ($M_P \sin i$).

1.2.2 Transit Method

A transit occurs when a planet passes in front of its host star, resulting in a detectable decrease in the star's brightness (Figure 1.5). The transit event begins when the planet's disk first makes contact with the disk of its host star, known as the first contact or t_1. As the planet continues to orbit, it moves in front of the star until the entire planetary disk blocks the stellar disk, which is known as the second contact or t_2. The time period between t_1 and t_2 is called the ingress. Similarly, the egress is the time period between the moment when the planet reaches the opposite edge of the stellar disk, t_3, and the point at which the planet is completely outside the stellar disk, t_4, marking the end of the transit (see Figure 1.5). The duration of the transit is the time period between t_1 and

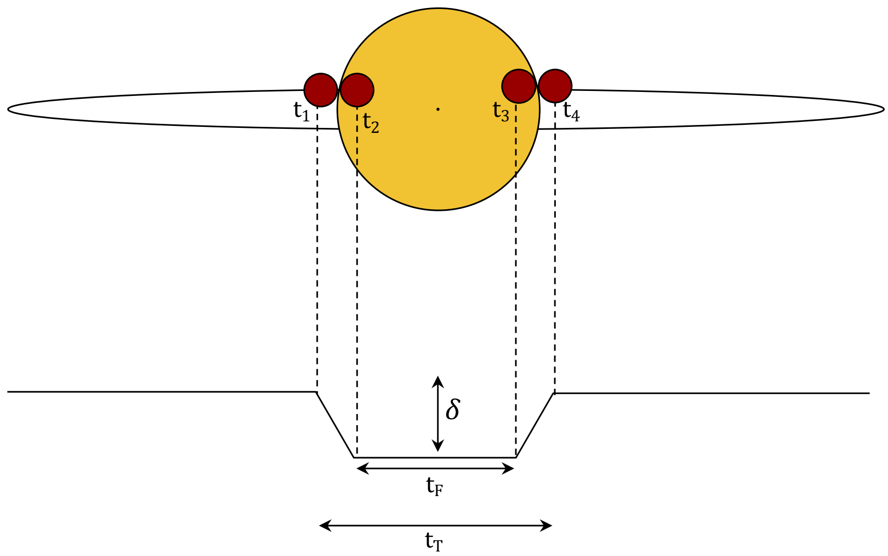

Figure 1.5: A schematic representation of a planet transiting its host star, accompanied by the corresponding variation in brightness during the transit (depicted at the bottom). The transit parameters (δ, t_F, t_T) used in the subsequent equations 1.5 to 1.9 are clearly indicated in the figure.

t_4. By analyzing the depth and duration of the transit, one can infer important characteristics of the exoplanet, such as its size relative to the host star (R_p/R_*), its orbital period (P), the distance (a) between the planet and the star, and the inclination angle (i). In the following subsection, a brief description will be provided on how the parameters of a planet are determined using the transit method (Seager & Mallén-Ornelas, 2003).

1.2.2.1 Planet parameters from transit light curves

If there is no limb darkening in the host star, the planet is completely dark, and there are no contributions from nearby stars, the transit depth (δ) can be expressed as:

$$\delta = \frac{L_* - L_{*,transit}}{L_*} \tag{1.5}$$

Where L_* is the luminosity of a star outside of transit and can be calculated as $4\pi R_*^2 F_*$. The stellar radius and stellar flux per unit surface area are represented as R_* and F_*, respectively. On the other hand, the luminosity of a star during transit is given by $L_{*,transit} = L_* - 4\pi R_P^2 F_*$, where R_P is the planet radius. The transit depth can then be related to the ratio of the planet's radius to the star's radius as follows

$$\delta = \frac{R_P^2}{R_*^2} \tag{1.6}$$

The impact parameter b, which represents the projected distance between the centers of the planet and the star during the transit event, can be derived from the parameters of the light curve according to the following equation (Seager & Mallén-Ornelas, 2003):

$$b = \frac{a}{R_*}\cos i = \sqrt{\frac{(1-\sqrt{\delta})^2 - [\sin^2(t_F\pi/P)/\sin^2(t_T\pi/P)](1+\sqrt{\delta})^2}{1-[\sin^2(t_F\pi/P)/\sin^2(t_T\pi/P)]}} \tag{1.7}$$

Where a/R_* refers to planet orbital distance normalized by the stellar radius, can be expressed as

$$\frac{a}{R_*} = \sqrt{\frac{(1-\sqrt{\delta})^2 - b^2[1-\sin^2(t_T\pi/P)]}{\sin^2(t_T\pi/P)}} \tag{1.8}$$

The definition of b in equation 1.7 allows for the derivation of the planet's orbital inclination projected onto the plane of the sky as-

$$i = \cos^{-1}(\frac{bR_*}{a}) \tag{1.9}$$

Moreover, in this thesis, the transit model developed by Mandel & Agol (2002) is used for transit light curve fitting. It incorporates several parameters, such as the center-to-center distance between the planet and star (d), the radii of the planet and star (R_p and R_*, respectively), the normalized separation of the centers (r/d), and the size ratio (R_p/R_*) [see Figure 1 from Mandel & Agol (2002)]. For a uniform source, Mandel and Agol provided the following expression for the ratio of obscured to unobscured flux:

$$F(p, z) = 1 - \lambda(p, z) \tag{1.10}$$

where,

$$\lambda(p, z) = \begin{cases} 0 & \text{for } 1 + p < z \\ \frac{1}{\pi}[p^2\kappa_0 + \kappa_1 - \sqrt{\frac{4z^2 - (1 + z^2 - p^2)^2}{4}}] & \text{for } |1 - p| < z \leq 1 + p \\ p^2 & \text{for } z \leq 1 - p \\ 1 & \text{for } z \leq p - 1 \end{cases}$$

and $\kappa_0 = \cos^{-1}[(p^2 + z^2 - 1/2pz)]$, $\kappa_1 = \cos^{-1}[(1 - p^2 + z^2/2z)]$. By using the formulation for both in-transit and out-of-transit regimes, the transit data can be modeled. Through the utilization of κ_0, κ_1, and p, the radii and inclination angle of the exoplanet can be determined via photometric techniques as given in the above equations. Moreover, Mandel & Agol (2002) take into account the presence of limb-darkening (quadratic and non-linear laws). The selection of the appropriate function depends on factors such as the relative size (radius) of the planet compared to the star and the planet's position on the stellar disk. For the precise analytical equations, please see Mandel & Agol (2002).

1.2.3 Other Exoplanet Detection Methods

- **Direct imaging**

  Direct imaging is a method for finding exoplanets where telescopes are used to take images of the planet directly. This technique specifically looks for planets at infrared wavelengths. The reason for using this technique in the infrared regime is that planets emit the most heat (thermal emission) in this region. This is advantageous because it significantly enhances the contrast between stars and planets compared to visible wavelengths (about one million versus a billion, respectively), making it possible to detect exoplanets (Close et al., 2012; Macintosh et al., 2015; Curiel et al., 2022; Franson et al., 2023). The direct imaging technique entails using a coronagraph to block out the star's light, allowing the faint light from the planet to be visible.

  This approach is suitable for detecting young planets that are warm and mainly emit in the infrared due to their thermal radiation. It is particularly effective for planets situated far from their host star, large and bright enough to be seen with telescopes, and have a face-on orientation. There are ~ 67 exoplanets have been discovered using this technique (Table 1.1).

- **Astrometry**

  Astrometry is the science of accurately determining the positions of stars. In the context of exoplanet detection, astrometry can reveal the presence of planets by observing small wobbles in the motion of a star. These variations are caused by the gravitational pull exerted by an orbiting planet, as discussed in Section 1.2.1. Through the observation of the star's position over time, astronomers can determine its proper motion, which is the apparent motion of the star across the sky due to its motion through space. They can then look for any deviations from the expected motion that may be caused by the presence of a planet.

  One of the main advantages of the astrometric method is that it can be used to detect planets in wider orbits than other detection methods, such as the radial velocity method or the transit method. However, it is also more challenging because the wobbles in the star's position are much smaller and harder to detect. Current astrometry missions, such as the European Space Agency's Gaia mission (Gaia Collaboration et al., 2022a), are able to detect exoplanets with masses similar to Neptune or Jupiter around nearby stars. But this number is limited to two: DENIS-P J082303.1-491201 b (Sahlmann et al., 2013) and GJ 896 A b (Curiel et al., 2022).

- **Gravitational microlensing**

  Gravitational Microlensing utilizes the concept of gravitational lensing, which was initially proposed in Einstein's general theory of relativity. When a massive object passes in front of a more distant star, its gravity can bend and magnify the light from the star (Ibrahim et al., 2015). If a planet is present around the foreground object, it can create a smaller but detectable additional lensing effect, resulting in a momentary brightening of the star's light curve.

  While microlensing is sensitive to planets in wide orbits and can detect planets down to Earth-like masses, its effectiveness relies on the precise timing and monitoring of a large number of stars to detect the rare microlensing events caused by exoplanets. Several free-floating objects (rouge planets) have been found with this method. Additionally, these events are typically short-lived, usually lasting only a few days, making it challenging to conduct follow-up observations. There are ~ 200 exoplanets that have been discovered with this method (Table 1.1).

- **Pulsar timing**

  Pulsars are a class of celestial objects consisting of highly magnetized rotating neutron stars (Lorimer, 2001) that emit beams of electromagnetic radiation from their magnetic poles. These neutron stars are the incredibly dense remnants of supernova explosions. The radiation emitted by pulsars can only be observed when the beam is directed towards Earth, creating a pulsating appearance with short and regular rotational periods that generate a precise interval between pulses. The timing of the pulses can exhibit slight regular variations that indicate the pulsar's movement back and forth, orbiting the center of mass of a system with one or more planets. Through precise measurements of these variations, astronomers can deduce the orbit and mass of the planets.

This method is extremely sensitive and can detect planets as small as one-tenth the mass of Earth (Sinukoff et al., 2013). However, pulsars are relatively rare celestial objects, and only ∼7 extrasolar planets have been discovered by this method (Bailes et al., 2011; Starovoit & Rodin, 2017; Spiewak et al., 2018) (Table 1.1). Additionally, the intense high-energy radiation emitted by pulsars makes them unsuitable for life to exist on planets orbiting around them.

Discovery Method	**Number of Planets**
Transit	4092
Radial Velocity	1048
Pulsar Timing	7
Astrometry	2
Microlensing	200
Direct Imaging	67
Others	54

Table 1.1: Confirmed exoplanet statistics as of July, 2023 using different detection techniques†.

Table 1.1 presents the statistics for confirmed exoplanets, with the most successful detection method being the transit method, followed by the RV method. This is because both of these methods are sensitive to detecting large and massive planets with short orbital periods, which are easier to detect due to the more frequent and prominent signals they produce. Microlensing, astrometry, and direct imaging are less successful due to technical limitations and the difficulty of detecting smaller planets with longer orbital periods.

1.3 Classification of Exoplanets

Exoplanets can be classified based on observable features such as mass and radius. It provides a more simplified way to distinguish the various populations

†https://exoplanetarchive.ipac.caltech.edu/docs/counts_detail.html

of exoplanets. Borucki et al. (2011) and Fulton et al. (2017) proposed following classifications of exoplanets based on their size–

Planet-regime	**Planet Size** ($R_\oplus$)
Earth-size	$R_P \leq 1.25$
Super-Earth-size	$1.25 < R_P \leq 2.0$
Neptune-size	$2.0 < R_P \leq 6.0$
Jupiter-size	$6.0 < R_P \leq 15.0$
Very large size	$15.0 < R_P \leq 22.4$

Table 1.2: Classification of planets based on planet size.

Stevens & Gaudi (2013) proposed a classification of exoplanets based on their mass, which includes the following categories–

Planet-regime	**Planet Mass range** (M_J)
Earth planets	$10^{-4} < M_P \leq 10^{-3}$
Super-Earths	$10^{-3} < M_P \leq 10^{-2}$
Neptunes	$10^{-2} < M_P \leq 0.31$
Jupiters	$0.31 < M_P \leq 3.14$
Super-Jupiters	$3 < M_P \leq 13$
Brown-Dwarfs	$13 < M_P \leq 75$
Stars	$75 < M_P \leq 1047$

Table 1.3: Classification of planets based on planet mass.

Overall, the classification of exoplanets is an important tool for astronomers to understand the diversity of planets in the universe in addition to their formation and evolution.

The following paragraph highlights some commonly recognized types of exoplanets within the community based on their composition:

Gas-giant planets: These are exoplanets that are primarily composed of hydrogen and helium gas or ices such as water, methane, and ammonia. These planets are often characterized by their large size and thick atmospheres consisting mainly of hydrogen and helium. Examples of gas giant planets include Jupiter and Saturn in our solar system.

Sub-Neptunes or Mini-Neptunes: These exoplanets resemble our solar system's Neptune in size and possess thick atmospheres primarily consisting of hydrogen and helium. They may also have layers of ice, rock, or oceans beneath their atmospheres.

Super-Earths: These planets are primarily composed of rock and are larger than our Earth, yet smaller than Neptune or Uranus.

Terrestrial planets: These exoplanets are composed mainly of silicate rocks and metals and are similar in composition to the terrestrial planets in our solar system.

Goldilocks planets or Habitable Zone planets: These exoplanets are located in the habitable zone of their host star, where conditions may be suitable for liquid water and potential life.

1.4 Giant Planets in Close-in Orbits

Giant planets in close-in orbit are also known as hot Jupiters. These are a type of exoplanet that have masses similar to or greater than Jupiter but orbit very close to their host stars ($M_P > 0.25 M_J$ and $P < 10$ days; Dawson & Johnson, 2018). The detection of exoplanets has been greatly influenced by the RV and transit methods, which have revolutionized the field of exoplanet research (Wright et al., 2012). RV methods have enabled us to determine the masses of exoplanets, and the precision of these mass measurements directly influences our ability to constrain their densities. This, in turn, contributes to the advancement of theoretical models concerning planet formation and evolution. The discovery of hot Jupiters have played a crucial role in driving technical advancements as they were the first kind of exoplanets to be discovered. Over time, the development of spectrographs such as ELODIE (Baranne et al., 1996), CORALIE (Udry et al., 2000), HARPS (Mayor et al., 2003; Cosentino et al., 2012), SOPHIE (Perruchot et al., 2008), TRES (Fűrész, 2008), HPF (Mahadevan et al., 2012), PARAS (Chakraborty et al., 2014), CARMENES (Quirrenbach et al., 2014), EXPRES (Jurgenson et al., 2016), NEID (Allen et al., 2018), ESPRESSO (Pepe et al., 2021), NIRPS (Bouchy et al., 2022), etc., have facilitated remarkable improvements in RV precision to a few tens of cm s^{-1}.

These hot Jupiters are the proving ground for most of the approaches to determine the atmospheric compositions and orbital and dynamical properties of the exoplanetary systems (Sing et al., 2011; Zhou et al., 2014; Louden & Wheatley, 2015). Despite their relatively larger sizes and higher masses, which make them easier to detect, the number of confirmed hot Jupiters is limited to ~ 600[‡]. Over the past decade, RV and transit (mainly Kepler (Borucki et al., 2010) and TESS (Ricker et al., 2015)) surveys have provided the existence of a significant number of low-mass planets in close-in orbits around their host stars. The discovery of these low-mass planets has far surpassed the number of giant planets like Jupiter, which are relatively uncommon around solar-type stars. According to the research conducted by Wittenmyer et al. (2016), only about 6.2% of solar-type stars have giant planets orbiting between 3 and 7 AU. Hot Jupiters are even rarer, occurring at a rate of $\sim 1\%$ around solar-type stars (Marcy et al., 2005; Mayor et al., 2011; Wright et al., 2012; Beleznay & Kunimoto, 2022a). Despite their rarity, they have been the subject of intense study and have provided valuable insights into planetary formation and evolution, as discussed in the next Section 1.4.1.

1.4.1 Formation, Migration, and Tidal Evolution

1. **Formation of close-in giant planets:**

   The solar system has been the primary focus of planetary formation theories, leading to the establishment of two notable models: the core-accretion model (Safronov, 1972; Goldreich & Ward, 1973; Hayashi, 1981; Pollack et al., 1996; D'Angelo et al., 2010) and the disk instability model (Boss, 1997; Durisen et al., 2007).

   (a) The **core accretion model** suggests that the giant planets form by the gradual accumulation of solid materials in a protoplanetary disk. According to this theory, a solid core is initially formed through the accumulation of planetesimals and dust particles. Once the core reaches a certain mass threshold, it begins to accrete gas from the surrounding disk, predominantly composed of hydrogen and helium. This gas accretion process continues until the planet reaches its final

[‡] http://exoplanet.eu/

mass (Haisch et al., 2001; Matsuo et al., 2007). Two crucial conditions that need to be satisfied for successful giant planet formation according to the core-accretion model are as follows (Pollack et al., 1996):

- The timescale required to build up the solid core should be shorter than the lifespan of the gas disk. The gas disks typically exist for a few million years (Fedele et al., 2010; Barenfeld et al., 2016), and during this period, the core must grow sufficiently to initiate the gas accretion phase.
- The region in the protoplanetary disk where the core forms known as the feeding zone, should contain an ample amount of mass to facilitate the growth of a core with a mass around ten times that of Earth ($10M_{\oplus}$; Pollack et al., 1996; Dawson & Johnson, 2018).

(b) The **disk instability model** (Boss, 1997) proposes that the giant planets form through the gravitational fragmentation of the protoplanetary disk. According to this theory, the disk becomes gravitationally unstable under certain conditions, causing it to fragment into clumps. These clumps then collapse under their self-gravity and form giant planets. The disk instability model suggests that giant planets can form relatively quickly within a few thousand years. Gas giants are rapidly created in this process before the gas in the disk becomes depleted (Saumon et al., 1995; Young et al., 2003). The Toomre criterion for disk instability is determined by the speed of sound (c_s), the epicyclic frequency[§] (κ), and the gas surface density (σ_g). Mathematically, it can be expressed as

$$Q = \frac{c_s \kappa}{\pi G \sigma_g} \tag{1.11}$$

If $Q \leq 1$, the disk is considered unstable. Hence, denser disks with higher gas surface densities are more prone to instability according to the Toomre criterion (Toomre, 1964; Safronov, 1960).

[§]represents the frequency of radial oscillations within accretion disk.

Furthermore, there are three primary theories explaining the origins of close-in giant planets: in-situ formation, gas disk migration, and high-eccentricity tidal migration. These theories explore different pathways through which these planets may have formed and are discussed in more detail below.

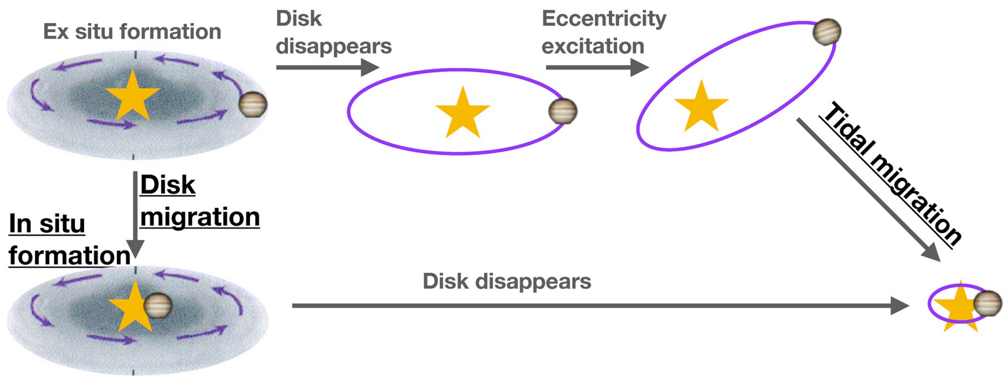

Figure 1.6: The three hypotheses explaining the origins of hot Jupiters: in-situ formation, disk migration, and high eccentricity tidal migration. Credits: Fortney et al. (2021).

2. **In-situ formation**

   One of the most intriguing and open questions in the field of exoplanetary science is whether hot Jupiters can form within the short periods they currently orbit (see Figure 1.6). The possibility of in-situ formation arises if one or both of the proposed mechanisms for giant planet formation can occur in close proximity to the star. If core accretion is the dominant mechanism, it requires a significant accumulation of solid material in the proximity of the star to form a giant planet. However, the high temperatures near the star pose a challenge. According to Rafikov (2005), the increased temperatures near the star can cause the gas to become unbound from the star, making the conditions for gravitational instability in the immediate disk vicinity unlikely. Nevertheless, recent models proposed by Batygin et al. (2016) and Bailey & Batygin (2018) support the plausibility of in-situ formation of close-in giant planets. These models indicate that the mass distribution of short-period giant planets in relation to their orbital periods and their inner boundaries align with the predictions for in-situ formation.

3. **Migration**

   Hot Jupiters may form further out in the protoplanetary disk where the conditions for core accretion and/or gravitational instability are more favorable. It is believed that these close-in giant planets formed beyond the ice line and then migrated inward at their present location (Lin et al., 1996; Rafikov, 2006). The giant planet migrates to a close-in orbit via gas-disk migration and high eccentric tidal migration, as discussed below.

   (a) **Gas-disk migration** refers to the process by which gas giant planets undergo orbital migration within the disk of gas and dust surrounding a young star during the early stages of planetary formation (Goldreich & Tremaine (1980) and see Baruteau et al. (2014) for a comprehensive review). Gas-disk migration can be further classified into two main types: Type I migration and Type II migration.

   - **Type I migration** is driven by torques resulting from Lindblad (Ward, 1997; Armitage, 2020) and co-rotation resonances (Paardekooper & Mellema, 2006; Duffell & Chiang, 2015). Lindblad resonances induce spiral density waves in the gas surrounding the planet's orbit, leading to the planet losing angular momentum and migrating toward the star. The migration rate depends on the planet's mass and the local gas density. Co-rotation torques are also exerted by gas following horseshoe orbits, causing the planet to either gain or reverse its migration direction. The efficiency of Type I migration is influenced by factors such as gas pressure, viscosity, and temperature gradients. This scenario applies to a protoplanet of relatively small mass that remains embedded within the surrounding disk.
   - **Type II migration** occurs when a planet gains a significant mass, typically a few 10th of Jupiter's mass, allowing it to create

a gap in the surrounding disk. Once the gap is formed, the planet then becomes "trapped" within this gap and migrates towards the star, following the disk's viscous evolution and the inward flow of gas accretion. The planet's mass continues to increase due to gas accretion, eventually approaching the mass of the surrounding disk. At this point, the planet's migration slows down and eventually stops. This behavior has been confirmed by Mordasini et al. (2009) and is relevant for understanding the formation and evolution of giant planets in planetary systems.

(b) **High-Eccentricity Tidal (HET) migration** is a proposed mechanism for moving a giant planet from a distant orbit of several AU to a much closer orbit of a few hundredths of an AU. This involves changing the planet's motion in two steps: first, reducing its angular momentum, and secondly, decreasing its total energy. To reduce the angular momentum and orbital energy, several mechanisms have been proposed:

- **Planet-planet scattering**– When two or more giant planets dynamically interact with each other, their orbits can change over time. These interactions cause their orbits to become more elongated (eccentric) and tilted (inclined) as they exchange their angular momentum. Eventually, these changes can bring the planets close to each other, resulting in what we call "close encounters" between the planets. During such encounters, one planet may be perturbed into a high elliptical orbit with a small periastron distance, resulting in intense tidal interactions with its host star (e.g., Rasio & Ford, 1996; Weidenschilling & Marzari, 1996; Ford & Rasio, 2005; Chatterjee et al., 2008). These tidal forces cause the planet to dissipate orbital energy, resulting in heating. As time passes, the planet loses energy, and its orbit's semi-major axis decreases. This process leads to the circularization of the orbit, eventually transforming a cold Jupiter into a hot Jupiter.

- **Secular interactions**– Secular interactions refer to the gradual exchange of angular momentum between distant planets. This process allows a Jupiter-like planet to transfer its angular momentum to other planets or stars within the system over a long period of time, spanning many orbits. Planets can undergo periodic (Petrovich, 2015) or chaotic (Wu & Lithwick, 2011; Hamers et al., 2017) exchanges of angular momentum. Kozai-Lidov cycles (Kozai, 1962; Lidov, 1962; Naoz, 2016) are a specific type of periodic angular momentum exchange, affecting both their mutual inclination and eccentricity, occurs when the outer body in a initially coplanar system follows a highly elliptical orbit (Li et al., 2014). As a result, the inner planet may temporarily assume a highly eccentric orbit with a small periastron distance, leading to intense tidal interactions with the star during periastron passage. The dissipation of tidal forces ultimately circularizes and reduces the planet's orbit, resulting in the formation of a "hot Jupiter" (Wu & Murray, 2003; Fabrycky & Tremaine, 2007).

4. **Tidal evolution**

   Regardless of the specific migration mechanism, once hot Jupiters reach close orbits around their host stars, they undergo significant tidal interactions. These tidal interactions result in several outcomes, as described by Matsumura et al. (2010). Tidal dissipation within the planet leads to a) tidal locking, where the rotation period synchronizes with the orbital period; b) circularization of the planetary orbit, where the eccentricity decreases over time until the orbit becomes nearly circular; c) orbital obliquity damping, where the planet's orbital axis aligns with the stellar spin axis, and d) orbital decay, where the planet's orbital semi-major axis gradually decreases. This decay can continue until the planet reaches its Roche limit, at which point tidal forces would cause it to be tidally disrupted.

   The timescales for the abovementioned processes depend on the efficiency of tidal dissipation in both the planet and the star. However, the specific values of these dissipation efficiencies are not well-constrained. Tidal locking is expected to occur relatively quickly, within about 1 million years (Rasio & Ford, 1996). The circularization of the orbit is expected to happen before orbital realignment, with realignment occurring on a similar or shorter timescale than orbital decay (Lai, 2012).

1.4.2 Mass-Radius (M-R) Relationship

One notable characteristic observed in many hot Jupiters is their larger radii when compared to theoretical models of pure H/He objects based on structural evolution (lowest density models). This phenomenon is known as radius inflation and has been extensively studied in the past years (see Fortney & Nettelmann, 2010; Baraffe et al., 2014, for a detailed review). Several factors contribute to variations in their radii and distinctive mass-radius relationships (Laughlin et al., 2011a; Thorngren & Fortney, 2018). The radius inflation is attributed to mechanisms such as atmospheric circulation (Showman & Guillot, 2002), Ohmic dissipation (Batygin & Stevenson, 2010), Tidal dissipation (Bodenheimer et al., 2001; Arras & Socrates, 2010), Layered convection (Chabrier & Baraffe, 2007), and Enhanced atmospheric opacities (Burrows et al., 2007). However, none of these mechanisms fully explain the observed variations in radius (Baraffe et al., 2014). It is possible that some important aspects of the evolution models for irradiated gas giants are missing. The observed inflation in radius could also be the result of a combination of multiple processes. The extent of radius inflation in hot Jupiters may depend on the level of stellar irradiation they receive (Demory & Seager, 2011a; Enoch et al., 2012; Weiss et al., 2013). Observational studies have demonstrated a positive correlation between the equilibrium temperature of a hot Jupiter and its radius (Burrows et al., 2007; Fortney et al., 2021). However, there is a possibility that mechanisms, such as layered convection, which are not anticipated to rely directly on the radiation from the host star, could still contribute to shaping the internal structures of the planet.

Additionally, when comparing the mass and radius of transiting hot Jupiters with irradiated giant planets models, it has been discovered that some hot Jupiters must contain a significant enrichment of heavy elements (Fortney et al., 2007). This indicates that not all heavy elements are confined solely to the planetary cores; instead, substantial amounts of heavy elements are present within the H/He envelopes (Charbonneau et al., 2002; Thorngren et al., 2016). The presence of heavy elements, such as metals, rocks, and water, in the planet's core and envelope can increase its overall density and result in a heavier mass planet for a given radius (Burrows et al., 2007). Thorngren et al. (2016) studied the correlations between the heavy element mass (M_z) with the metallicity of the host star ([Fe/H]) and the total mass of the planet (M_P). They found a clear correlation between M_z and M_P, while a weaker correlation with [Fe/H] as compared to Miller & Fortney (2011). Their results suggest that planets with a higher abundance of heavy elements are more commonly found around stars with higher metallicities, although planets with lower heavy-element content do not exhibit a distinct pattern. Determining the exact composition and structure of hot Jupiter is an ongoing area of research, typically inferred through spectroscopic observations.

Overall, the mass-radius relationship of hot Jupiters contributes to our broader understanding of exoplanetary systems, including their formation, evolution, and atmospheric properties. It serves as a foundation for characterizing more number of hot Jupiters and refining theoretical models, ultimately advancing our knowledge of planetary science beyond our solar system.

1.5 Giant Planets around Evolved Stars

RV surveys have mainly targeted slow-rotating FGK-type stars. This selection was made because more massive main-sequence stars possess fewer suitable spectral lines for Doppler measurements, as their rapid rotation causes line broadening. However, when these rapidly rotating stars transition from the main sequence to a later evolutionary stage, they become cooler and gradually reduce their rotation, making detecting planets around them relatively easier. This opens up new possibilities for RV surveys to include these evolved stars ($\log_* \leq 4.1$, Stassun et al., 2019) and discover more planetary systems.

By studying the evolved stars, we can gain insights into the planet occurrence rate around massive stars as well as the effects of stellar evolution on planetary systems and further our understanding of planet formation and evolution in different stellar environments. The following section discusses the latest research in the field, which serves as the basis for the motivation behind this thesis. By focusing on TESS's population of evolved planet hosts, we have an exceptional opportunity to advance our understanding even further. This thesis aims to contribute to the existing knowledge by discovering and studying more of these systems.

1.5.1 Metallicity Correlation

The correlation between the metallicity of main-sequence stars and the occurrence rate of giant planets is well established (Gonzalez, 1997a; Santos et al., 2001, 2004a; Fischer & Valenti, 2005a; Udry, 2010; Sousa et al., 2011), suggesting that they most likely form through core accretion (Boss et al., 2003; Mordasini et al., 2012). The same correlation appears to be found for subgiant stars as well (Jofré et al., 2015; Johnson et al., 2010a; Ghezzi et al., 2018), while there is no clear consensus for red giant (RGB) stars. About 90 close-in giant planets have been detected around evolved stars, with 62 orbiting metal-rich stars, 19 around metal-poor stars, and the rest around solar metallic hosts[††]. Some studies support the correlation (Hekker & Meléndez, 2007; Reffert et al., 2015a; Johnson et al., 2010a; Jones et al., 2016), while others do not (Takeda et al., 2008; Maldonado et al., 2013; Mortier et al., 2013). In an attempt to explain the lack of correlation in RGB stars, Pasquini et al. (2007) propose that the formation of giant planets around intermediate-mass stars might be primarily driven by disk instability rather than core accretion. This mechanism could remove the dependence on the metallicity of host stars. On the contrary, Mordasini et al. (2012) conducted simulations based on the core accretion model and found that the star's mass can also impact the formation of giant planets. It could compensate for the lower metallicity observed in evolved systems hosting planets compared to main-sequence systems. Despite ongoing research, a definitive consensus has not been reached. However, the TESS population might offer some additional help.

1.5.2 Occurrence Rate

Studies using Doppler planet surveys have found that hot Jupiters occur around main-sequence stars at a rate of approximately 1.0%. However, the exact numbers may vary slightly across different surveys. For instance, Wright et al., 2012 utilized data from the Keck and Lick Observatories and estimated the occurrence rate of hot Jupiters to be approximately 1.2% ± 0.38%. Previously, other studies using similar data found the occurrence rates of hot Jupiters to be 1.2% ± 0.1% (Marcy et al., 2005) and 1.5% ± 0.6% (Cumming et al., 2008). In a separate analysis, Mayor et al. (2011) used RV data from the HARPS and ELODIE instruments and determined the occurrence rate of hot Jupiters to be approximately 0.89% ± 0.36%. In summary, RV surveys have determined that the occurrence rate of hot Jupiters around main sequence stars falls within the range of ∼ 0.8 –1.5% (Marcy et al., 2005; Cumming et al., 2008; Mayor et al., 2011). This contrasts with the occurrence rate observed for Kepler transiting planets, which is estimated to be ∼ 0.4–0.5% (Fressin et al., 2013; Howard et al., 2012; Petigura et al., 2018; Kunimoto & Matthews, 2020). This lower occurrence rate has also been observed for TESS (Zhou et al., 2019b; Beleznay & Kunimoto, 2022b). These discrepancies in occurrence rates have been hypothesized to be due to differences in metallicities among the samples (Wright et al., 2012, Howard et al., 2012), and stellar multiplicity rate (Wang et al., 2015; Moe & Kratter, 2021).

Going beyond the main sequence hosts, there is a dearth of hot Jupiters around these stars, as observed in RV surveys. This indicates disparities in the populations of hot Jupiters between main-sequence and evolved stars (Johnson et al., 2010a; Jones et al., 2016). Meanwhile, transit surveys have found a few systems around evolved stars (Lillo-Box et al., 2016; Rabus et al., 2016; Zhou et al., 2019a; Yee et al., 2023). Occurrence rate studies by Grunblatt et al. (2019) and Temmink & Snellen (2023) for close-in giant planets orbiting *K2* LLRGB and RGB Stars revealed a rate of ∼ 0.5%, similar to that of main-sequence stars.

However, it's important to note that these studies had a limited sample size, with only 3 and 5 confirmed planets, respectively, emphasizing the need to increase the sample of hot Jupiters around evolved stars.

At the time of writing the thesis[¶], a total of 363[‖] exoplanets have been detected by TESS, with 77[‖] of them being classified as hot Jupiters, making up $\sim$ 21% of the total exoplanets from TESS. Among these hot Jupiters, only 17[‖] are orbiting evolved stars, representing $\sim$ 22% of the hot Jupiter population detected by TESS. When comparing this with the overall statistics of hot Jupiters, those found around evolved stars account for only 16%. Moreover, only 10% of the total population of the exoplanets are hot Jupiters. This may be because TESS is more sensitive to detecting larger planets, likely owing to its detectors being less sensitive than those used in the Kepler mission. The lower sensitivity of TESS detectors, in contrast to Kepler, results in a preference for observing brighter stars. This enables meter-class telescopes like the 1.2 m telescope at Mt. Abu, PRL, to be competitive in measuring planet mass. Moreover, TESS is an ongoing survey; the numbers may be expected to increase over time.

1.5.3 Correlation between Host Mass and Giant Planet Occurrence

In order to see the correlation between the host star's mass and the occurrence of giant planets, Johnson et al. (2010a) studied samples ranging from low mass M-dwarfs ($0.2 M_\odot$) to intermediate-mass sub-giants (masses of up to $1.9 M_\odot$). The authors found a trend between the occurrence rate of giant planets and the stellar mass. However, disagreement in determining evolved star mass and selection biases in the stellar sample made this study questionable (Lloyd, 2011, 2013; Schlaufman & Winn, 2013). Recent research has improved mass estimation by utilizing asteroseismology to assess stellar masses. Later on, the samples of Johnson et al. (2010a) were extended up to $5 M_\odot$ by Reffert et al. (2015a), and they found that as the stellar mass in the range from 1.0 to $1.9 M_\odot$ increases, the giant-planet occurrence rate increases, and rapidly drops beyond $2.5 M_\odot$ stellar

[¶]July, 2023

[‖]https://exoplanetarchive.ipac.caltech.edu/

mass. Even after this, other studies, particularly based on the stellar mass determination, have also shown comparable results (Jones et al., 2016; Ghezzi et al., 2018). The discovery of the 17[‖] hot Jupiters orbiting evolved stars by TESS, all within the mass range of 1.0 to 1.9 $M_\odot$, provides additional evidence supporting this correlation.

1.5.4 Eccentricities of Close-in Giant Planets around Evolved Stars

Close-in giant planets orbiting evolved stars are often observed to have more eccentric orbits than those around main-sequence stars. Grunblatt et al. (2018) suggests that this could be indicative of a transient phase where these planets experience faster shrinkage than circularization due to tidal forces from their evolved host stars. Consequently, evolved stars give rise to a distinctive population of close-in planets that are transient and have somewhat elliptical orbits. In contrast, such a population is not commonly found around main sequence stars (Villaver & Livio, 2009; Villaver et al., 2014). A study by Veras (2016) has proposed that the planets around evolved hosts are expected to exhibit notable differences compared to main-sequence stars, primarily due to the dynamic interactions influenced by stellar evolution.

1.5.5 Radius Inflation

More adequate methods to constrain the radius inflation mechanism(s) have been devised recently. By statistically analyzing the radii of hot Jupiters and using models of their internal structure, Thorngren & Fortney (2018) found the key factor for explaining radius inflation is how much incident flux is converted into internal heating. They discovered that the best explanation occurs when the planets receive an intermediate amount of heat, with a temperature $\sim 1{,}600K$. As the host star transitions to the subgiant and giant branch phase, the level of stellar irradiation experienced by hot Jupiters undergoes a substantial increase (as the size and luminosity increase as compared to main sequence stars; Hartman et al., 2016). These findings provide additional evidence supporting radius inflation is related to the incoming stellar incident flux on the planet. Notably, there is a threshold of incident flux, $\sim 2\text{x}10^8\ erg/s/cm^2$ ($\sim 1000K$ in equilibrium temperature), below which it is highly unlikely to discover inflated hot Jupiters (Demory & Seager, 2011a). Lopez & Fortney (2016) demonstrated that warm Jupiters "re-inflate" when their host stars evolve off the main sequence, resulting in equilibrium temperatures exceeding 1,000 K (Grunblatt et al., 2018, 2019). Further studies of re-inflation into both the main sequence and post-main sequence will contribute to better constraining the mechanism(s) responsible for the radius anomaly observed in hot Jupiters.

1.6 Motivation and Objectives of Thesis

Despite decades of research, the fundamental questions surrounding the formation and evolution of close-in giant planets or hot Jupiters remain unanswered. Exploring hot Jupiters orbiting evolved stars is motivated by the need to deepen our understanding of planetary systems and their evolution in the later stages of stellar evolution. These hot Jupiters orbiting evolved stars present unique scientific opportunities to enhance our understanding of the aforementioned aspects (see Section 1.5), which includes the study of close-in giant planet occurrence rate around evolved stars and its correlation with the stellar mass and metallicity as well as the study of radius inflation, and eccentricity distribution of hot Jupiters. At the beginning of this research[†], only 67[‖] hot Jupiters were discovered around evolved stars, which are depicted in Figure 1.7. Consequently, a large number of exoplanets in this category are required. TESS survey, which is currently operational, may contribute to detecting more of these systems. Only two such systems were detected (with TESS) at that time.

The primary objectives of the thesis are as follows:

- Detect and characterize the close-in giant planets around evolved stars using precise RV measurements. This is achieved through the utilization of the PRL Advanced Radial velocity Abu sky Search (PARAS) spectrograph. The candidates for RV follow-up observations were selected from TESS photometric survey. The RV and transit observations allow for pre-

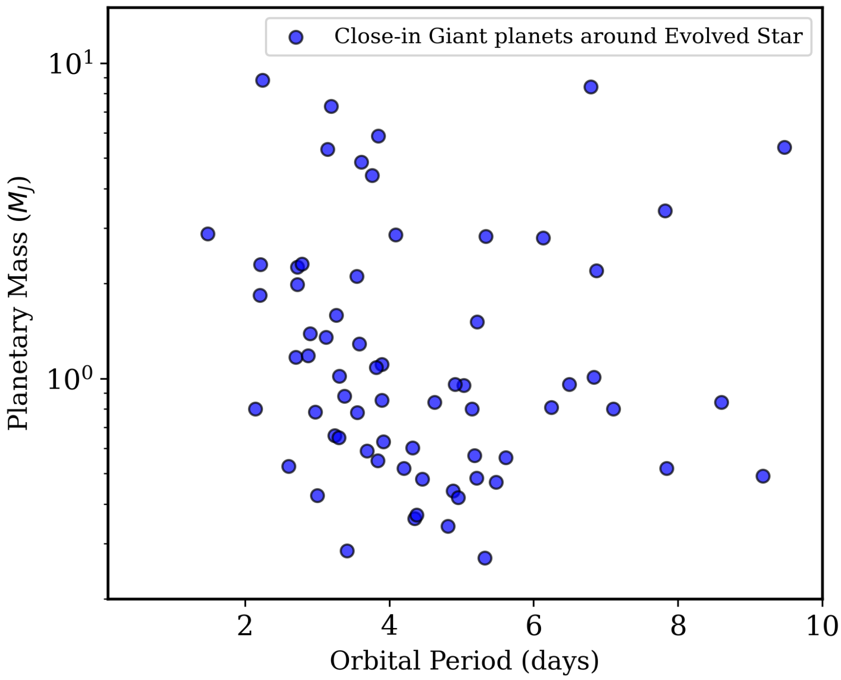

Figure 1.7: The plot represents all the known close-in giant planets around evolved stars at the time of candidate selection for the thesis work†, showcasing their planetary mass and orbital period. Source: NASA Exoplanet Archive‖.

cise measurements of the physical parameters of exoplanets. These parameters include their masses, sizes, distances from their host stars, and orbital parameters. The thesis work involves conducting high-resolution spectroscopy observations, reducing the echelle spectra, and analyzing the extracted spectra in order to obtain RV measurements.

- Determine the planet's parameters such as orbital period (P), the planet's radius relative to the host star's radius (R_p/R_*), and orbital inclination (i) utilize the transit photometry of the star. This thesis entails accessing relevant archival data from the TESS database and performing photometric measurements using ground-based telescopes whenever required.

- Determine the mass and radius of the host star precisely using the high-resolution spectra obtained through PARAS. As planetary mass and radius obtained from RV and transit observations, respectively, rely on the mass and radius of the host star (see section 1.2.1). Therefore, it is essential to measure the spectroscopic parameters of the host star precisely. This will enable better constraints on the mass and radius of the primary star. An accurate determination of the stellar parameters of the primary host star will lead to a precise characterization of the planet.

1.7 Overview of the Thesis Chapters

This section aims to provide a brief overview of the structure and content of the thesis.

Chapter 2 provides a detailed description of the PARAS instrument, including its specifications, the observation process used at the observatory, and the data reduction and analysis procedure. Subsequently, a brief summary of the TESS photometric survey is provided. The candidate selection criteria for follow-up observations using PARAS are also discussed.

Chapter 3 starts by introducing stellar activity and its impact on planet detection. The importance of line bisectors in studying the asymmetry of spectral lines to gain insights into physical processes is highlighted. This has been achieved by developing a Python script based on existing literature for bisector analysis and utilizing it on our selected candidates. The methodology and results obtained are discussed.

Chapter 4 presents the discovery and characterization of TOI-1789b, a hot Jupiter-type exoplanet that transits a slightly evolved star. This chapter encompasses discussions on RV and photometry observations, along with their analysis and resulting findings.

Chapter 5 details the discovery and characterization of a massive giant planet orbiting the sub-giant F-type star TOI-4603. Similar to the previous chapter, observations, data analysis techniques, and results obtained for this system are covered as a part of this Chapter.

Chapter 6 covers a summary of this thesis and explores the scope of future work.

Chapter 2

Instrument Description, Observations, and Data Analysis

The primary aim of the thesis is to detect and characterize the close-in giant planets (with $P \leq 10$ days) around evolved stars using precise RV measurements. Chapter 1 highlights several unanswered questions related to these planets. This includes whether they form at their current location or migrate inward, how their atmosphere and internal structure are affected by their extreme surroundings, how the planetary systems evolve with stellar evolution, and what causes the inflated radii observed in many hot Jupiters. To gain a better understanding of these scientific problems, it is crucial to study a larger number of giant planets. These planets are primarily identified as potential exoplanet candidates in several transit surveys like Kepler (Borucki et al., 2010), K2 (Howell et al., 2014), and TESS (Ricker et al., 2015). However, without information on the masses of these planetary candidates, it is not feasible to determine their true nature and characteristics. The RV method has proven to be the most effective approach in determining the mass of an exoplanet (Chapter 1). For this thesis work, we primarily use the pre-existing PARAS spectrograph for RV follow-up observations (or mass measurements) of shortlisted potential giant planet candidates from the TESS photometric survey.

The current chapter provides an overview of the PARAS spectrograph, including its optical layout, instrumental stability, and achievable RV precision.

The TESS photometric survey and the candidate selection criteria for PARAS observations are also discussed. The chapter further discusses the PARAS observational procedures and the data reduction and analysis pipeline. Finally, a brief discussion on the 0.43m telescope is also given.

2.1 Specifications of PARAS Spectrograph

PARAS is a high-resolution (R∼67000) fiber-fed echelle spectrograph indigenously developed at the Physical Research Laboratory (PRL), India (Chakraborty et al., 2014) and attached to the 1.2 m telescope at the PRL Mt. Abu Observatory, located in the Aravalli range in Rajasthan, India (latitude: $24^o39'17.34''$ N, longitude: $72^o46'45.18''$ E, and altitude 1680 m). The instrument is capable of obtaining high-resolution spectra and measuring the RVs of stars with high precision ($\sim$ 1–3 m s^{-1} for brighter stars, Fischer et al., 2016). It has been used to detect exoplanets, Brown Dwarfs (BDs), and very low mass stars (VLMS), as well as to study various physical properties of the F, G, and K-type stars (Chaturvedi et al., 2016, 2018; Chakraborty et al., 2018a; Šubjak et al., 2020).

The light from the telescope is collected using the Cassegrain unit, and it is fed to the spectrograph through the fibers (see Figure 2.4). The Cassegrain unit comprises of calibration unit (Tungston and Uranium-Argon Hollow-Cathode Lamp (UAr HCL)) and the fiber input optics. The main spectrograph consists of the optical elements is located in a separate room within a vacuum chamber. Following are the technical details of the PARAS spectrograph (also see Table 2.1):

- **Optical layout:** The optical layout of the PARAS spectrograph (Figure 2.1) consists of several key components, such as a fiber optic input system, a collimator, an echelle grating, a folding mirror, a cross-disperser, and a CCD detector. The optical design of the spectrograph uses the white-pupil configuration, which reduces the scattering of the light from the UAr HCL and thus enables high RV precision (Chakraborty et al., 2014). It uses an R4 echelle grating as a primary diffraction element and a prism as cross-disperser to separate the orders. This echelle grating has a physical size of 220 × 420 mm with a groove frequency and blaze angle of 31.6 lines/mm and 75^o, respectively, and operated close to the Littrow condition. However, the pupil diameter is only 100 mm, falling on the centeral region on echelle. The apex angle of the prism is 65.6^o, which provides the inter-order separations of 74 to 23 pixels across the 380 to 950 nm wavelength range. The spectra are taken with a deep-depleted and back-thinned 4096 × 4096 pixels CCD (pixel size of 15 μm). To maintain optimal performance, the CCD is cooled using a helium-closed cooling system, achieving a working temperature of -115 ^{o}C. Although the spectrograph is designed to capture the 380 to 950 nm wavelength range in a single exposure, however, for simultaneous wavelength reference mode for precise RV measurements, it is optimized to operate within the wavelength range of 380 to 690 nm. The spectrograph exhibits an approximate efficiency of 30% from the slit position to the detector.

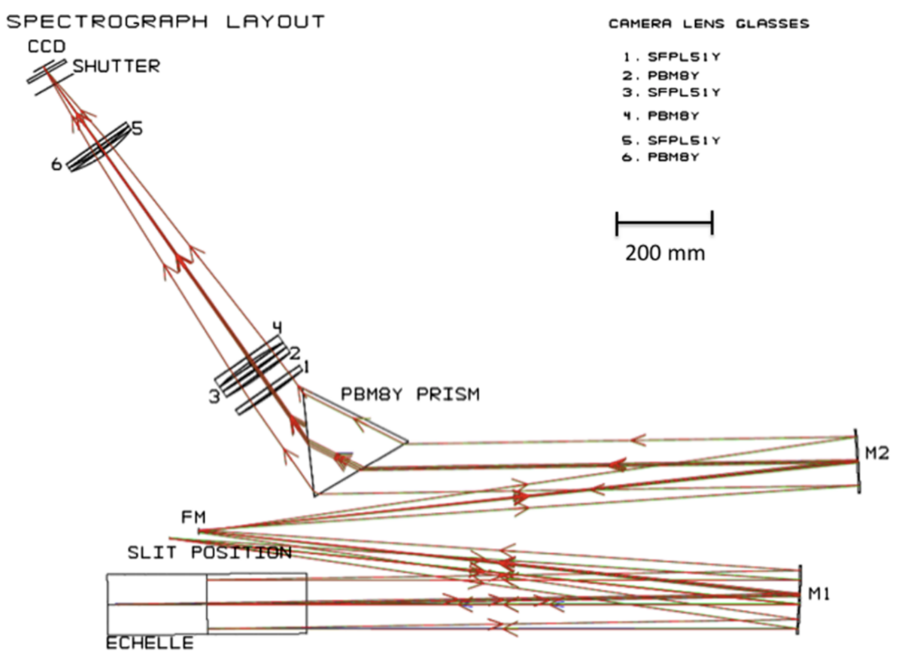

Figure 2.1: The figure illustrates the optical layout of the PARAS spectrograph, showcasing its key components, including collimating mirrors, echelle grating, cross disperser prism, and camera optics (Credits: Chakraborty et al., 2014).

- **Pressure and Temperature Controlled Environments:** The spectrograph optics needs to be placed in a highly-stabilized temperature and pressure environment to minimize the instrumental drifts. To ensure this the spectrograph optics is kept in a vacuum chamber, which in turn is kept in thermally insulated concentric cuboidal chambers. The temperature of the spectrograph is maintained at 24.05° C with a precision of 0.007° C rms, and the pressure is controlled between 0.05 to 0.15 mbar. The spectrograph is also placed on an isolated pier, which prevents vibrations from any other external source.

- **Fiber-feeding at telescope and spectrograph interface:**
The spectrograph uses two fibers, one is science or star fiber and the other one is calibration fiber. Each fiber is a combination of octagonal and circular fibers of 1.5 m and 20 m length, respectively, with a core diameter of 50 μm. From the telescope side, light enters into the octagonal fiber and exits at the spectrograph end from the circular fiber. The use of diverse core shapes of fiber in PARAS exhibits excellent scrambling performance, without using a scrambler. At the telescope interface, a focal reducer converts the f/13 beam that is coming from the telescope to an f/4.5 beam, where the star fiber tip (50 μm size) is inserted, giving the fiber a view of $1.9''$ on the sky. The point spread function (PSF) spot size is $\sim$ 40 μm in rms diameter at the focal plane, giving $1.8''$ on the sky. Hence, the star's light overfills the fiber. In good seeing conditions (seeing $\leq 1.6''$), star FWHM is observed around $1.8''$, resulting in light loss but mitigating PSF variation issues. At the spectrograph interface, the fiber tips are projected onto a virtual slit position with the help of an f/13 achromatic doublet. This configuration provides a resolution that is determined by the projected fiber image at the slit position and enables the precision of $\sim$ 1 m s^{-1}. The center-to-center separation between the two fiber cores is 180 μm, resulting in a separation of 17 pixels on the CCD detector.

Chakraborty et al. (2014) reported that the overall efficiency of the spectrograph, inclusive of the optical fibers, spectrograph losses, and telescope, is $\sim$ 7%. More detailed information regarding mirror reflectivity, individual optical components, and their transmission losses for lenses can be found in Chakraborty et al. (2008); Chakraborty et al. (2010, 2014).

Sr. No.	Parameter	Description
1	Resolution (R)	67000
2	Slit Size	50 µm fiber; there is no physical slit at the slit position.
3	Passband	380–950 nm
4	Pupil Diameter	100 mm, $f/13$ for the off-axis Parabolas.
5	Echelle Grating	Physical size = 220 × 420 mm, Groove frequency = 31.6 lines/mm, Blaze angle = 75°.
6	Prism	Apex angle = 65°.
7	Camera Lens System	$f/5$, Focal Length ∼528.5 mm at 6330Å.
8	CCD Detector	E2V, 4096×4096, 15-micron square pixel.
9	Fiber Optics	Multi-mode, core 50 microns.
10	Pressure and Temperature Controlled Environment	Temperature: 24.05°C with a precision of 0.007°C rms, Pressure is controlled between 0.05 to 0.15 mbar.

Table 2.1: Basic Parameters of PARAS Spectrograph (Chakraborty et al., 2010, 2014).

2.2 RV Precision with PARAS

The actual factor that limits the RV precision is the slope of the spectral lines. Based on this fact, Hatzes & Cochran (1992) derived an equation for RV precision in terms of spectral resolution (R), signal-to-noise ratio (S/N) and wavelength coverage (B in Å) as follows:

$$\sigma_{RV} \sim 1.45 \times 10^9 (S/N)^{-1} R^{-1} B^{-1/2} \ m \ s^{-1} \tag{2.1}$$

Later, a more robust way of deriving the RV precision is given by Bouchy et al. (2001) taking the spectral type (number of lines) & the line broadening also into the account and defining the quality factor Q, representing the spectrum's quality and spectral line richness:

$$Q = \frac{\sqrt{\sum W(i)}}{\sqrt{\sum A_0(i)}} \tag{2.2}$$

where $A_0(i)$ represents the intensity of a zero-velocity spectrum at the ith pixel, and $W(i)$ is the optimum weight assigned to the individual pixel. This weight is inversely proportional to the square of the individual velocity dispersion. The dependance of the RV precision (δV_{rms}) on Q is given by:

$$\delta V_{rms} = \frac{c}{Q\sqrt{N_e^-}} \tag{2.3}$$

where c is the speed of light and, N_e^- are the number of photo-electrons over the whole wavelength range.

The expected RV precision for PARAS spectrograph estimated using these two approaches is listed in Table 2.2. PARAS have already shown a RV

Visual Magnitude Range (mag)	PARAS RV Precision (m s^{-1})
< 6.5	$1 - 2$
$7 - 8$	$3 - 7$
$8 - 9$	$7 - 10$
$9 - 10$	$12 - 15$
$10 - 11$	$15 - 35$

Table 2.2: RV precision with PARAS (for 1800 s exposure) based on magnitudes. Credits: Priyanka Chaturvedi Thesis.

precision of 1-2 m s^{-1} on bright RV standard stars like Sigma Draconis and HD 9407 (see Chakraborty et al. (2014)). Apart from that, a RV standard star named HD 55575 (Bouchy et al., 2013) has also been observed with PARAS for ∼400 days and it yielded a RV scatter of 3.5 m s^{-1}, which comes down to 3.1 m s^{-1} on nightly binning (Figure 2.2). This star has also been observed with SOPHIE+ and produced a similar RV scatter of 3.1 m s^{-1} (Bouchy et al., 2013). This RV precision is well-enough to detect the Neptunian class of planets around Sun-like stars, like K2-236b (Chakraborty et al., 2018a)). For this thesis, we have targeted the close-in giant planets which produce RV variations of few tens of m s^{-1} to a few hundreds of m s^{-1}. Thus, the limiting magnitude (in V-band) for the spectrograph is around 10, with which these planets can be characterized with a high level of confidence ($>$ 3-σ). This has been considered while selecting the potential exoplanetary candidates for this thesis.

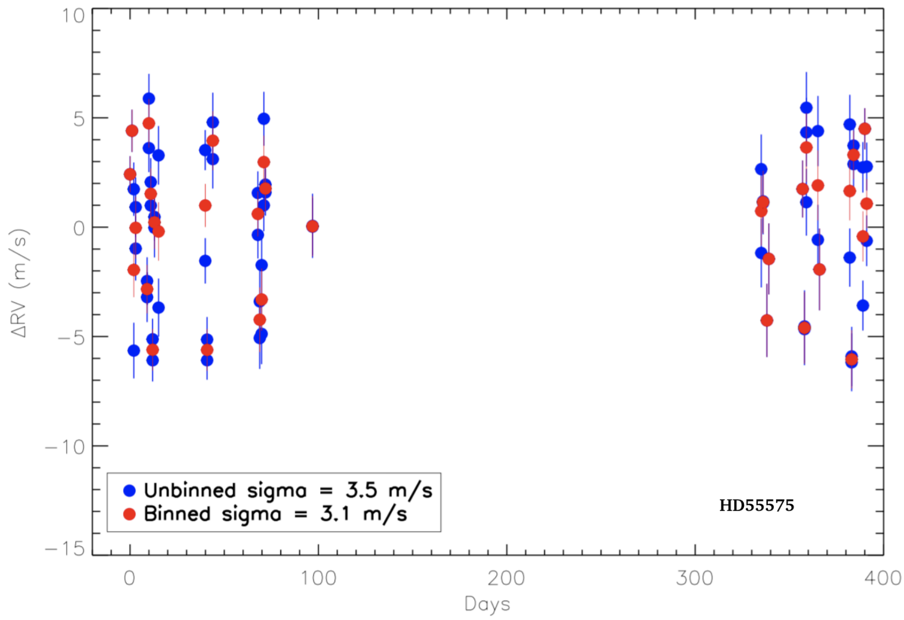

Figure 2.2: HD 55575 (V magnitude: 5.5 and Spectral type: F9V) observed with PARAS over a period of more than one year ($\sim$ 400 days). Individual velocity data points are shown in red, and nightly binned data is presented in blue.

2.3 TESS Photometric Survey

The candidates for observations with PARAS in this thesis were carefully shortlisted from NASA's space-based mission 'Transiting Exoplanet Survey Satellite (TESS),' which is designed to search for transits in stars. It was launched in 2018 and placed into a highly elliptical 13.7 days orbit around the Earth (Ricker et al., 2015). TESS possesses four identical cameras, each having a field of view (FOV) measuring $24° \times 24°$ (a total FOV of $24° \times 96°$) and a pixel scale of 21″ pixel^{-1}. It exhibits sensitivity within the 600-1000 nm wavelength range. TESS systematically covers the entire sky by dividing it into 26 sectors, with 13 sectors allocated to the northern hemisphere and the remaining 13 sectors assigned to the southern hemisphere. Each TESS sector typically being observed for $\sim$27 days, and there are some overlaps near the ecliptic poles where each TESS sector can be viewed for up to 351 days. These areas are referred to as continuous viewing zones (CVZs).

This mission was primarily scheduled for two years, in which the south-

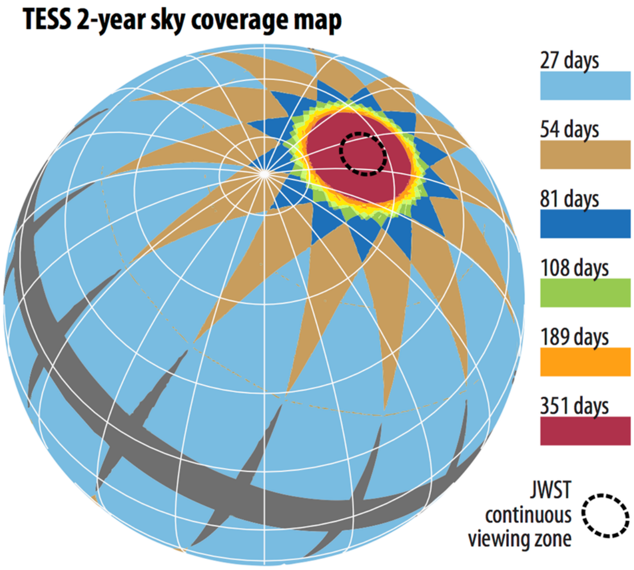

Figure 2.3: The figure displays the sky coverage map of the TESS primary mission, indicating the areas of the sky observed during the mission. The map also includes information about the observing time dedicated to each region. Image Credits: TESS MIT page.

ern hemisphere sky would be tiled in the first year and the northern hemisphere in the next year. After successfully completing the two years, the mission is now extended. The two-year sky coverage map of TESS is depicted in Figure 2.3, where colors represent its expected days of observations. During its primary mission, the spacecraft captured around 20,000 targets in postage stamps with a two minutes cadence, which were subsequently downlinked. Additionally, it obtained full-frame images (FFIs) from its four cameras, which were binned to a 30-minute cadence. TESS is now in its extended mission phase, observing more frequently. The FFIs are taken every 10 minutes, and for pre-selected 1000 specific targets per sector, there is also a new observation mode of every 20 seconds. The second phase of TESS's mission brings notable advancements. Firstly, it significantly increases the number of sectors with observed target data, thereby enhancing the reliability of previous planet discoveries and facilitating the identification of new ones. Moreover, this phase will introduce a shorter cadence for capturing FFIs. This shorter cadence allows for a larger sample of evolved hosts. Based on the current data, there is an expectation of discovering several hundred new exoplanets around evolved stars. This estimation, mentioned in studies conducted by Campante et al. (2016) and Barclay et al. (2018), is subject to variations depending on the assumed occurrence rate of such planets.

2.4 Candidate Selection Criteria for Follow-up Observations with PARAS

The candidates for this thesis work were carefully shortlisted from the TESS photometric survey, which provides a list of TESS Objects of Interest (TOIs) available on the TESS ExoFOP webpage*. These TOIs are identified as potential exoplanet-hosting star candidates. The following selection criteria were used for shortlisting the candidates for this thesis work:

- **Observability:** The candidates were shortlisted by considering their visibility in the night sky based on their celestial coordinates during the non-monsoon months of the observing season at Mt. Abu, which falls between October and May.

- **Spectral types:** To ensure precise measurements of RVs for exoplanet detection, sources with spectral types F, G, and K were chosen because they provide an adequate number of spectral lines required for precise RV measurements using the CCF technique. Insufficient spectral lines would result in reduced RV precision, thus highlighting the importance of selecting F, G, and K-type stars.

- **Magnitudes:** Sources with a magnitude brighter than ~ 10 in the V-band were specifically chosen. This magnitude serves as the limit of observations for the PARAS spectrograph used in conjunction with the 1.2 m telescope (see Section 2.2 and Section 2.6.4).

- **System properties:** Considering the current focus on detecting planets around evolved stars, the selection criteria was further refined. Candidates were prioritized based on their stellar surface gravity ($\log g_*$) of less than

*https://exofop.ipac.caltech.edu/tess/

4.1 cgs (Rodriguez et al., 2021) or stellar radius (R_*) greater than 2 $R_\odot$, as provided on the ExoFOP webpage. This criterion aids in narrowing down the sample to evolved stars, as lower surface gravity and larger stellar radii are indicative of later stages in stellar evolution.

A total of 54[†] TOIs fulfilled the abovementioned criteria, including their observability, spectral type, surface gravity and/or stellar radius, and were observable from Mt. Abu. Out of these, 19 were brighter than $V = 10$ magnitudes. Among the 19, 8[‡] were already ruled out as false positives (FPs), 2 were confirmed planets (CPs) (Schanche et al., 2020; Sha et al., 2021), and 2[‡] were found out of phase with photometric ephemeris. Therefore, at that time, only 7 out of the 19 candidates were found as planetary candidates (PCs). TESS later confirmed 1 CP (Wittenmyer et al., 2021) and 2[‡] FPs from these 7 PCs. This left us with 4 final candidates: TOI-1490, TOI-1684, TOI-1719, and TOI-1789. Over time, more candidates were released by TESS, and we shortlisted 3 more: TOI-2474, TOI-4543, and TOI-4603. Therefore, in total, 7 candidates were chosen for this thesis work, and these are listed in Table 2.3. Please note that the parameters provided in Table 2.3 are based on the ExoFOP webpage.

All of these candidates were observed with the PARAS spectrograph, and their RV measurements were obtained. Two successful giant planet discoveries, TOI-1789 b and TOI-4603 b, were made and are listed in Table 2.3. The details of these two systems are thoroughly discussed in Chapter 4 and Chapter 5, respectively. Furthermore, the remaining five out of seven candidates, namely TOI-1684, TOI-1719, TOI-2474, TOI-4543, and TOI-1490, are summarized as follows:

[†]As of the Year 2020

[‡]the TFOP working group (Collins, 2019)

Candidate ID	Magnitude (V-band)	Spectral Type	Stellar Radius ($R_\odot$)	Planetary Radius (R_J)	n_{obs} [a]	Results from PARAS
TOI-1490	9.2	K3	5.11	1.09	15	More observations required
TOI-1684	8.25	K2	2.99	0.85	16	Scattered data
TOI-1719	8.29	F9	4.17	1.19	6	Scattered data, $\Delta m = 1.8$ of stellar companion at $0.11''$
TOI-1789	9.7	F8	2.25	1.53	16	Giant planet companion found (This work)
TOI-2474	8.69	K3	3.50	0.48	8	Scattered data
TOI-4543	7.8	K1	3.19	2.24	26	Scattered data, $\Delta m = 2.6$ of stellar companion at $0.38''$
TOI-4603	9.2	F7	2.68	1.04	27	Giant planet companion found (This work)

Table 2.3: Shortlisted Candidates for PARAS observations.

[a] Observations suitable for precise RV measurements.

- **TOI-1684:** Initially alerted by TESS on January 30, 2020, in sector 19. The TESS observed a planetary radius of $\sim 0.85 R_J$, corresponding to a predicted mass of $\sim 65 M_E$ (Chen & Kipping, 2017) and a predicted K-value of ~ 32 m s^{-1}. PARAS observations took place from November 10 to December 23, 2020, resulting in 33 observations over 11 nights, with 16 spectra suitable for precise RV measurements. The SNR of the acquired spectra ranged from 15 to 18 per pixel at 550 nm. However, TOI-1684 does not exhibit any periodic variations in their radial velocities. Therefore, we had stopped observations for this star.

- **TOI-1719:** Initially identified by TESS on February 19, 2020, in sectors 20 and 21. The observed planetary radius is $\sim 1.19 R_J$, resulting in a predicted mass of $\sim 113 M_E$ and a predicted K-value of ~ 48 m s^{-1}. Subsequent PARAS observations were carried out from October 30 to November 22, 2020, comprising 9 observations over 6 nights, with 6 spectra suitable for precise RV measurements. The SNR of the acquired spectra ranged from 14 to 24 per pixel at 550 nm. Furthermore, subsequent high-resolution imaging revealed bright nearby companions with magnitude contrasts (Δm) of 1.8 magnitude, situated at separations of $0.11''$. Due to the point spread function (PSF) of the PARAS spectrograph ($\sim 1.8''$), these sources remained unresolved during PARAS observations, leading to the exclusion of TOI-1719 from the study.

- **TOI-2474:** Alerted by TESS on February 3, 2021, in sector 32, TOI-2474's TESS-observed planetary radius is $\sim 0.48 R_J$, resulting in a predicted mass of $\sim 25 M_E$ and a predicted K-value of ~ 12 m s^{-1}. Subsequent PARAS observations were taken from February 14 to December 21, 2021, comprising 13 observations over 9 nights, with 8 spectra favorable for precise RVs. The SNR ranged from 12 to 20 per pixel at 550 nm. However, TOI-2474 does not exhibit any periodic variations in their radial velocities. Therefore, we stopped observing TOI-2474.

- **TOI-4543:** Initially alerted by TESS on October 21, 2021, in sectors 42, 43, and 44. TOI-4543 has an observed radius of $\sim 2.24 R_J$, resulting in a predicted mass of $\sim 317 M_E$ and a predicted K-value of $\sim$ 113 m s^{-1}. Subsequent PARAS observations occurred from October 28 to December 28, 2021, comprising 59 observations over 16 nights, with 26 spectra favorable for precise RV measurements. The SNR ranges from 12 to 29 per pixel at 550 nm. Additionally, subsequent high-resolution imaging revealed nearby companions with magnitude contrasts (Δm) of 2.6 magnitude located at separations of $0.38''$, leading to the exclusion of TOI-4543 from the study.

- **TOI-1490:** TOI-1490 was alerted by TESS on December 05, 2019, in sector 17. The TESS-observed planetary radius is $\sim 1.09 R_J$, yielding a predicted mass of $\sim 98 M_E$ and a predicted K-value of $\sim$ 34 m s^{-1}. Subsequent PARAS observations were carried out from January 21, 2020, to October 30, 2022, comprising 25 observations over 17 nights, with 15 spectra favorable for precise RVs. The SNR of the acquired spectra ranged from 15 to 18 per pixel at 550 nm. The PARAS observations of TOI-1490 indicate the possibility of a companion with a mass of approximately $2M_J$, exhibiting a semi-amplitude of around 300 m s^{-1} in its orbit. To draw any conclusion, more data is required. Notably, this source will be visible from mid-July 2023, and the observatory will be closed due to the monsoon season (until October 2023). Therefore, the plan is to resume this source's observations starting in November 2023.

2.5 Observation Strategy

The 1.2 m PRL telescope was utilized to conduct observations on the shortlisted objects. Prior to each observing season, candidates were carefully selected in advance, considering their celestial coordinates and the local sidereal time (LST). Subsequently, the sources were scheduled in a queue for the particular night of observation. The following steps were followed during the observation process:

- Prior to starting the observations, a weather forecast was checked, and condensation levels were monitored throughout the night.

- The selection of observation intervals for a specific candidate was determined by its orbital period. For sources with longer periods (more than 8 days), observations were scheduled every alternative day. On the other hand, for sources with shorter periods (up to 8 days), spectra were taken daily at various times to achieve a well-sampled phase of the orbital period of the system.

- Spectra of stars brighter than 6 mag were captured with a 1200 s exposure time, while fainter stars were observed with 1800 s exposure. Spectra with lower SNR were excluded during RV analysis.
- The sources were observed with a planned air mass below 1.5 to ensure better SNR by avoiding high extinction.

2.6 PARAS Observations, Reduction and Analysis Procedures

2.6.1 Observations Procedure

Once the telescope has been set up for observations, the star is pointed by providing its celestial coordinates. It is necessary to focus the incoming starlight onto the star fiber so that the light can efficiently transfer to the opposite end where the spectrograph is placed. Figure 2.4 shows the process of feeding starlight into the star fiber. A CCD is kept at the same focal plane as the input fibers, represented as FP CCD in the figure. Consequently, focusing on this FP CCD ensures that the image is also focused on the fibers. This image remains at a fixed position (X, Y) on the CCD. To initially check the focus, the position of the secondary mirror is adjusted. Once the optimal position is determined, we start guiding the star by using a starfish auto guider CCD to ensure precise tracking of the star. Approximately 8% of the incoming light is fed to this guiding CCD. Now, for entering the starlight into the spectrograph, the FP CCD needs to be replaced with the star fiber. This is achieved using a PI (Physik Instrumente) motor control system, which moves the FP CCD by a pre-calculated number of steps. This step ensures that the starlight is directed to a position very close to

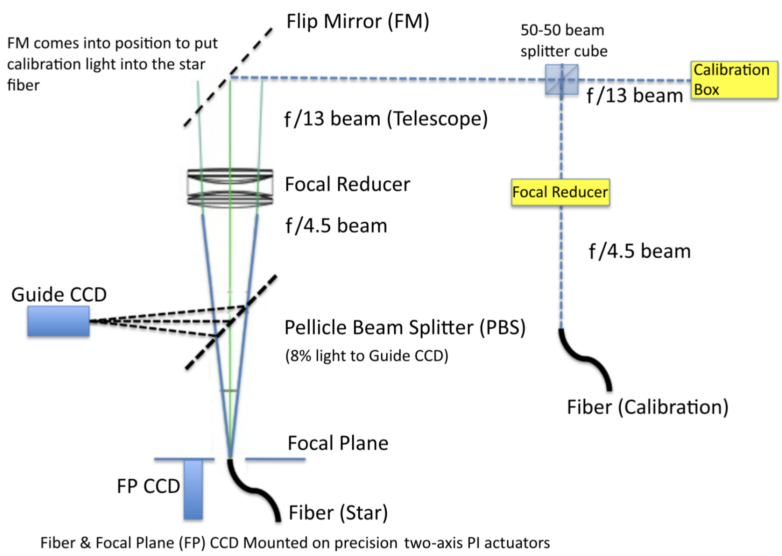

Figure 2.4: Schematic of the PARAS Cassegrain unit (not to scale) illustrating the feeding of starlight and calibration light into the star and calibration fibers, respectively. (Credits: Chakraborty et al., 2014).

the fiber. The next task is to properly align the fiber and starlight to get the maximum counts. For this purpose, a flip mirror has been placed inside the vacuum chamber between the slit position and fiber optics, and an exposure meter CCD is mounted at the spectrograph interface. Fine adjustments are made in the PI stepper motor in both directions (X and Y) to maximize the counts in the exposure meter CCD. Each star requires approximately 5-10 minutes overhead time for this process, and then the science frames are acquired.

A nightly observation log (PARAS_LOG) is maintained to record the information related to science and calibration frames, such as their exposure time, counts, and air mass during the observations. Additionally, the weather condition and technical problems, including pointing and guiding errors occurring during the observations, are also recorded in that log file.

2.6.2 Raw data Frames for Observations and Calibrations using PARAS

The spectrograph is designed to acquire spectra from two fibers simultaneously. One fiber is reserved for the star (Fiber A), while the other fiber is intended for the calibration lamp (Fiber B). Calibration frames, including Bias, Flat, and UAr/ThAr HCL frames, are acquired at the onset of each night to facilitate various corrections on the science frames obtained from the PARAS. For this thesis work, both the ThAr and UAr HCL are utilized, but since the process is the same for both, we will refer to the UAr HCL from this point onward. Bias exposure is required for bias subtraction, while the Flat frame is crucial for locating and extracting orders from the two fibers. To acquire flats, PARAS uses a Tungsten lamp, and separate exposures of Tung+Dark and Dark+Tung are taken for order definition of Fiber A and Fiber B, respectively. Moreover, data acquired from UAr HCL requires two types of frames: Dark+UAr and UAr+UAr. The Dark+UAr is used for scattered light subtraction, especially to remove the effect of bright argon lines bleeding into the star orders. UAr+UAr is necessary for tracking instrumental drifts during the night and between nights, as it allows for accurate wavelength calibration. The raw frames acquired from the PARAS spectrograph are depicted in Figure 2.5. Additionally, Figure 2.5(e) displays spectra taken from PARAS around 550 nm with the HD 55575 star spectra in Fiber A and the UAr HCL spectra in Fiber B.

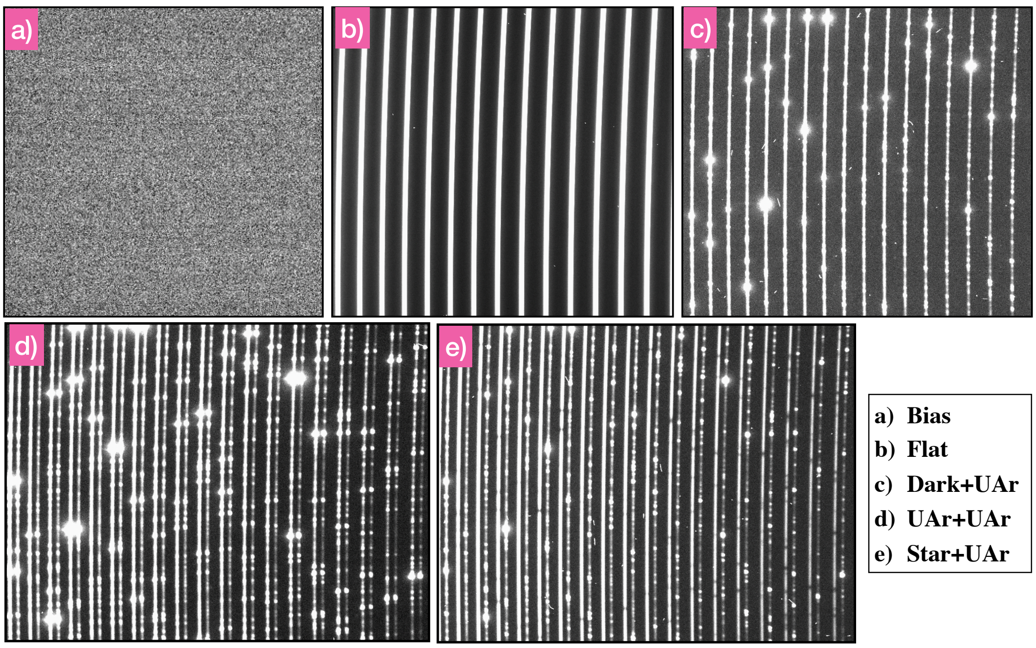

Figure 2.5: Raw data frames acquired from PARAS for observations and calibration. The Figure e) presents the spectra of HD 55575 around 550 nm.

Furthermore, the reduction and extraction of PARAS spectra involves the utilization of two pipelines: the data reduction pipeline (`PARAS_PIPELINE`) and the data analysis pipeline (`PARAS_ANALYSIS`) (Chakraborty et al., 2014). These pipelines use a set of image-processing algorithms written in IDL and are employed sequentially to process and analyze the acquired data, enabling the extraction of valuable spectra for further study. More details of the key constituents of these pipelines are presented below.

2.6.3 Data Reduction pipeline

The PARAS data reduction pipeline (`PARAS_PIPELINE`) generates spectra that are arranged in pixel-order space. The core of this pipeline is the `REDUCE` package developed by Piskunov & Valenti (2002) that processes and extracts the cross-dispersed echelle spectra. Further, it has been tailored to fulfill the specific requirements of the PARAS spectrograph.

Before each night's observations, composite calibration frames are taken, and master frames are generated from them. To produce a master bias frame, the nightly bias frames are divided into two groups and compared to measure the bias shifts and monitor the effects of read noise, and identifying any outliers. The resulting master bias frame is then used to correct the bias in all non-bias images by subtracting it from them. Furthermore, a master flat is generated by combining all available flat frames. In order to extract spectra with minimal continuum, the locations and curvature of echelle order are determined empirically based on a high-quality flat-field frame. The `REDUCE` package (Piskunov & Valenti, 2002) offers an algorithm to locate spectral orders in two-dimensional spectroscopic data robustly. This algorithm follows a four-step process. It starts by identifying the possible spectral order pixels and then examines their level of clustering. Next, these partial orders are merged, eliminated, and ultimately fitted. Given the significant number of spectral orders in PARAS, the algorithm's performance is enhanced by creating a mask that excludes low signal corners and bad pixels from the image extraction process. As PARAS is a very stable spectrograph, a master order trace is created using a median flat field image, which is then incorporated into the automated pipeline. The user's intervention is required only in a few cases where a decision must be made about merging or rejecting clusters. Further, the method outlined in van Dokkum (2001) is used for the cosmic ray correction in the data. It employs a robust algorithm based on the variation of Laplacian edge detection. This algorithm effectively identifies and removes cosmic rays of different shapes and sizes, distinguishing them from undersampled point sources with high confidence.

Moreover, in order to extract the optimal spectra, it is crucial to estimate and subtract the background caused by scattered light. However, measuring the background below an order directly is not possible. To address this, interpolation of the background between orders is performed to obtain a reliable estimate. This estimation accounts for sky emission but cannot account for ghosts or highly intense emission lines. The ghost artifacts are not present in the spectrograph, even when strong argon lines are present beyond 700 nm, and also bright argon lines bleeding at wavelengths greater than 700 nm are restricted using a filter. For orders that are not completely cured, a bleeding map is used, which is linearly scaled by a global parameter that describes variations in lamp brightness, similar to Lovis & Pepe (2007).

The extraction of spectra is accomplished by the `REDUCE` package through the use of a decomposition routine. The routine involves dividing the image into swaths and separating the spatial profile from the spectrum for each column. Initially, an estimated spectrum is generated, and the spatial profile is fitted using a noise model and an empirically determined mean spatial profile. Once the change in the deduced spectrum reaches a minimal value (smaller than 0.002 in this case), the iteration process terminates, resulting in the best possible slit function and spectrum. Following the completion of the above procedures, the obtained data is commonly referred to as the reduced data.

2.6.4 Data Analysis pipeline

Once the data is fully reduced, the PARAS analysis pipeline (`PARAS_ANALYSIS`) can be initiated. The following processes will conclude in radial velocities from the reduced data.

- **Wavelength calibration:** The acquired spectra from the PARAS PIPELINE are in pixel space, which is to be converted into wavelength space through the wavelength calibration process. This calibration is achieved by comparing the spectra of UAr HCL with a template of suitable Uranium lines. Previously, the standard ThAr HCL was used for wavelength calibration in the PARAS spectrograph, but as it is no longer commercially available, UAr HCLs are now utilized. A study by Sarmiento et al. (2018) indicated that Uranium could be a precise replacement for Thorium in ThAr and Thorium-Neon (Th-Ne) HCLs for wavelength calibration in the visible and near-infrared (NIR) range. This is attributed to Uranium having a greater number of lines than Thorium in both wavelength regions. For the PARAS spectrograph (R∼67000), Sharma & Chakraborty (2021) identified 1540 well resolved Uranium lines in the 380.9 – 683.3 nm wavelength range. Analysis of the PARAS spectrograph performance (with UAr HCL) showed an inter-fiber drift of 88 cm s^{-1} over 6.5 hours and an RV dispersion (σ_{RV}) of 3.2 m s^{-1} for the RV standard star, HD55575, over ∼450 days. These results align with past measurements using ThAr HCL, confirming that a ThAr HCL can be replaced by UAr HCL for precise wavelength calibration in RV measurements. Now, to perform the calibration for a specific order in the UAr HCL spectrum, the pixel position of the central wavelength for each line is identified, and a Gaussian fit is applied to precisely determine the line position in terms of pixels. These fitted pixel positions, along with the corresponding line's central wavelengths for that order, are then used to fit a third-order polynomial. The resulting polynomial provides the wavelength solution for that particular order, which is then applied to the observed stellar spectra. This process is repeated for all orders, ensuring wavelength calibration for the entire spectrum.

- **Instrumental drift correction:** Throughout the night, we take calibration lamp exposures (UAr+UAr) at regular intervals. As both fibers (Fiber A and Fiber B) traverse the same opto-mechanical elements and encounter similar changes in pressure and temperature, then the drift in each fiber should be similar. To determine the instrumental drift, a weighted binary mask consisting of intense Uranium lines is used. This Uranium mask is shifted against each spectral order, and the CCF is computed. By combining the resulting CCFs and fitting a Gaussian peak, we can accurately determine the absolute drift value. Subsequently, the resulting wavelength solution is applied to the observed stellar spectra. Now, to calculate the inter-fiber drift, we apply the same mask to the UAr+UAr spectra of both fibers and observe the difference between them, which is then applied to the observed stellar spectra. Hence the instrumental drift is corrected.

- **Barycentric correction:** Precise RV or Doppler measurements are affected by multiple factors related to the Earth's rotational and orbital motion, the motion of the solar system relative to the target star, and the observer's location in relation to the barycenter of the solar system. To account for these effects and obtain accurate Doppler measurements, 'barycentric corrections' are applied. In order to apply the barycentric correction to any target star observed with PARAS, we rely on the methodology presented by Wright & Eastman (2014).

- **Producing radial velocities:** The RV of an observed star at a specific epoch is determined by performing a cross-correlation between its spectra and a suitable numerical template mask of the same spectral type. This mask is created particularly from high signal-to-noise ratio or synthetic data (Baranne et al., 1996). This comprises the value zones from 0 to 1, whereas the non-zero zones correspond to the theoretical locations and widths of absorption lines at zero velocity .

  The CCF is generated by shifting the mask as a function of the RV and is given by Pepe et al. (2002)–

$$CCF(V_R) = \sum_i \int S(\lambda) M_i(\lambda_{V_R})\, d\lambda = \sum_i CCF_i(V_R) \tag{2.4}$$

  Where, S(λ) is the acquired spectrum, M is numerical mask, and λ_{V_R} is

Doppler shifted RV. The mask M can be expressed as the sum of M_i where i refers to the absorption line.

Since the spectral lines have different relative depths. As a result, strong and deeper lines intrinsically contain more RV information than weak lines. To account for this, Pepe et al. (2002) introduced a cross-correlation function (CCF^w) that incorporates the appropriate weighting of each spectral line in the mask:

$$CCF^w(V_R) = \sum_i CCF_i(V_R).w_i \tag{2.5}$$

For a given amplitude of CCF_i, the noise on each point of the CCF can be determined with the Gaussian fit, which results as

$$\sigma_i^2 \propto S_i \propto \frac{CCF_i}{c_i} \propto \frac{1}{c_i} \tag{2.6}$$

and the weight assigned to each individual CCF_i is

$$w_i = \frac{1}{\sigma^2} = c_i \tag{2.7}$$

Where c_i is the relative depth of each absorption line. The weighted mask lines, with a width of 3 km s^{-1}, take into account the characteristics of the star to determine their depths. As a next step, we start by supplying an initial estimation of the star's RV in order to initiate the algorithm of `PARAS_PIPELINE` for obtaining precise radial velocities.

The spectra are cross-correlated with a mask of the same spectra type to calculate the CCF for individual orders. Subsequently, the CCFs of all the orders are then combined and fitted using a Gaussian function, allowing the determination of the RV of the spectra at that particular epoch (Roy et al., 2016). Finally, the obtained RV values are plotted against their corresponding time.

Combined RV uncertainties: In PARAS data, along with the photon noise error (as mentioned in Section 2.2), there are CCF fitting errors associated with the RV measurements which are estimated using a statistical approach. For a spectrum, the signal (N) on each pixel is randomly varied within the Poissonian uncertainty $\pm\sqrt{N}$, and the CCF is then computed. This process is repeated 100 times for each spectrum, and the 1σ uncertainty on the CCF fitting is obtained from the standard deviation of the distribution of the resulting RV values. Consequently, the errors in RVs are determined by the square root of the quadrature sum of photon noise and statistical errors.

2.7 PRL's 0.43 m Telescope

In addition to RV observations, we carried out ground-based transit follow-up observations using PRL's 0.43 m telescope, which is also situated at Mt. Abu Observatory, PRL, India. The telescope (`CDK17 from PLANEWAVE`[§]) has a focal ratio of $f/6.8$ and focal length of 2939 mm. Its standout features are the absence of coma, off-axis astigmatism, and field curvature, ensuring that the stars appear as pinpoint light sources across its 70 mm image circle. It is equipped with a

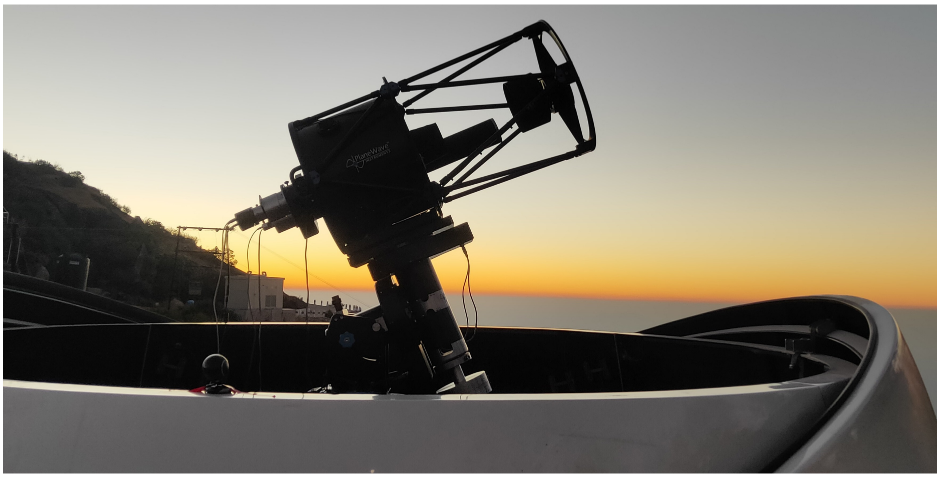

Figure 2.6: Image showing 0.43 m telescope at PRL Mt. Abu Observatory.

fixed primary mirror, which provides simple secondary mirror collimation. The telescope's overall design and construction make it acquire good-quality images, making its operation user-friendly. The image depicted in Figure 2.6 showcases the PRL's 0.43 m telescope. Moreover, for the transit observations with 0.43 m

[§]https://planewave.com/product/cdk17-ota/

Specifications	`TRIUS PRO-814`	`ANDOR iKon-L 936`
Manufacturer	Starlight Xpress Ltd.	Oxford Instruments
Sensor type	Monochrome ICX814AL (Interline CCD)	e2V CCD42-40 (BEX2-DD)
Image format (pix)	3388 x 2712	2048 x 2048
Pixel size (μm)	3.69	13.5
QE (at 580 nm)	$\sim$ 77%	$\geq$ 90%
Dark current (e^-/s/pix)	$\leq$ 0.002 at $-10\,^{\circ}$C	0.006 at $-80\,^{\circ}$C
System gain (e^-/ADU)	0.25	1
Readnoise	$3e^-$ at 3 MHz	$7e^-$ at 1 MHz

Table 2.4: Specifications of both the CCDs

telescope, two CCDs were used, `TRIUS PRO-814` (TRI) CCD[¶] and `ANDOR iKon-L 936` (ADR) CCD[‖]. The TRI is a low-cost CCD and has a field of view (FOV) of $14.6' \times 11.7'$ with a pixel scale of $0.26''$. ADR has a FOV of $32' \times 32'$ with a pixel scale of $0.95''$. The key specifications of both CCDs can be found in Table 2.4.

Furthermore, once planet-like variations are detected in the RVs of a star, the subsequent step involves determining whether these variations are indeed caused by the presence of an actual planet. Previous observations have shown that stellar activity (such as starspots, plages, etc.) can generate RV variations of a magnitude comparable to those produced by hot Jupiters, typically on the order of a few tens of m s^{-1} (Queloz et al., 2001; Martínez Fiorenzano et al., 2005; Perger et al., 2017; Simola et al., 2019; Meunier, 2021). The upcoming chapter will focus on discussing a method employed to determine the origin of these RV variations.

[¶]https://www.sxccd.com/product/trius-sx814/

[‖]https://andor.oxinst.com/products/ikon-xl-and-ikon-large-ccd-series/ikon-l-936

Chapter 3

Radial Velocity Variations and Line Bisector Analysis

3.1 Introduction

The spectral lines observed in the star's spectra result from a combination of factors such as absorption, emission, scattering, and the movement of gases within the stellar atmospheres across the differentially rotating stellar disk. These lines change their centroid position due to the center of mass motion of the star, leading to variations in the star's radial velocity (Chapter 1). These variations serve as evidence for the presence of planetary or stellar companions orbiting the star. However, the presence of magnetic fields in the stellar atmosphere causes a number of inhomogeneities (referred to as stellar activity jitter) contributing to asymmetries in the spectral lines (Saar & Donahue, 1997; Santos et al., 2000; Wright, 2005; Dumusque, 2014; Davis et al., 2017; Simola et al., 2018). Due to these line asymmetries, the same RV variations are observed from the star, which falsely indicates that they are caused by shifts in the centroid positions, leading to false planet detection (Queloz et al., 2001; Desidera et al., 2004; Martínez Fiorenzano et al., 2005; Robertson & Mahadevan, 2014; Rajpaul et al., 2015; Robertson et al., 2015; Lubin et al., 2021). As a result, it is crucial to carefully account for and distinguish between genuine planetary signals and those arising from stellar activity jitter when detecting planetary companions around stars.

This chapter begins by discussing different types of stellar activity jitters and their associated timescales. Then, it introduces the line bisector analysis tool and discusses line profile asymmetries. A Python script based on existing literature is developed for conducting line bisector analysis on the selected candidates for PARAS observations. Finally, the chapter presents the results obtained from the line bisector analysis.

3.2 Stellar Activity

Stellar activity encompasses a wide range of dynamic processes occurring within a star, where magnetic fields and turbulent plasmas interact in its interior. This interaction can amplify the strength of magnetic fields, leading to increased energy release in the form of heat, non-thermal particles, or kinetic energy (Pagano, 2013). Consequently, these interactions give rise to the formation of active regions, which includes star spots, plages, faculae, flares, etc. (Piddington, 1983). These are the temporary features appearing in different regions of the stellar atmosphere. For instance, spots are visible in the photosphere as dark zones due to their lower temperature compared to the surrounding areas. Faculae, which are bright zones, are generally observed near spots in the photosphere. Moving to the chromosphere, plages manifest as bright regions near spots and are visible in monochromatic light of specific spectral lines, such as Hα or Ca II. Flares are characterized by their sudden and powerful energy releases, which occur when there is a disruption in the stellar chromosphere (Meunier, 2021). The activity phenomena described above show temporal variations on different timescales (Pagano, 2013; Maldonado et al., 2019). Flares typically last for a few minutes or hours without showing regular periodicities. The spots and plages on the photosphere of the star have lifetimes typically spanning weeks to months (Castenmiller et al., 1986; Maldonado et al., 2019). However, there are exceptional cases where certain stars maintain a relatively constant distribution of spots even over extended periods, even lasting several years (ζ Boo A, Toner & Gray, 1988; Gray, 1988). Along with the formation of active regions, granulation (where hot plasma rises, cools, and sinks, forming bright granules and dark intergranular lanes, Cegla et al., 2019; Meunier, 2021), and the magnetic cycle (Makarov, 2010) of the stars also results in stellar activity jitters in the RVs of the stars. Granulation lasts for about 10 minutes to 2 days, while the magnetic cycle spans years (Meunier & Lagrange, 2013).

3.2.1 Line Profile Asymmetries due to Stellar Activity

Line profile asymmetries due to stellar activity refer to changes in the shape or asymmetry of spectral lines observed in a star's spectrum. These variations result from various activity-related phenomena occurring in the star's atmosphere, such as active regions (e.g., star spots and plages), granulation, flares, and magnetic cycles. As the star rotates, different regions with varying Doppler shifts contribute to the observed line profiles, leading to asymmetric shapes. The RV amplitude of variations caused by the active regions can be in the range of 1–200 m s^{-1} (Hatzes, 2016; Maldonado et al., 2019). Some studies also have confirmed the artifact of stellar activity on the stars. For example, RV variations: $\sim$ 80 m s^{-1} on HD-166435 star (Queloz et al., 2001), $\sim$ 10 m s^{-1} on 219542 B star (Desidera et al., 2003), $\sim$ 3.9 m s^{-1} on GLIESE 667C star (Robertson & Mahadevan, 2014), and $\sim$ 2.13 m s^{-1} on Kapteyn b (Robertson et al., 2015) were observed. On the other hand, granulation, flares, and the magnetic cycle of the stars can induce the RV variations on the order of $\sim$0.4 m s^{-1} (Cegla et al., 2019), $<$ 1 m s^{-1} (Meunier, 2021), and up to 20 m s^{-1} (Makarov, 2010; Dumusque et al., 2011; Dumusque, 2012; Meunier & Lagrange, 2013), respectively.

In the case of hot Jupiters, the RV amplitude of the stars ranges from a few tens of m s^{-1} to a few hundreds of m s^{-1}. Therefore, the active regions (e.g., dark spots) produce a challenge while detecting hot Jupiters. The presence of spots and bright plages on a star's surface can vary in size and evolve over time. They are coupled with the star's rotation and have significant effects on RV measurements, with the most notable impact arising from the flux deficit (or excess) in these regions. As the star rotates, this flux deficit (or excess) moves from the blueshifted to the redshifted part of the stellar disk. Consequently, it alters the shape of spectral lines and introduces periodic variations in measured RVs that align with the stellar rotation period (Figure 3.2). For studying the origin of RV variations measured on stellar spectra, the 'line bisector' diagnostic tool is commonly used.

3.3 Line Bisectors from the Stellar Spectra

The line bisector detects changes in the shape of spectral lines (or CCFs). This section discusses the analysis procedure for the line bisectors, which is based on the methods outlined in Queloz et al. (2001) and Martínez Fiorenzano et al. (2005). This method eliminates the need for additional observation time required for acquiring separate spectra. Line bisectors also provide a significant advantage over other indirect observables, for example, activity indicators, in comprehending the origins of RV variations. This is because the line bisectors are directly derived from the same data used for measuring RVs—the spectral lines (or CCFs) profile and provide a more direct and accurate means of identifying contamination by stellar companions, which cannot be obtained through activity indicators alone. The following subsections discuss the determination of line bisectors and their associated errors, along with the discussion on the origin of RV variations in the stars.

3.3.1 Determining the Line Bisector

The bisector of an absorption line or a CCF refers to the middle point of the line profile where the flux values on the left and right sides of the line are equal. In our case, we use CCFs of the spectra. The determination of the line bisector involves a few basic steps. First, the ordinate axis of the CCF is adjusted to a suitable scale. Then, the values in velocity corresponding to the left and right points for a specific flux value are identified. This process is achieved by interpolating the CCF, which allows for the precise determination of these points on the desired scale. To further investigate line bisectors, a parameter called the bisector velocity span (BVS) is calculated, which is discussed in the next subsection.

3.3.2 Bisector Velocity Span

The BVS serves as a measure of the slope and curvature of the line bisector, as studied by Toner & Gray (1988). The line bisector has two distinct regions

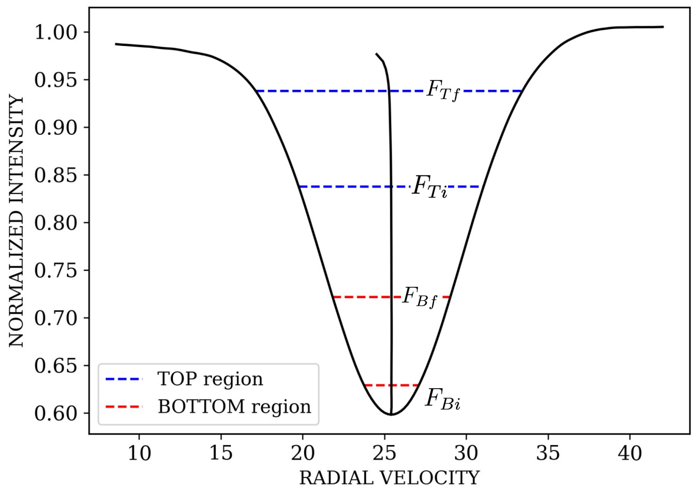

Figure 3.1: Schematic representation of CCF and its bisector for one of the stars observed with PARAS.

within the absorption profile: a top zone near the wings and a bottom zone above the core (see Figure 3.1). These regions are defined by their initial and final flux values (F_{Ti}, F_{Tf}) for the top zone and (F_{Bi}, F_{Bf}) for the bottom zone. The bottom zone is centered around 87% above the core, while the top zone is centered around 25% near the wings (Martínez Fiorenzano et al., 2005). These selected regions represent the places to study the velocity given by the bisector. By calculating the average velocities in the top zone (V_t) and the bottom zone (V_b) and taking their difference ($\bar{V}_t - \bar{V}_b$), the bisector velocity span or BVS can be obtained.

3.3.3 Determining Errors in BVS

To estimate the errors in the BVS, an approach outlined by Gray (1988) was followed. The authors determine the bisector error coming from photometric error:

$$\delta V = \frac{1}{\sqrt{2}} \frac{\delta F}{(dF/dV)} \tag{3.1}$$

Here, the wavelength error in the velocity scale is denoted by δV, and the flux F has a photometric error represented by δF. dF/dV gives the slope of the profile. The expression for the photometric error is determined by considering the noise present in the absorption line. The noise is given as:

$$\frac{1}{\frac{S}{N}\sqrt{F}} \tag{3.2}$$

Where $\frac{S}{N}$ represents the signal-to-noise ratio of the spectrum and the fraction of pixel is given by following quantity:

$$\frac{\Delta F}{x\frac{dF}{dV}} \tag{3.3}$$

The final expression for the photometric error, by taking into account the interval flux (ΔF) where the bisector is being computed and x representing the linear dispersion of the spectrograph, is given as follows:

$$\delta F = \frac{1}{\frac{S}{N}} \frac{1}{\sqrt{n\Delta F x \frac{dF}{dV} F}} \tag{3.4}$$

Where n is the number of lines employed in the mask for the CCF.

By substituting equation 3.4 into equation 3.1, the following expression can be obtained:

$$\delta V = \left(\frac{S}{N}\right)^{-1} \left(2nF\frac{\Delta F}{x}\frac{dF}{dV}\right)^{-1/2} \tag{3.5}$$

Where F represents the central flux of the analysis zone (top or bottom).

In this context, it is feasible to calculate the errors for V_t and V_b based on the CCF profile. An appropriate error bar can be calculated for the BVS by assuming that it is determined by the square root of the sum of the squares of δV_t and δV_b (i.e., $\sqrt{\delta V_t^2 + \delta V_b^2}$).

By calculating the BVS along with its associated error bars, we can examine the correlation between the RV of the CCF and the orientation of the line bisector (or its BVS). If a correlation is found, it will cast serious doubts on the reflex-motion interpretation of the RV variations.

3.3.4 Correlation and its Interpretation

Two types of linear correlation can be observed between the RV variation and BVS. The first type is characterized by a negative slope, typically found in active stars, indicating the presence of starspot(s) crossing the stellar surface as it rotates. Figure 3.2 schematically (not to scale) represents this asymmetry in the line caused by the presence of spots. Since the RV computation is based on measuring the spectral line centroids, which can be affected by the spots. If a

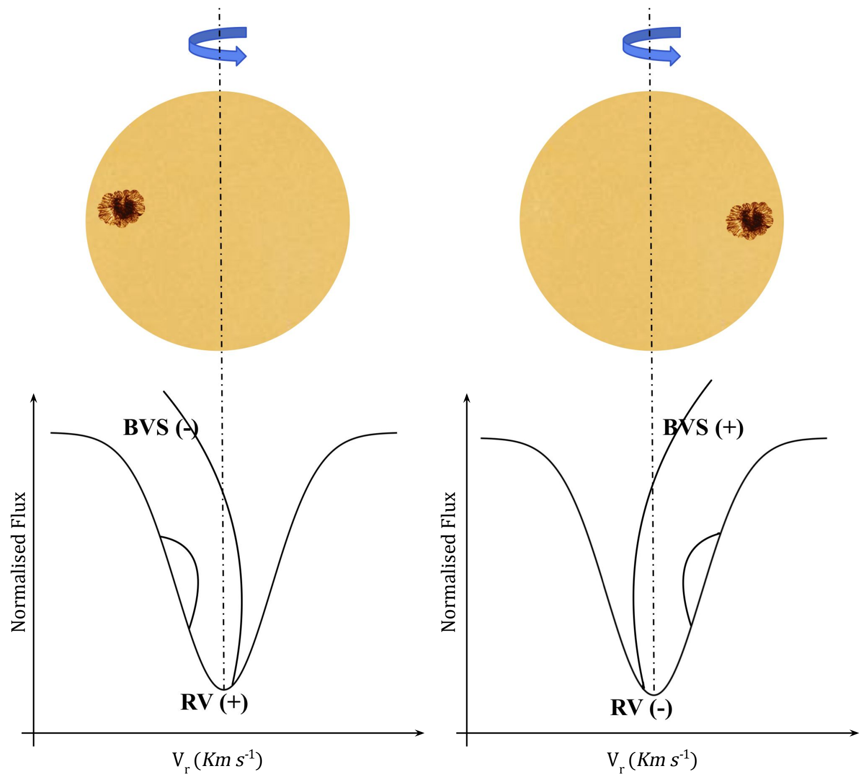

Figure 3.2: A schematic representation of rotating stars with spots, resulting in asymmetric CCF profiles. Specifically, when the spot is located on the left side and moving towards the observer, line asymmetry is observed in the bluer portion of the line, and vice versa. The figure also shows line bisectors. A negative correlation is seen between RV variation and BVS.

spot is located in the red wing of the profile (upper right in Figure 3.2), it will cause a shift towards more negative RV values in the line centroid (bottom right in Figure 3.2). Due to the shape of the line bisector, the BVS will predominantly yield positive values, resulting in an anti-correlation in the BVS-RV plot. Similarly, if a spot is present in the blue wing of the profile, a similar behavior will occur, but with an opposite sign.

The second type exhibits a positive slope, which arises from spectral contamination caused by light originating from a nearby object. In our specific case, this contamination arises from the stellar companion in the observed binary system. When there is contamination, the absorption line of the observed star

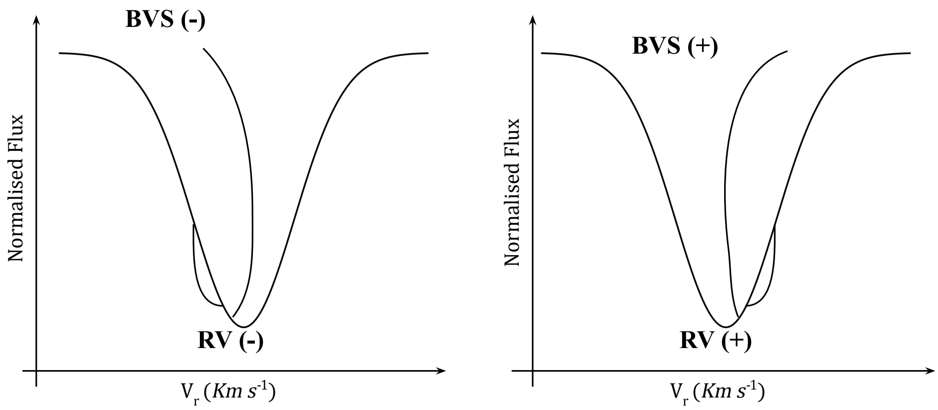

Figure 3.3: Schematic representation of asymmetric absorption profiles and line bisectors due to contamination, showing a positive correlation between RV variation and BVS.

will have a weak extra absorption feature overlaid on it (Figure 3.3). If the extra absorption feature appears on the blue (or red) side of the absorption line, the central position of the line will move towards the blue (or red) side as well. This shift leads to negative (or positive) values for RV. Consequently, there is a positive correlation between the BVS and RVs. If there is a lack of correlation between BVS and RV, it suggests that the variations in RV are attributed to the presence of the planets around the star.

Based on the algorithm discussed above, we also have developed a Python package for conducting line bisector analysis on the PARAS data. To ensure the reliability and accuracy of the code, initial validation was performed on SOPHIE archival data.

SOPHIE archive: SOPHIE is a cross-dispersed echelle spectrograph mounted on the 1.93-m telescope at the Observatoire de Haute-Provence (OHP; Perruchot et al., 2008; Bouchy et al., 2013). It is attached to the Cassegrain focus via two distinct optical fiber sets, offering different spectral resolutions (HE mode, R = 40000; HR mode, R = 75000). The spectra cover the wavelength range of 387.2 to 694.3 nm. The RVs are calculated via the CCF technique that achieves high precision (down to 2-3 ms^{-1}) using simultaneous Thorium calibration for late F, G, K, and M-type stars depending upon the SNR. All data taken with SOPHIE (raw and reduced data) are fully protected for one year, after which it is made available to the community. The current database version enables users to query and receive a list of existing observations for specific objects. It includes links to extracted (e2ds) and reconnected (s1d) spectra, cross-correlation functions, and public radial velocity measurements. More information about the data can be obtained on the SOPHIE archive page*.

Furthermore, the bisector analysis code was applied to data of an active star, 'HD 166435', and the planet-hosting star '51 Pegasi'. Subsequently, the code was applied to determine the line bisectors of the selected candidates observed with PARAS. Finally, the results are presented and discussed.

3.3.4.1 HD 166435

The dwarf star HD 166435 is characterized as a G1 spectral type with a visual magnitude (V) of 6.8 (White et al., 2007). It exhibits noticeable variations in RVs, shows photometric variability, and is found magnetically active. Previous studies have revealed a strong correlation between its RVs and orientation of line bisectors (BVS) (Queloz et al., 2001). Due to the large amplitude and consistent nature of the RV variations induced by stellar activity, this star represents an excellent candidate for evaluating our code. The line bisectors were derived for this star using processed data obtained from the SOPHIE archive. Figure 3.4 illustrates the plot of BVS against RV, clearly displaying the correlation. The

*http://atlas.obs-hp.fr/sophie/intro.html

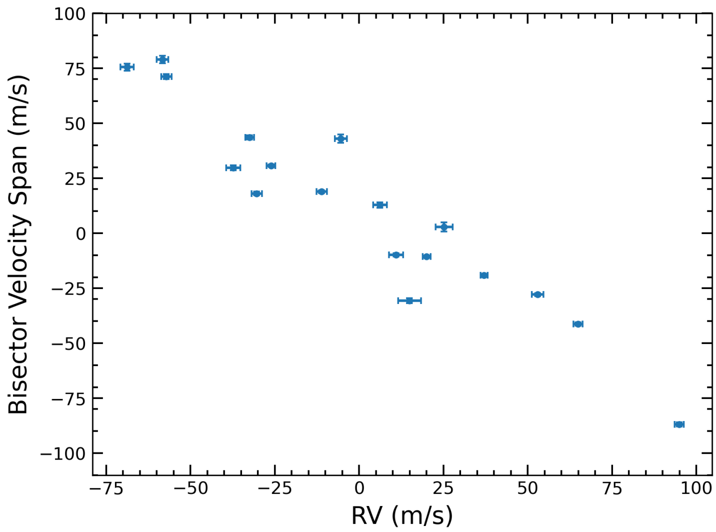

Figure 3.4: Line bisector analysis of active star HD 166435. The data was taken from the SOPHIE archive. A high correlation was observed between RV and BIS (correlation coefficient = -0.95, p-value = 1.63e-09).

values of BVS and RV for individual spectra, along with their respective error bars, are presented in Table 3.1. The correlation coefficient was calculated to be -0.92 with a p-value of 1.63e-09, indicating a strong negative correlation.

3.3.4.2 51 Pegasi

51 Pegasi holds a significant place in exoplanetary science as it was the first solar-type star discovered to host a planet. It is classified as a G2 spectral-type star with a visual magnitude (V) of 5.5 (Keenan & McNeil, 1989). This star falls within a region populated by stable objects with minimal variability on the Hertzsprung-Russell (HR) diagram, as noted by Eyer & Grenon (1997). Henry et al. (2000) indicates that over a span of five years, there have been no measurable changes observed in the star's mean magnitude. The Ca II record also showed a consistently steady signal, despite slight seasonal variations, suggesting a generally low level of stellar activity. For the line bisector analysis, the processed data from the SOPHIE archive for 51 Pegasi was used. The results confirmed the findings of Hatzes et al. (1998) and Povich et al. (2001), as there was no significant correlation observed between BVS and RV (correlation coefficient = 0.10, p-value = 0.52). The values and distribution of BVS and RV for

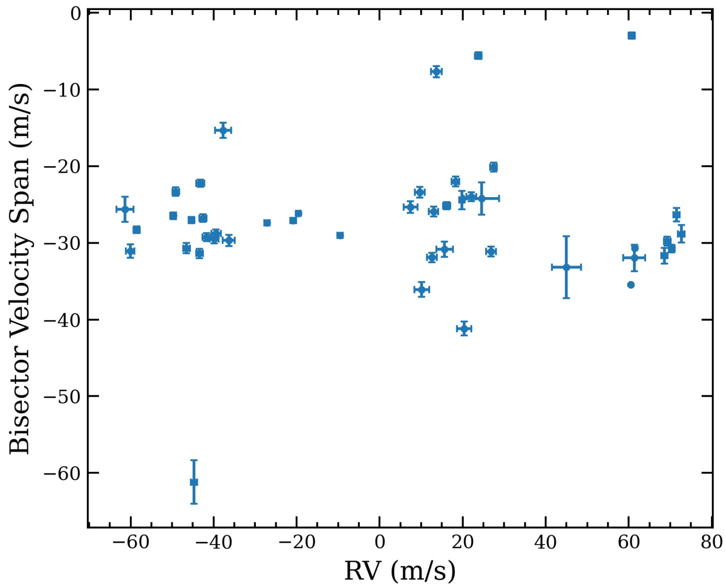

Figure 3.5: Line bisector analysis of planet-hosting star 51 Pegasi. The data was taken from the SOPHIE archive. No significant correlation was observed between RV and BVS (correlation coefficient = 0.10, p-value = 0.52).

individual spectra can be found in Table 3.2 and Figure 3.5, respectively.

Following the successful validation of our code, the line bisectors package was applied to the selected candidates for this thesis. The line bisector analysis is specifically conducted in cases where variations in RV are observed in the stars. Notably, RV variations were detected in three out of the seven selected candidates for this thesis. In the subsequent subsection, the results obtained from applying the bisector analysis to these specific sources are presented and discussed.

3.3.4.3 TOI-1789

TOI-1789 is a metal-rich late F-type slightly evolved star that has a visual magnitude of 9.7. For more detailed information about this star, please refer to Section 4.4.1. We obtained a total of 16 spectra of TOI-1789 and estimated their corresponding RV values. By conducting the line bisector analysis, we derived the values of BVS for each individual spectrum, which can be found in Table 4.4. Figure 3.6 displays the distribution between the BVS and RVs. The analysis reveals no significant correlation between the two parameters (correlation coefficient ≈ 0.15, p-value = 0.58), supporting the presence of a planetary companion around it.

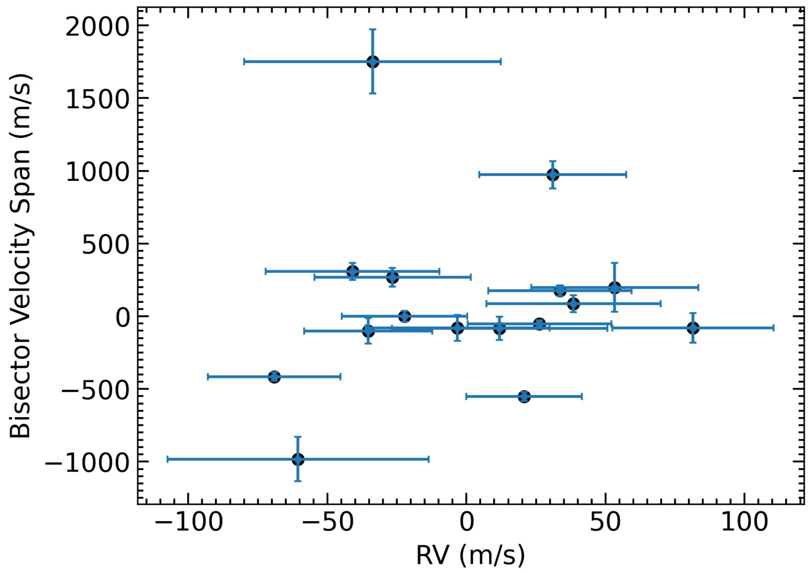

Figure 3.6: Bisector analysis plot of TOI-1789, using PARAS data, indicates that no significant correlation exists between RV and BVS (Correlation coefficient ≈ 0.15, p-value = 0.58).

3.3.4.4 TOI-1490

TOI-1490 is classified as a K-type giant star with a visual magnitude of 9.2. A set of 15 spectra for this particular star was obtained with PARAS, which revealed noticeable variations in RVs ($\sim$ 300 m s^{-1}), indicating the presence of $\sim 2M_J$ companion. No significant correlation (correlation coefficient ≈ -0.32, p-value = 0.23) between its BVS and RV was identified by applying the line bisector analysis to the available data. Figure 3.7 shows their distribution. However, it is important to note that our data coverage does not span the entire phase of the RV curve (see Chapter 2 for more details). Therefore, to draw conclusive findings, it is necessary to acquire additional data that can provide a more clear picture.

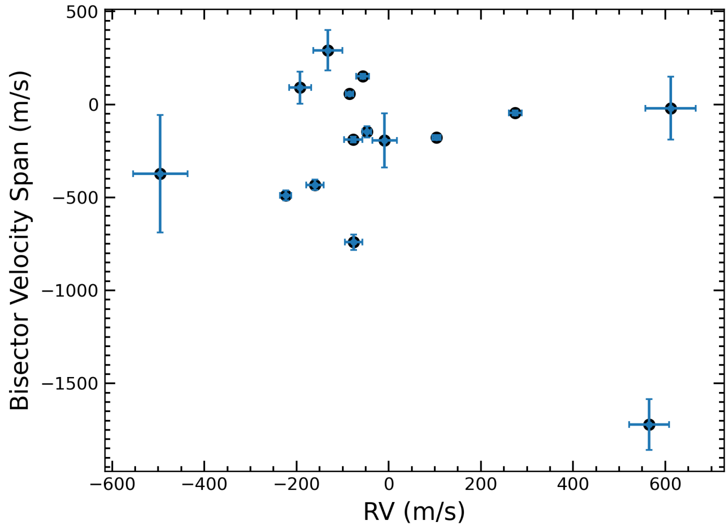

Figure 3.7: Plot of Bisector analysis of TOI-1490 from PARAS data. No significant correlation can be seen between BVS and RVs (correlation coefficient ≈ -0.32, p-value = 0.23).

3.3.4.5 TOI-4603

A total of 27 spectra of TOI-4603 were observed from the PARAS spectrograph. TOI-4603 has a visual magnitude of 9.2 and is a late F-type sub-giant star with a metal-rich composition.

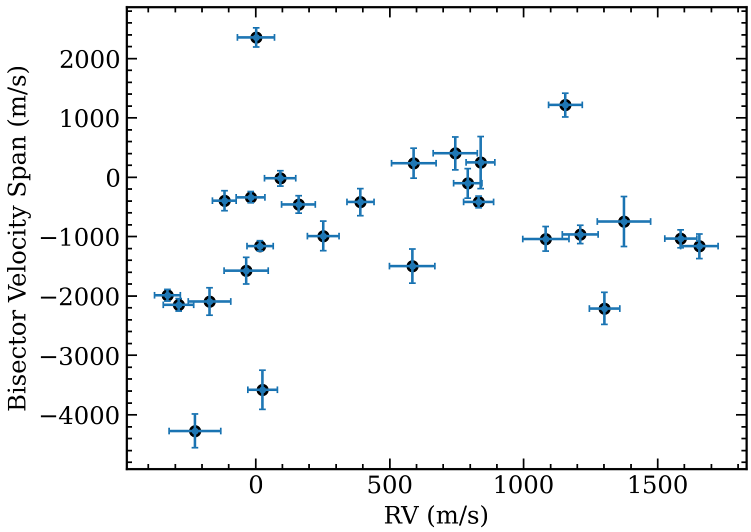

Figure 3.8: Plot of bisector analysis for TOI-4603, based on PARAS data, revealed no significant correlation between RV and BVS (Correlation coefficient ≈ 0.24, p-value = 0.23).

For more detailed information about this star, please refer to Section 5.3.1. The values of BVS were derived for each individual spectrum through the bisector analysis are listed in Table 5.1. The distribution of BVS and RV is illustrated in Figure 3.8. No significant correlation between BVS and RV was observed (correlation=0.24, p-value=0.23). This finding further supports the presence of a planetary companion around TOI-4603.

3.4 Summary

In this chapter, we have discussed the impact of line asymmetries on RV variations and explored the utilization of line bisectors to identify the origin of these variations. Specifically, the correlation between BVS and RVs was investigated for this purpose. Subsequently, the findings from the line bisector analysis of TOI-1789, TOI-4603, and TOI-1490 were discussed, as these stars exhibited RV variations. The analysis revealed no significant correlations between BVS and RV for these stars. These results suggest the presence of planetary companions around these stars, as the absence of a significant correlation implies that the RV variations are likely induced by the gravitational influence of planets rather than other sources.

3.5 Appendix

3.5.1 Tables

BJD_{TDB}	Relative-RV	σ-RV	BIVS	σ-BVS
Days	m s^{-1}	m s^{-1}	m s^{-1}	m s^{-1}
2456766.641862	2.80	2.14	25.18	2.51
2456767.634728	18.91	0.66	-11.13	1.53
2456770.632605	-86.86	0.95	94.94	1.34
2456493.432587	43.02	1.93	-5.43	1.76
2456494.454912	75.47	1.53	-68.78	1.98
2456563.299678	43.56	0.88	-32.48	1.30
2456565.315114	30.67	0.65	-26.14	1.25
2456565.329755	18.03	0.85	-30.37	1.51
2456566.294744	-10.55	0.28	20.02	1.19
2456878.363028	-41.31	0.83	64.88	1.34
2456603.223409	12.78	1.22	6.16	2.04
2456604.220170	71.16	1.17	-57.15	1.55
2456607.240990	-30.69	1.20	14.96	3.42
2456608.215116	29.73	1.09	-37.31	2.14
2456765.628821	78.97	1.77	-58.32	1.71
2457101.644437	-9.84	0.69	10.96	2.06
2457240.450714	-19.14	0.42	37.07	1.04
2457536.483128	-27.93	0.65	52.93	1.75

Table 3.1: Bisector velocity span and RV measurements of HD 166435 are presented in chronological order. The data for analysis is taken from the SOPHIE archive.

BJD_{TDB} Days	Relative-RV m s^{-1}	σ-RV m s^{-1}	BVS m s^{-1}	σ-BVS m s^{-1}
2455433.552167	-35.48	0.12	60.51	0.24
2455762.572980	-30.67	0.20	61.49	0.40
2455782.593436	-26.15	0.24	-19.58	0.52
2455794.481968	-29.02	0.31	-9.51	0.64
2455417.606745	-27.08	0.34	-20.84	0.69
2455417.643368	-27.42	0.32	-27.11	0.63
2455418.421407	-29.27	0.54	-41.71	1.00
2455418.424347	-28.81	0.54	-39.40	1.10
2455418.492614	-31.39	0.61	-43.38	0.85
2455418.529040	-26.79	0.49	-42.56	0.90
2455418.565465	-61.18	2.85	-44.72	0.74
2455418.604113	-27.06	0.40	-45.33	0.74
2455418.640701	-26.47	0.44	-49.74	0.74
2455419.341745	-23.42	0.70	9.68	1.15
2455419.345090	-25.93	0.65	13.01	1.13
2455419.418554	-25.18	0.46	16.14	0.88
2455419.459100	-25.34	0.74	7.44	1.65
2455419.497065	-20.14	0.56	27.43	0.83
2455419.533491	-22.01	0.64	18.26	0.90
2455419.569661	-7.70	0.71	13.69	1.28
2455419.605855	-5.60	0.45	23.79	0.80
2455419.642188	-24.42	1.20	19.83	0.64
2455420.375258	-26.34	0.90	71.51	0.80
2455420.377886	-28.83	1.16	72.67	0.78
2455420.414369	-33.18	4.03	45.00	3.50
2455420.460934	-31.97	1.74	61.34	2.64
2455420.502498	-29.79	0.59	69.28	0.80
2455420.539063	-3.01	0.41	60.73	0.71
2455420.575697	-31.69	1.05	68.64	0.75
2455420.612353	-30.76	0.50	70.38	0.70
2455421.382982	-24.02	0.59	22.12	1.18
2455421.386582	-31.14	0.64	26.83	1.19
2455421.425982	-24.21	2.11	24.54	4.26
2455421.483797	-41.17	0.90	20.35	1.68
2455421.520570	-30.85	0.99	15.62	2.00
2455421.567332	-36.10	0.96	10.13	1.76
2455421.617056	-31.92	0.60	12.63	1.18
2455422.356027	-15.36	1.00	-37.70	1.91
2455422.359361	-29.69	0.72	-36.33	1.47
2455422.395566	-29.48	0.59	-39.91	1.08
2455422.439434	-22.26	0.47	-43.24	0.96
2455422.475547	-23.33	0.56	-49.15	0.81
2455422.511718	-25.64	1.62	-61.36	2.07
2455422.547900	-30.70	0.65	-46.52	0.80
2455422.584036	-28.30	0.45	-58.57	0.74
2455422.620253	-31.07	0.89	-60.08	1.02

Table 3.2: Bisector velocity span and RV measurements of 51 Pegasi are presented in chronological order. The data for analysis is taken from the SOPHIE archive.

BJD_{TDB}	Relative-RV	σ-RV	BVS	σ-BVS
Days	m s^{-1}	m s^{-1}	m s^{-1}	m s^{-1}
2458870.118345	-432.76	28.43	-159.95	19.2135
2458872.116189	56.11	6.02	-85.11	8.38893
2459203.177756	-741.10	41.45	-76.22	19.1705
2459205.149349	89.70	87.08	-192.24	24.0852
2459205.175343	290.45	108.61	-131.98	31.3535
2459233.157837	-194.04	145.30	-9.14	26.6539
2459234.098448	-488.56	27.13	-223.57	12.4891
2459235.097271	-373.45	315.49	-495.61	59.2014
2459236.103872	-1722.07	136.58	564.83	43.1842
2459236.135617	-20.61	169.20	611.71	54.8102
2459237.096434	-177.96	12.92	103.58	8.74420
2459237.121351	-147.73	29.65	-47.42	9.44257
2459571.101124	-46.23	12.95	274.62	14.2072
2459591.176051	-189.01	15.07	-76.94	19.4602
2459592.123849	150.95	13.38	-56.56	13.9774

Table 3.3: Bisector velocity span and RV measurements of TOI-1490 from PARAS data are presented in chronological order.

Chapter 4

Discovery of an Inflated hot Jupiter TOI-1789 b

4.1 Introduction

Hot Jupiters have achieved remarkable milestones in the field of exoplanetary science. The continuous progress in the space and ground-based transit and RV surveys (Mayor et al., 2003; Bouchy & Sophie Team, 2006; Baglin et al., 2006b; Borucki et al., 2010; Quirrenbach et al., 2014; Ricker et al., 2015) has not only increased the number of hot Jupiters but also enabled the precise measurements of their radii, masses, and densities. These surveys have revealed that hot Jupiters often exhibit larger radii, typically ranging from 10% to 50% greater than that of Jupiter. (Hartman et al., 2012; Espinoza et al., 2016; Raynard et al., 2018; Soto et al., 2018; Tilbrook et al., 2021). Chapter 1 discusses the proposed mechanisms behind this radius inflation, with intense radiation from their host stars being the primary cause (Laughlin et al., 2011b; Thorngren & Fortney, 2018). The evolved stars emit higher amounts of radiation because of their larger sizes in contrast to their solar analogs. Given the scarcity of systems featuring giant stars harbouring planets within 0.5 AU, it is crucial to focus on stars that might be transitioning from the main sequence to the sub-giant/giant branch. Detecting these stars during an evolutionary phase that has not yet resulted in the engulfment of their orbiting planets presents an intriguing opportunity. Currently, only a small number of close-in planets have been discovered around slightly evolved stars, such as KELT-12 b (Stevens et al., 2017), HATS-40 b (Bento et al., 2018b) and TOI-640 b (Rodriguez et al., 2021) to name a few.

This chapter presents our work related to the detection and characterization of a transiting hot Jupiter orbiting a slightly evolved star known as TYC 1962-00303-1 or TOI-1789. The photometric and high-resolution spectroscopic and imaging data were utilized to confirm the nature of this transiting candidate and derive its mass, radius, and density for characterizing the planet. All the observations, analyses, and results of the TOI-1789 system are presented here. The implications of the results are discussed at the end of the chapter.

4.2 Photometric, Imaging, and Spectroscopic Observations of TOI-1789

4.2.1 TESS Photometry

TYC 1962-00303-1 ($V = 9.7$) was initially identified as TOI-1789 on March 12, 2020. TESS observed this star between January 21 and February 18, 2020, covering a period of 27.3 days. However, a data gap of ~ 2 days occurred in the observations due to data transfer from the spacecraft. The observations of TOI-1789 were made in TESS sector 21 using CCD-4 of camera 1, employing a long cadence mode with 30-minute exposures. The data underwent analysis using both the Quick Look Pipeline (QLP: Huang et al., 2020) and the Science Processing Operations Center (SPOC: Jenkins et al., 2016) pipeline. The QLP is developed by MIT, while the SPOC pipeline is based on the one used for the Kepler mission at NASA Ames Research Center. Both analysis pipelines detected 8 transits, each exhibiting a depth of ~ 2600 parts per million (ppm). These transits occurred at regular intervals of ~ 3.21 days with the duration of ~ 2.3 hours. Prior to being released as a planetary candidate, the TESS Science team vetted the transit data. The reported transits exhibit a V-shaped light curve and show a small centroid offset on the star position. The Pre-search Data Conditioning Simple Aperture Photometry (PDCSAP) light curves (Stumpe et al., 2014; Smith

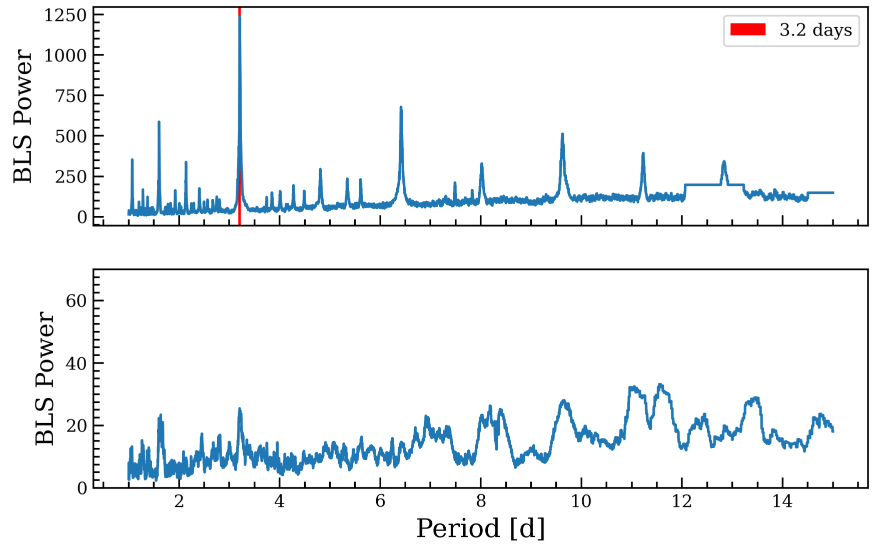

Figure 4.1: **Upper panel:** Box Least Square periodogram for TOI-1789. The peak can be seen at ~ 3.21 days signal. **Bottom panel:** Residual periodogram.

et al., 2012) extracted from the SPOC pipeline were utilized for this work. These light curves are publicly accessible through the Mikulski Archive for Space Telescopes (MAST)*. The Box Least-Square (BLS; Kovács et al., 2002) periodogram was further computed to identify transits in the PDCSAP light curves, and the transit signal with a period of 3.2076208 days and a depth of 2610$\pm$220 ppm was successfully retrieved. The corresponding BLS periodogram for TOI-1789 is presented in Figure 4.1. To explore the presence of additional transit signals, another analysis was conducted using the BLS periodogram after removing the 3.2076208-day signal from the dataset. However, no significant peaks were found, as indicated in the residual periodogram (bottom panel of Figure 4.1). Median-normalized PDCSAP light curves were used for further analysis, and additional detrending was performed on the fluxes. To accomplish this, the transits were initially masked, and the `Lightkurve` package (Lightkurve Collaboration et al., 2018) was employed to fit a high-order polynomial over the out-of-transit data. The resulting detrended light curve, which is now suitable for transit modeling, can be observed in Figure 4.2. Table 4.1 presents the basic properties of the star as reported in the existing literature.

Stellar companion of TOI-1789: The system has been reported as a widely

*https://mast.stsci.edu/portal/Mashup/Clients/Mast/Portal.html

Parameter	Description (unit)	Value	Source
α_{J2000}	Right Ascension	09:30:58.42	(1)
δ_{J2000}	Declination	26:32:23.98	(1)
π	Parallax (mas)	4.474 ± 0.0181	(1)
μ_α	PM in R.A. (mas yr^{-1})	-7.977 ± 0.019	(1)
μ_δ	PM in Dec (mas yr^{-1})	-39.401 ± 0.015	(1)
G	*Gaia* G mag	9.584 ± 0.0002	(1)
T	TESS T mag	9.182 ± 0.006	(2)
B_T	Tycho B mag	10.422 ± 0.039	(3)
V_T	Tycho V mag	9.788 ± 0.031	(3)
J	2MASS J mag	8.672 ± 0.024	(4)
H	2MASS H mag	8.410 ± 0.021	(4)
K_S	2MASS K$_S$ mag	8.345 ± 0.018	(4)
$W1$	WISE1 mag	8.297 ± 0.023	(5)
$W2$	WISE2 mag	8.348 ± 0.02	(5)
$W3$	WISE3 mag	8.311 ± 0.024	(5)
$W4$	WISE4 mag	7.996 ± 0.226	(5)
g	SDSSg mag	10.353± 0.100	(6)
r	SDSSr mag	9.590± 0.060	(6)
i	SDSSi mag	9.398± 0.020	(6)
B	APASS B-mag	10.335± 0.020	(6)
V	APASS V-mag	9.686 ±0.030	(6)

Other Identifiers:

HD 82139[7]
TYC 1962-00303-1[3]
TIC 172518755[2]
$GaiaEDR3$ 646125297938578944[1]
2MASS J09305841+2632246[4]

Note: The SIMBAD database mentions the K0 spectral type for the host star, our own spectral analysis revealed that it is actually a late F-type star, as described in Section 4.3.1.1 and Section 4.4.1.

References. (1) Gaia Collaboration et al. (2021), (2) Stassun et al. (2018), (3) Høg et al. (2000), (4) Cutri et al. (2003), (5) Cutri et al. (2021), (6) Henden et al. (2016), (7) Cannon & Pickering (1993)

Table 4.1: Basic Stellar Parameters for TOI-1789

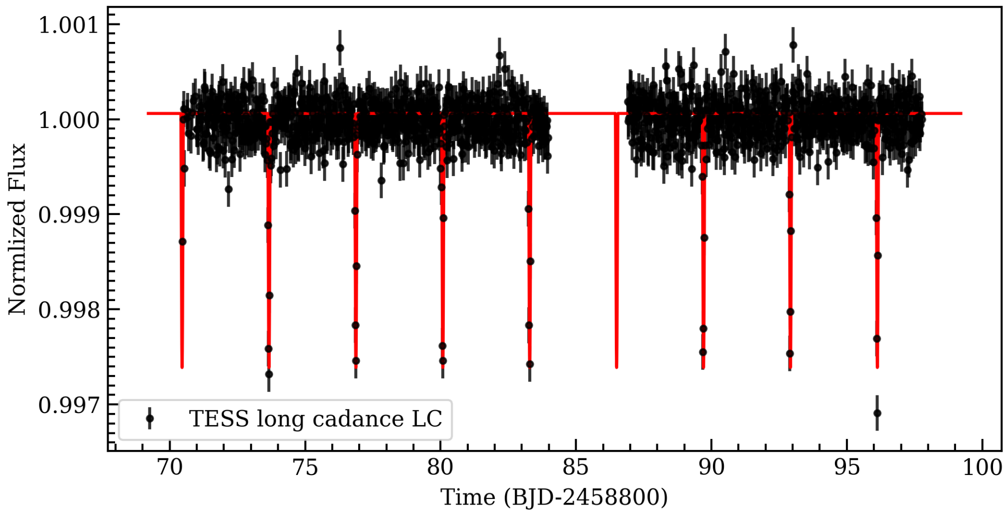

Figure 4.2: The plot shows the TESS Light Curve (LC) of TOI-1789 after normalization. The LC reveals eight clearly visible transits, occurring every ∼3.21 days, and has a depth of ∼2.6 ppt. The best-fit transit model is represented by the overlaid red line, which results from the simultaneous fitting of TESS and PRL photometry data using EXOFASTv2(Eastman et al., 2019). Refer to Section 4.3.3 for more details on fitting.

separated visual binary, and the stellar companion, TYC 1962-475-1, shares a similar spectral type and brightness with TOI-1789. The two stars have an orbital separation of 17776 AU, which corresponds to a separation of approximately 1.3′ on the sky (Andrews et al., 2017).

Gaia assessment: The Gaia Renormalised Unit Weight Error (RUWE) is a metric similar to a reduced chi-square, where values that are $\lesssim$ 1.4 indicate that the Gaia astrometric solution is consistent with the star being single, whereas RUWE values $\gtrsim$ 1.4 may indicate an astrometric excess noise, possibly caused the presence of an unseen companion (e.g., Ziegler et al., 2020). The *Gaia* RUWE number for TOI-1789 is 0.948, suggesting that a single-star model best fits the astrometric observations (Gaia Collaboration et al., 2021).

Additionally, the separation between these two sources on the sky is greater than the TESS pixel scale of 21″. The PDCSAP fluxes provided in the data have been corrected for potential contamination from neighboring pixels, as stated in the Kepler manual (Thompson et al., 2016). However, due to the long ca-

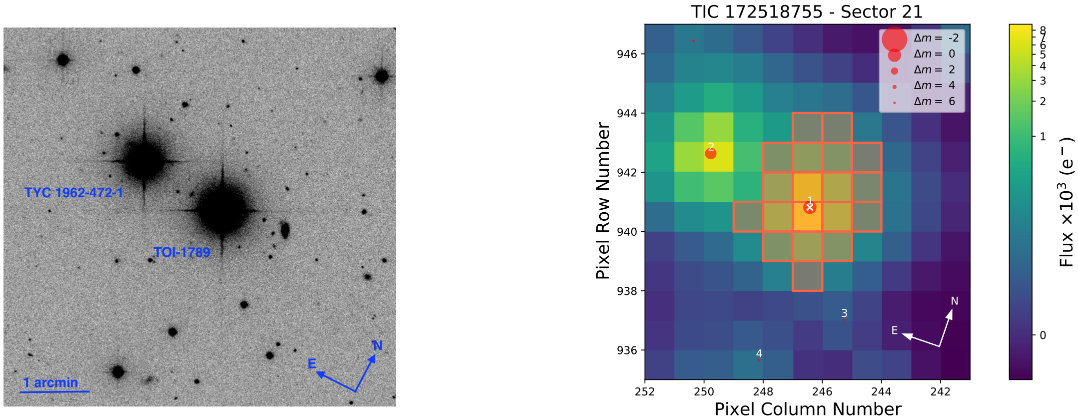

Figure 4.3: *Left panel:* TOI-1789 and its visual binary companion (TYC 1962-472-1) as observed in the SDSS (DR7) in the *sloan-i* band†. *Right panel:* The Traget Pixel File (TPF) for TOI-1789 is created with `tpfplotter` (Aller et al., 2020). The individual red dots' sizes represent the magnitude contrast (Δm) with TOI-1789 which is labeled as '1'. The red-squared region represents the aperture mask used for photometry by the SPOC pipeline.

dence data (30-minute intervals), the short transit duration ($\sim$ 2 hrs), and the V-shape of the transits, it is difficult to precisely determine the transit shape, duration, and planetary radius. The TESS data validation report also mentions a slight centroid offset in the target's position. To address these limitations and gain more precise transit parameters while verifying the nature of the transits detected by TESS, we carried out short-cadence ($\sim$ 20 sec) ground-based transit observations. The goal was to determine precise transit parameters and further investigate the characteristics of the observed transits (see Section 4.2.2).

4.2.2 Ground-based Photometry

The ground-based transit follow-up observations for TOI-1789 were acquired using the PRL's 0.43 m telescope. Additional information about the telescope can be found in section 2.7. Both the CCDs, `TRIUS PRO-814` (TRI) and `ANDOR iKon-L 936` (ADR), were utilized for the transit observations. A total of five full transits were observed from January 08, 2021, to March 10, 2021, as summarized in Table 4.2 and depicted in Figure 4.4. The initial three transits were acquired using the TRI CCD, while the remaining two transits were observed using the

Instrument	UT Date (year: 2021)	5-min Precision (ppt)	Avg. PSF (″)	Avg. EXP-time (s)
`TRIUS PRO-814`	Jan 08	0.94	4.1	25s
`TRIUS PRO-814`	Jan 21	1.04	4.4	25s
`TRIUS PRO-814`	Feb 06	1.32	3.9	20s
`ANDOR iKon-L 936`	Mar 07	0.89	6.2	18s
`ANDOR iKon-L 936`	Mar 10	1.00	4.5	8s

Table 4.2: An overview of the ground-based transit follow-up observations of TOI-1789.

ADR CCD. During the observations, the telescope was slightly defocused to extend the exposure times, resulting in a higher signal-to-noise ratio (SNR) and improved photometric precision. The observations of all the transits were taken in the Bessel-R passband. It's worth noting that the use of the ADR CCD in precision differential photometric observations has been well-established, given that the similar type of CCD detectors are employed in other transit surveys such as SPECULOOS (Sebastian et al., 2020) and SuperWASP (Pollacco et al., 2006).

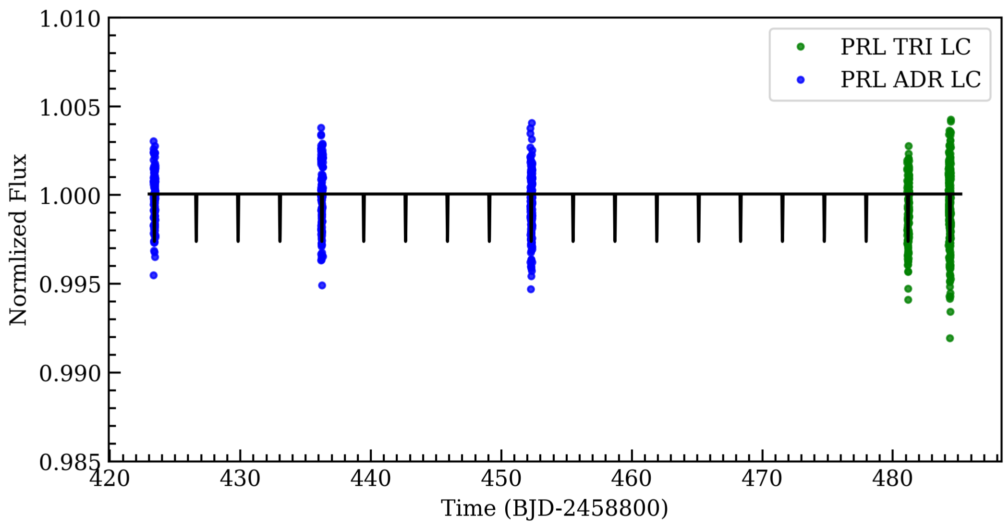

Figure 4.4: Ground-based light curves of TOI-1789 obtained from the PRL 0.43 m telescope. The first three transits, observed with TRI CCD, are depicted with blue dots, while the remaining two transits, observed with ADR CCD, are shown with green dots. The black line represents the best-fitted transit model.

For data reduction and extraction of light curves, we employed the AstroImageJ software (AIJ: Collins et al., 2017). AIJ is a powerful tool for performing ultra-precise differential photometry, light curve detrending, fitting, and plotting on time-series data, including exoplanet transits. Firstly, all the raw science frames underwent dark correction and flat-fielding. Then, multi-aperture differential photometry was employed, following the approach described in Collins et al. (2017). The aperture size used was 1.5 times the full width at half maximum (FWHM) of the star. Hence, the light curves were extracted. All of these extracted light curves were further linearly detrended by considering factors such as FWHM, airmass, and exposure time. The contribution of these factors was incorporated into the overall chi-square (χ^2) calculation for light curve fitting within the AIJ framework for each transit (as shown in equation 5 of Collins et al., 2017). Finally, normalized light curves were obtained from AIJ. In the detrended light curves, the transit events were clearly visible, as illustrated in Figure 4.4 and Figure 4.9. All five transit light curves were jointly modeled along with the observed RVs, as described in Section 4.3.3.

The residuals obtained from the best-fitted transit model exhibit a standard deviation (in 5 min bins) of 1.16 parts per thousand (ppt) or $\sim$ 1.3 mmag for the TRI dataset and a standard deviation of 0.92 ppt or $\sim$ 1 mmag for the ADR dataset. The achieved precision using the TRI CCD camera is within 1.3 σ of the precision achieved with the ADR CCD camera. This indicates that low-cost CCD cameras like the `TRIUS PRO-814` can effectively be used for precise differential photometric observations.

4.2.3 High-resolution Speckle Imaging[‡]

High-resolution imaging is a useful tool for identifying contamination originating from neighboring stars. The observations of TOI-1789 were conducted on February 3, 2021, using the ‘Alopeke speckle instrument that is mounted on the Gemini North 8 m telescope[§]. The ‘Alopeke instrument enables simultaneous

[‡]Results from high-resolution speckle imaging observations were made available to me by Steve B. Howell, who served as a co-author in Khandelwal et al. 2022.

[§]https://www.gemini.edu/sciops/instruments/alopeke-zorro/

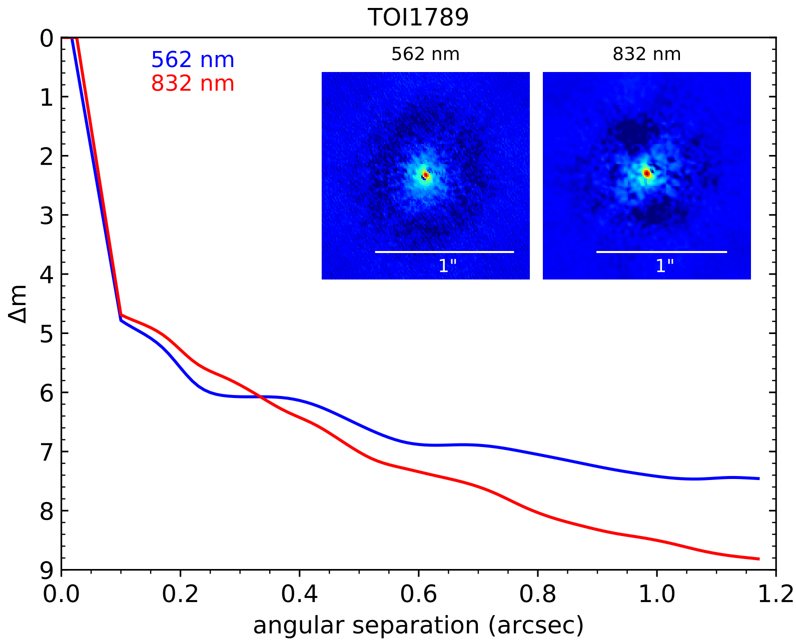

Figure 4.5: The high-resolution speckle imaging observations of TOI-1789 on UT February 3, 2021 using ‘Alopeke/Gemini instrument. The 5σ contrast curves in the 562 and 832 nm bands with their reconstructed images are plotted .

speckle imaging in two distinct wavelength bands (562 and 832 nm). The obtained data includes a reconstructed image that provides reliable contrast limits for detecting companions (e.g., Howell et al. (2016)). The observation process involved collecting five sets of 1000 exposures, each lasting 0.06 sec. Subsequently, Fourier analysis was applied to these exposures as part of the standard reduction pipeline (Howell et al., 2011). By examining the Fourier analysis, it becomes possible to identify interferometric fringes, which serve as indicators of the presence of nearby companion stars. These fringes were then utilized to determine various parameters, including the separation, position angle, and magnitude contrast (Δm) of the companions. The final results, comprising the 5σ contrast curves and reconstructed speckle images, can be observed in Figure 4.5. The contrast curves were computed by taking the average of each reconstructed image, and then radial annuli were constructed. For each pixel within these annuli, a determination was made as to whether it lay above or below the mean value. By accumulating these radial values, a polynomial was fitted at a 5σ contrast level, leading to the two contrast curves depicted in Figure 4.5. No companions with a magnitude contrast (Δm) brighter than ~ 5 were identified within a separation of 1.17″ from the TOI-1789. Given the distance to TOI-1789 (which is ∼223 pc), these angular limits correspond to spatial limits of up to 268 AU.

4.2.4 Spectroscopy

For the precise determination of the mass of the planet through RV measurements, two spectrographs, PARAS and TCES, were used. Our observations are discussed in the following sub-sections.

4.2.4.1 PARAS-PRL

The TOI-1789 was observed with the PARAS spectrograph from December 19, 2020, to March 19, 2021, and a total of 16 spectra were obtained with this. Out of these, one stellar spectrum was acquired on December 19, 2021, using ThAr HCL, while the remaining spectra were obtained using UAr HCL due to the unavailability of pure-Th HCL (Chakraborty et al., 2014; Sharma & Chakraborty, 2021). Each observation was given an exposure time of 1800 sec, resulting in an SNR per pixel ranging from 12 to 20 at 550 nm. The data was further reduced and analyzed to determine the RV measurements (See Section 2.6 for more details). An offset of 10 m s^{-1} was calculated using the RV standard star HD 55575 between the absolute RVs measured from ThAr and UAr HCL spectra. This offset was subsequently corrected in the TOI-1789 RVs for further analysis. Table 4.4 lists all the RVs obtained from PARAS, along with their respective errors.

4.2.4.2 TCES-TLS[¶]

The TOI-1789 was observed with the Tautenburg coude echelle spectrograph (TCES) attached to the 2 m Alfred Jensh telescope at the Thüringer Landessternwarte Tautenburg in Germany. The TCES is a slit spectrograph operating at a resolving power (R) of 67000 and covers a wavelength range of 470 to 740 nm. It is housed in a temperature-stabilized Coude room, ensuring a controlled

[¶]The TCES RV measurements were provided by Priyanka Chaturvedi and Eike W. Gunther, who are the co-authors in Khandelwal et al. 2022.

environment for optimal observations. For detailed information on the observations, please refer to the work by Guenther et al. (2009). The observations of TOI-1789 were taken from February 22, 2021, to April 5, 2021, and a total of 21 spectra were acquired. To ensure the wavelength calibration, an iodine cell was placed in the optical path of the spectrograph. Each of the obtained spectra had an exposure time of 1800 seconds, resulting in an average SNR per pixel of $\sim$ 43 at 564 nm. For TCES data reduction, standard IRAF routines were used, which involve bias subtraction, flat-fielding, elimination of scattered light, and spectrum extraction. First-order wavelength calibration was achieved by employing ThAr HCL spectra, which were acquired at the beginning and end of each night. An immediate wavelength solution was derived by superimposing the iodine lines. The complex forward modeling technique was used to determine the Doppler shift in the absorption lines. This approach is specific to the instrument used and relies on the point spread function (PSF) characteristics of the spectrograph (Valenti et al., 1995). RVs were calculated using Velocity and Instrument Profile EstimatoR (VIPER[‖], Zechmeister et al., 2021), a Python-based software currently being developed as an open-source solution for instrument profile and RV estimation using the Iodine cell technique. VIPER follows the standard procedure discussed in Butler et al. (1996); Endl et al. (2000).

4.3 Analysis and Results of TOI-1789 System

In order to determine the stellar and planetary properties of the TOI-1789 system, we conducted the analysis on the photometric and spectroscopic observations. The subsequent sections outline the analysis procedure and provide a concise overview of the findings obtained from our analysis.

[‖]https://github.com/mzechmeister/viper

4.3.1 The Host Star

4.3.1.1 Spectroscopic Parameters**

The spectroscopic parameters were estimated using a relatively high SNR spectrum ($\sim$ 65 per pixel) obtained from TCES-TLS without the iodine cell. At the initial stage, the empirical software `SpecMatch-Emp` code (Hirano et al., 2018) was utilized to compare the TCES-TLS spectra (with a resolution of R = 67000) with the well-characterized FGKM type stars observed with Keck/HIRES. The results yielded the following stellar parameters: an effective temperature of $T_{\rm eff} = 5804 \pm 110$ K, the iron abundance relative to hydrogen, [Fe/H] $= 0.29 \pm 0.09$ (dex), and a stellar radius of $R_* = 2.078 \pm 0.180 R_\odot$ (see Table 4.3 for details). For a more detailed analysis, the spectral analysis package `SME` (Spectroscopy Made Easy; Valenti & Piskunov, 1996; Piskunov & Valenti, 2017) version 5.22 was used. This code utilizes recalculated stellar atmospheric models and generates synthetic spectra using molecular and atomic line data from VALD (Ryabchikova et al., 2015) and the Atlas12 (Kurucz, 2013) atmosphere grids. The determination of the best-fitting stellar parameters involves an iterative process of minimizing the chi-squared statistic (χ^2) by comparing the synthetic spectra with the observed spectra. For a more thorough description of the modeling procedure, please see Fridlund et al. (2017) and Persson et al. (2018). In our modeling approach, specific spectral features that are sensitive to different photospheric parameters were selected. The effective temperature ($T_{\rm eff}$) was determined from the Hα line wings, while the surface gravity ($\log g_*$) was derived from the CaI $\lambda\lambda$6102, 6122, and 6162 triplet, as well as the λ6439 line. The iron and calcium abundances and the vsin i were fitted using narrow, unblended lines within the 6100-6500 Å wavelength range. The resulting vsin i was found to be 7.0 ± 0.5 km s^{-1}. The micro- and macro-turbulent velocities ($V_{\rm mic}$ and $V_{\rm mac}$) were kept fixed at 1 and 3 km s^{-1} (Bruntt et al., 2010; Doyle et al., 2014), respectively. The stellar parameters obtained from the SME analysis are in good agreement with the uncertainties found in the `SpecMatch-Emp` analysis (Table 4.3). The stellar parameters de-

**The basic code was run by Carina M Persson and Malcolm Fridlund, and output results were provided to me for further analysis. These two are the co-authors in Khandelwal et al. 2022.

rived from the SME serve as priors in the global modeling process. The final spectroscopic parameters, determined through the global modelling of the RV and transit data, are presented in the last row of Table 4.3, highlighted in bold font. For more details on the global modeling, please refer to Section 4.3.3. It is worth noting that our spectral analysis reveals TOI-1789 as a late F-type star, which contrasts with the spectral type (K0) as reported by SIMBAD.

Spectroscopic Parameters	$T_{\rm eff}$ (K)	[Fe/H] (dex)	$\log g_*$ (dex)
`SpecMatch-Emp`	5804 ± 110	0.29 ± 0.09	–
SME	5894 ± 142	0.38 ± 0.1	4.2 ± 0.2
Global Modelling	5984^{+55}_{-57}	$0.370^{+0.073}_{-0.089}$	$3.939^{+0.024}_{-0.046}$

Table 4.3: Spectroscopic Properties derived for TOI-1789.

4.3.1.2 Rotational Period Determination

TOI-1789 exhibits moderate rotation with a projected rotational velocity of 7.0 ± 0.5 km s^{-1}, as determined by SME spectral modeling. Using the radius of $2.168^{+0.036}_{-0.034}$ $R_\odot$ obtained from the global modeling (Section 4.3.3), a rotational period of approximately 15.7 days was calculated under the assumption that the star is observed equator-on ($i = 90°$). This analysis allows the exploration of TOI-1789's rotational behavior, and its stellar properties were further derived through the combination of results from SME spectral modeling and global modeling (see Section 4.3.3.1).

4.3.2 Periodogram Analysis

Independent from the photometry, the RV measurements obtained from both the spectrographs, PARAS and TCES, were combined in order to identify the periodic signals in the data. The instrumental offset was initially corrected by subtracting the corresponding average RV values. After that, the Generalized Lomb-Scargle periodogram (GLS; Zechmeister & Kürster, 2009) was computed on the combined RV datasets (panel 1 of Figure 4.6). For periodogram normalization and false alarm probability (FAP) calculation, the equations provided in Zechmeister & Kürster (2009) was used. A threshold FAP of 0.1% was con-

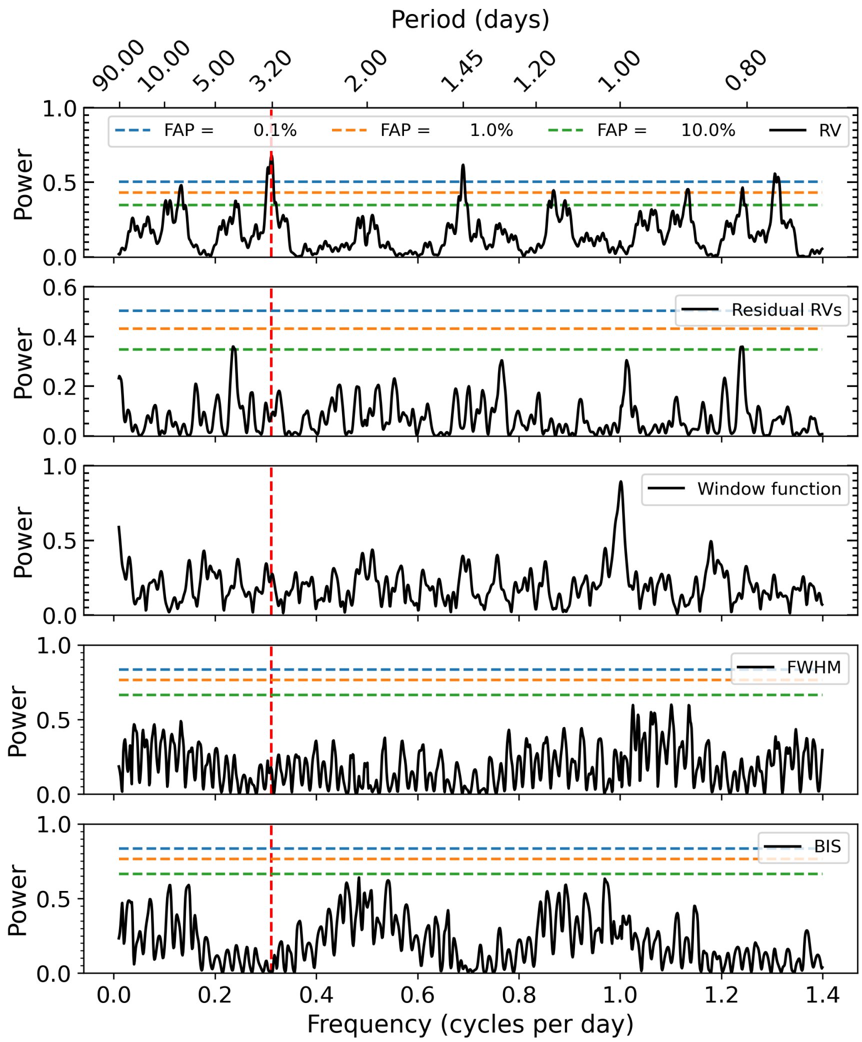

Figure 4.6: The GLS periodogram for the RVs (panel 1), residual RVs (panel 2), window function (panel 3), FWHM (panel 4), and bisector span of TOI-1789 (panel 5) is respectively shown (upper to lower). The primary peak, at ≈ 3.21 days (dashed red line), aligns with the orbital period from photometry. The FAP levels (dashed lines) of 0.1%, 1%, and 10% are shown in panel 1.

sidered to identify significant signals in the periodogram. The most prominent signal was found at approximately 3.21 days, corresponding to the orbital period derived from the transit data. This signal is marked as a vertical dashed line in Figure 4.6. To validate the periodicity at this period, we performed a bootstrap analysis with 1,000,000 randomizations within a narrow range centered around the 3.21-day period. The obtained FAP of 0.007% provides strong confirmation of a periodic signal within our RV data set. Two additional notable signals can be seen in the RV periodogram at periods of approximately 0.76 and 1.45 days. However, these signals disappear when subtracting the 3.21-day periodic signal using a best-fit sinusoidal curve (see panel 2). These signals are identified as the 1-day aliases of the orbital frequency (f_{orb}) or the 3.21-day signal. Specifically, 1/0.76 represents the 1-day alias of f_{orb}, and 1/1.45 represents the 1-day alias of -f_{orb}. No other significant periodicities above the 0.1% FAP threshold were observed in the residual periodogram. The spectral window function is shown in panel 3. Additionally, the GLS periodogram was conducted on the CCF FWHM (panel 4) and BVS (panel 5) of the PARAS data. These metrics are commonly employed as indicators of stellar activity since they quantify line asymmetries that resemble Doppler shifts (see Chapter 3). However, no statistically significant signals associated with stellar activity were found in the periodograms. Please note that the TCES data couldn't be used here due to iodine line contamination in the spectra.

4.3.3 Global Modelling with EXOFASTv2

The EXOFASTv2 (Eastman et al., 2019) is publicly accessible software that is used to constrain the parameters of the host star in the global model and determine the planetary and orbital parameters of the system. It is a collection of `IDL` routines that employ the Differential Evolution Markov Chain Monte Carlo (MCMC; Johnson et al., 2011a) technique, incorporating a Bayesian approach to explore the provided parameter space. This software is designed to fit multi-planetary systems using multiple photometry and RV datasets and also enables the estimation of stellar parameters using spectral energy distribution (SED) and isochrones analysis. The convergence of the MCMC chains is assessed using the Gelman-Rubin statistics (Gelman & Rubin, 1992; Ford, 2006).

The following subsections discuss an overview of the methodology for determining the parameters of the host star and the planet.

4.3.3.1 Modelling the Host Star

The host star parameters were determined using the SED fitting (Stassun & Torres, 2016) with the Kurucz stellar atmosphere model (Kurucz, 1979) and the MIST isochrones (Choi et al., 2016; Dotter, 2016) within the EXOFASTv2 framework. By combining the SED fitting, MIST isochrones, and transit data, we can precisely ascertain the radius, mass, age, and $\log g_*$ of the star (Torres et al., 2008). In order to constrain the stellar parameters, transit data from TESS and ground-based observations were utilized. Gaussian priors were applied to $T_{\rm eff}$ and [Fe/H], obtained from spectral analysis, and to the parallax from $GaiaEDR3$ (Gaia Collaboration et al., 2021). At the same time, uniform prior was imposed with an upper limit on V-band extinction based on Schlafly & Finkbeiner (2011) and dust maps specific to the host star's location. Figure 4.8 illustrates the plot between $\log g_*$ and $T_{\rm eff}$, as presented in Table 4.5. The solid line represents the most likely MIST evolutionary track for TOI-1789, while the dashed lines correspond to the evolutionary tracks of two different masses: 1.36 $M_\odot$ and 1.64 $M_\odot$ (within ± 0.14 of TOI-1789's mass). The broadband photometry used in this analysis includes Tycho BV (Høg et al., 2000), 2MASS JHK (Cutri et al., 2003), APASS DR9 BV, SDSSgri (Henden et al., 2016), ALL-WISE W1, W2, W3, and W4 (Cutri et al., 2021), which are listed in Table 4.1. Figure 4.7 displays the best-fitting SED model and the broadband photometry fluxes.

Figure 4.13 displays the bimodality of the probability density function (PDF) for stellar mass and age, along with their correlated parameters. This bimodal pattern, characterized by two distinct peaks, has been observed in multiple recent studies (Grieves et al., 2021a; Ikwut-Ukwa et al., 2020; Carmichael et al., 2020, 2021; Pepper et al., 2020). The presence of bimodality is primarily attributed to the degeneracy between the MIST isochrones within the region of the $T_{\rm eff}-\log g_*$ plane occupied by TOI-1789. The PDF exhibits two prominent peaks centered at a mass of 1.35 $M_\odot$ (with an associated age of 4.15 Gyr) and 1.51 $M_\odot$ (with an associated age of 2.71 Gyr), having probabilities of 30% and 70% respectively.

We finally adopted the parameters for the star, including M_*, age, and

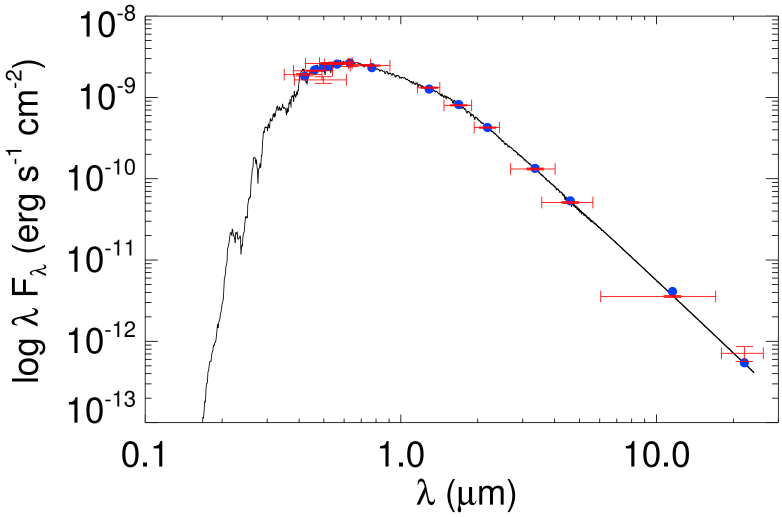

Figure 4.7: The spectral energy distribution (SED) of TOI-1789. The red markers represent the photometric measurements in each filter, with horizontal error bars denoting the bandwidth of the filters, and vertical error bars indicating measurement uncertainties. The best-fitted Kurucz stellar atmosphere model is shown in black, while blue dots represent the model fluxes over each passband.

their correlated parameters, based on the results provided by EXOFASTv2. These adopted values are centered around the most probable estimates and thus have larger uncertainties resulting from the observed bimodality. Table 4.3 presents the adopted stellar parameters, along with their corresponding 1σ uncertainties. The final adopted values for the host star's parameters are as follows: $M_* = 1.507^{+0.059}_{-0.14}\ M_\odot$, $R_* = 2.168^{+0.036}_{-0.034}\ R_\odot$, $\log g_* = 3.943^{+0.023}_{-0.043}$, at an age of $2.73^{+1.3}_{-0.51}$ Gyr. The $\log g_*$ determined here indicates a slightly lower value compared to the estimation obtained with SME in Section 4.3.1.1, with a significance level of $\sim 1.3\sigma$. The determination of $\log g_*$ through SED fitting, combined with isochrones and transit data, provides a more accurate measurement due to the strong constrain it places on the stellar density (Stevens et al., 2017). Therefore, we adopt these stellar parameters obtained from the global modeling for further calculations of the orbital and planetary parameters.

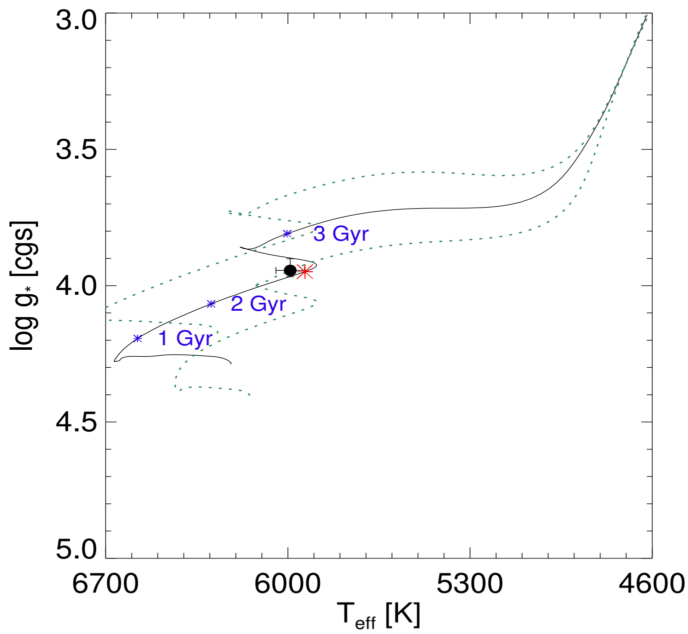

Figure 4.8: Evolutionary track for TOI-1789 from MIST (solid black line). At the model value of $T_{\rm eff}$ and $\log g_*$, the black circle is plotted with its error bars. The red asterisk indicates the model value for the Equal Evolutionary Point (EEP) or the age of TOI-1789 along the track. Additionally, there are two dashed lines representing the evolutionary tracks for masses of 1.36 $M_\odot$ and 1.64 $M_\odot$. Along the track of TOI-1789, blue asterisks denote the age values 1 Gyr, 2 Gyr, and 3 Gyr.

4.3.3.2 Orbital Parameters

Performing separate fits to the RV and transit data is valuable because it allows us to constrain parameters that are independently obtained from each dataset. Specifically, parameters such as i, R_p, b, and a are only dependent on the transit data, and K, which in turn provides insights into the mass of the planet (M_p) is depended upon RV data. However, certain parameters, including P, ω, T_c, and e, are affetced by both datasets. These parameters can effectively be constrained by simultaneously fitting the RV and transit data. For the simultaneous fitting, photometry data from two datasets, TESS and PRL (Section 4.2.2), along with RV data obtained from PARAS and TCES (Section 4.2.4), were utilized. Gaussian priors were provided from Section 4.3.3.1 and listed in Table 4.5. The initial

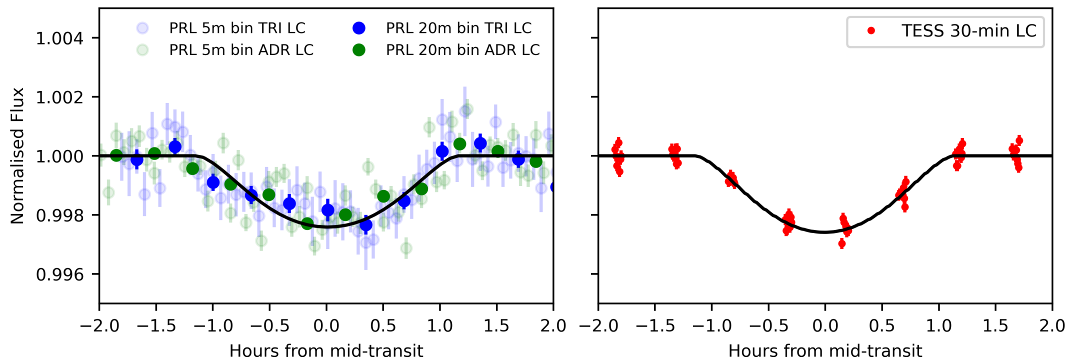

Figure 4.9: The phase folded normalized light curves of TOI-1789. Left panel:- All the transit light curves acquired from PRL's 0.43 m telescope are shown. The blue and green dots depicts the TRI and ADR datasets, respectively. The light curves are phase folded according to their orbital period and then binned to 5-min, and 20-min cadences. Right panel:- phase folded TESS light curve is presented with the red dots. The black line in both the panel is the best fitted transit model from EXOFASTv2 (For details, refer Section 4.3.3.2)

values for the P and T_c were provided based on the TESS QLP pipeline. Offsets and jitter terms for each dataset of each instrument are also incorporated in both the RV and LC fitting processes. The transit model is generated using the algorithm proposed by Mandel & Agol (2002), with the resampling over 10 steps to accommodate the TESS long cadence data (30-minute intervals) (Kipping, 2010). For the photometric data, a quadratic limb-darkening (LD) law was applied for $TESS$ and passbands. The values of u_1 and u_2 required for the LD modeling were obtained through interpolation of the limb-darkening models from Claret & Bloemen (2011) and Claret (2017).

We employed 56 chains with 50,000 steps in order to achieve convergence in the MCMC global fitting process. Initially, we fitted a circular orbit model, assuming zero eccentricity. Subsequently, we fitted an eccentric orbit model, allowing the $e\sin\omega_*$ and $e\cos\omega_*$ parameters to vary freely to assess any significant eccentricity in the orbit. The resulting eccentricity was determined to be 0.1 ± 0.075. To compare the two models and evaluate their goodness of fit, the Akaike Information Criterion (AIC, Akaike (1974)) and the Bayesian Information Criterion (BIC, Burnham & Anderson (2002)) were calculated. The ΔAIC between the models was found to be 6.0, moderately favoring the circular orbit model, while the ΔBIC was 17.0, strongly supporting the circular orbit model.

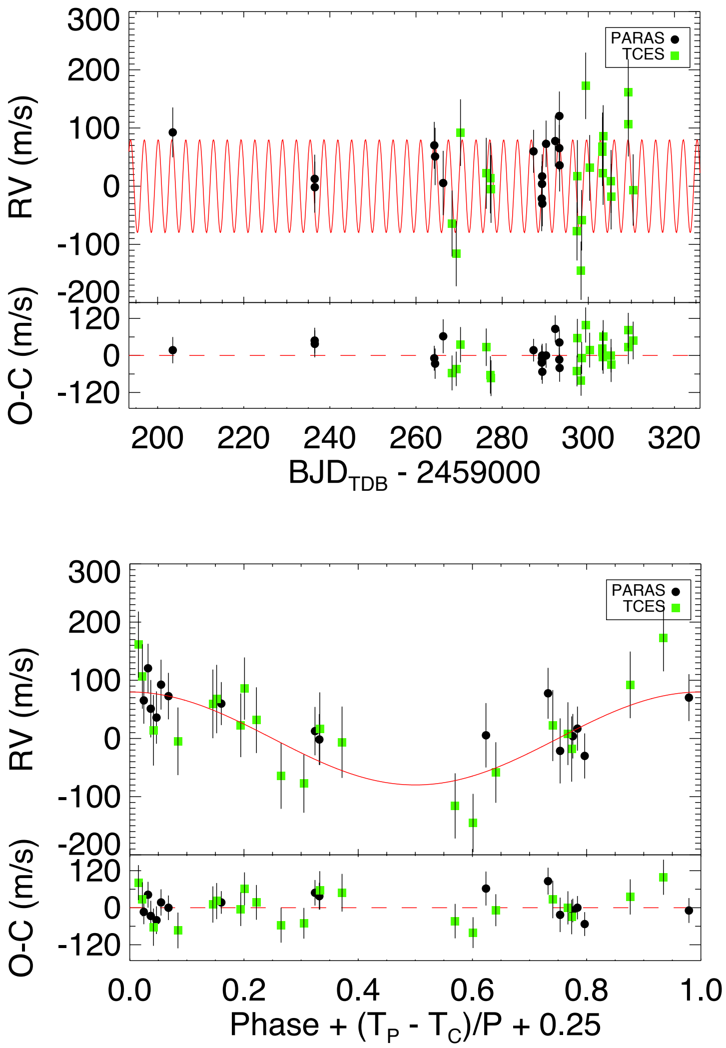

Figure 4.10: Upper panel:- The RVs of TOI-1789 obtained from PARAS (black dots) and TCES (green squares) plotted against time. Lower panel: The same RVs are shown with respect to the orbital phase (∼ 3.21d). The red line represents the best-fit RV model obtained using EXOFASTv2 (see Section4.3.3.2). The bottom panel in both figures shows the residuals, indicating the deviations between the data and the best-fit model.

Therefore, the circular orbit model was adopted for further analysis, and the orbital and planetary parameters are reported in Table 4.5. Based on our analysis, TOI-1789 b is found to have a mass of 0.70 ± 0.16 $M_{\rm J}$, and a radius of $1.44^{+0.24}_{-0.14}$ $R_{\rm J}$, resulting in a density of $0.28^{+0.14}_{-0.12}$ g cm^{-3}. The best-fit models obtained from EXOFASTv2 for the transit light curves can be seen in Figure 4.4 and 4.9, while the RV curves are illustrated in Figure 4.10. Furthermore, Figure 4.13 depicts the covariances between all the fitted parameters obtained from the global joint fit.

In the case of TOI-1789, b+R$_p$/R$_*$ $>$ 1, indicating a grazing transit configuration. In such cases, the posterior probability densities exhibit a significant degeneracy between the transit impact parameter (b) and its related parameters (such as the inclination). This degeneracy poses challenges in precisely determining the planetary radius (R$_p$/R$_*$). Despite incorporating short cadence data in addition to TESS observations and having a relatively deeper transit depth of 0.25%, the determination of the planetary radius in TOI-1789 is not well-constrained. This is evident from Figure 4.13, where a clear degeneracy between R$_p$/R$_*$ and the inclination ($\cos i$) can be observed. As a result, there is an uncertainty of 9-16% associated with the measured planetary radius.

4.4 Discussion

The host star and planet properties of TOI-1789 were precisely determined (with the precision of 9-16% and 22% in planetary radius and mass, respectively). This system is an important contribution to studying the close-in giant planets around slightly evolved stars. Our focus in the following discussion revolves around the evolutionary status of the host star and the derived properties of the planet.

4.4.1 The Evolved Star

Semi-analytical disk models show the occurrence rate of giant planets should increase with their host star's mass between 0.2 to 1.5$M_\odot$ (Ida & Lin, 2005; Kennedy & Kenyon, 2008). However, this trend is expected to weaken beyond this mass limit due to a slower growth rate, shorter lifespan of the protostellar disk, and longer migration timescale (Reffert et al., 2015b). Exploring planets around main sequence stars that are more massive than the Sun can provide valuable insights into this aspect. However, the rapid rotation of these stars broadens their spectral lines, making it difficult to precisely measure their Doppler shifts. As a result, RV surveys have traditionally focused on slow-rotating FGK-type stars. When these rapidly rotating stars transition away from the main sequence, they significantly slow down and cool, making the search for planets around them relatively easy. This characteristic has been utilized in dedicated planet searches around intermediate-mass sub-giant stars, resulting in the discovery of numerous planets (Johnson et al., 2007, 2010b, 2011b). At the Lick Observatory, a survey of giant stars showed an important finding: the occurrence rate of the planets reaches its highest point at a stellar mass of $1.9^{+0.1}_{-0.5}\,M_{\odot}$. However, many of the detected planets around evolved stars were found at large orbital distances (Hatzes et al., 2003; Robinson et al., 2007; Fischer et al., 2007; Johnson et al., 2008). This is not surprising since the interaction between the star and the planet is primarily influenced by tidal forces. When the star's rotation period exceeds the planet's orbital period, the star encounters an increase in its rotation rate, which leads to a decrease in the orbital distance. The orbit of a planet goes through synchronization and circularization when the total angular momentum exceeds a critical threshold. However, if the total angular momentum is below this threshold (or small enough), the planet's orbit continues to shrink until it eventually gets engulfed by the host star. The occurrence of this phenomenon relies entirely on the tidal dissipation time scales of the star (Mazeh, 2008, and references therein). These tidal forces play an increasingly crucial role when the host star is in an evolved state, raising the possibility of the planet being destroyed (Kunitomo et al., 2011; Schlaufman & Winn, 2013). However, estimating these tidal dissipation forces remains a challenge. The circularization timescale serves as a measurement for the tidal dissipation occurring within planets (Socrates et al., 2012; Hansen, 2010). Most hot Jupiters discovered with periods less than 3 days have circular orbits. We have calculated the circularization timescale for the orbit of TOI-1789 b, which is $\tau_{cir} = 0.08$ Gyr (for $Q_P = 10^6$, equation (3) of Adams & Laughlin (2006)). This timescale is shorter than the star's age calculated in our study (Section 4.3.3.1). In Figure 4.11, we illustrate all the transiting hot

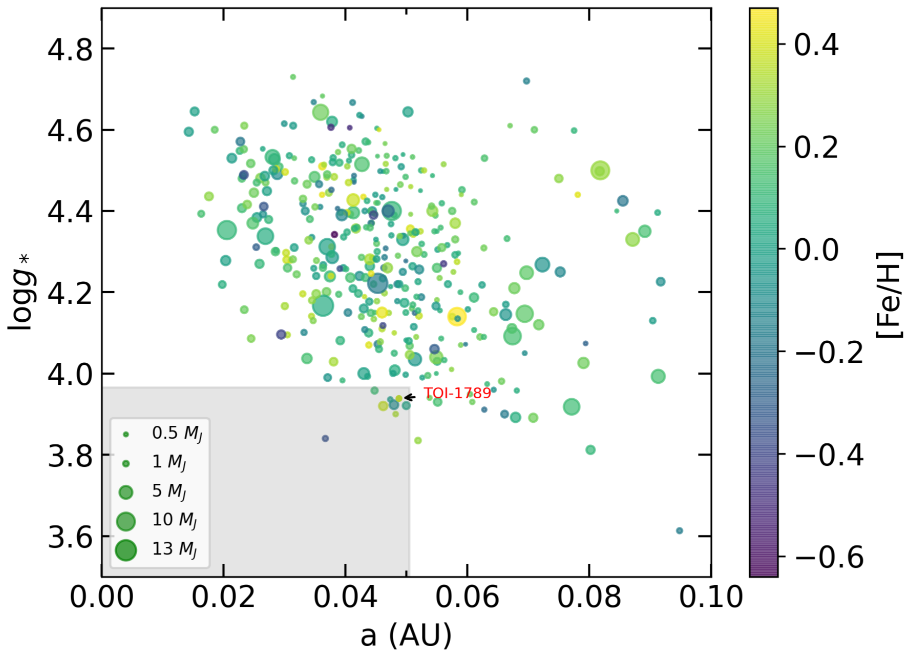

Figure 4.11: The surface gravity ($\log g_*$) of host stars with transiting hot Jupiters plotted against their orbital separation (a). The data utilized for this plot is sourced from the TEPcat database[††], considering only planets with uncertainties in masses and radii below 25%. The color-coding represents the metallicity of the host stars, ranging from low metallicity (blue) to high metallicity (yellow). Each data point's size represents the planet's mass in M_J. The shaded region ($a \leq 0.05$ AU and $\log g_* \leq 4.1$ dex) contains seven other exoplanets, with TOI-1789 marked by a black arrow and red label.

Jupiters which have uncertainties in their masses and radii less than 25% and the data taken from the Transiting ExoPlanet catalogue (TEPcat) database[††]. We apply a planet mass cutoff ranging from $0.25 M_J < M_P < 13 M_J$, along with an orbital period shorter than 10 days, in order to maintain consistency with the definition of hot Jupiters (Dawson & Johnson, 2018; Boss et al., 2005b). In the Figure 4.11, the $\log g_*$ vs the semi-major axis (a) is plotted. The $\log g_*$ serves as an indicator of the star's evolutionary status, whereas a represents the separation between the orbiting planet and its host star. The color of the stars corresponds to their respective metallicity, where super-solar metallicity is represented by yellow and sub-solar metallicities are indicated by blue. The size of the data points

[††]https://www.astro.keele.ac.uk/jkt/tepcat/ Southworth (2011) as of March 2023

represents the mass of each planet. The position of TOI-1789 is highlighted with a red text label and an arrow in the figure. One notes that close-in transiting planets are more common around the main sequence stars ($\log g_* \geq 4.1$). Furthermore, a majority of the planet-hosting stars exhibit a super-solar metallicity. This correlation between stellar metallicity and the occurrence of planets around main sequence stars was initially reported by Gonzalez (1997b); Santos et al. (2004b); Fischer & Valenti (2005b). Surveys such as the ELODIE and the Next 200 Stars (N2K) were specifically designed to use this information and have led to the discovery of several Jovian exoplanets (Bouchy et al., 2005; Fischer et al., 2005; Moutou et al., 2006). The investigation of the planet-metallicity relationship has been extended to evolved stars through a comprehensive survey conducted at the Lick Observatory (Frink et al., 2001), which revealed a strong correlation with a power-law exponent of $1.7^{+0.3}_{-0.4}$ (Reffert et al., 2015b). TOI-1789 joins the population of other metal-rich host stars with a derived metallicity of $0.373^{+0.071}_{-0.086}$ dex.

Given any stellar type, there is a detection bias favouring close-in planets. Furthermore, the Figure 4.11 reveals that in the case of evolved stars ($\log g_* < 4.1$), there are fewer planets located in close proximity to their host stars compared to main-sequence stars. This scarcity of close-in planets around giants and sub-giant stars was previously observed by Bowler et al. (2010). The surface gravity of the host star demonstrates a weak linear correlation with the separation (a) as depicted in the figure (Pearson correlation coefficient = -0.34, $p = 8.2 \times 10^{-12}$). This plot highlights that the proximity of orbiting planets depends on the evolutionary stage of the host star. The TOI-1789 b, positioned at 0.048 AU from its host star, is classified as a close-in planet and appears to lie near this boundary. It is possible that such close-in planets could be engulfed by their host stars during the sub-giant/giant phase of stellar evolution. This notion is supported by the masses of the planets observed near this boundary limit, most of which have sub-Jovian to Jovian-like masses. Tidal forces are expected to be stronger when the orbiting planet has a larger mass (Mazeh, 2008). Currently, only eight planetary systems (including this study) orbiting stars similar to or more evolved than TOI-1789 are known to be located closer to their host stars (a $\leq$ 0.05 AU). These systems include WASP-78 (Smalley et al., 2012), WASP-71 (Smith et al., 2013), HATS-26 (Espinoza et al., 2016), WASP-82 (West et al., 2016), HATS-12 (Rabus et al., 2016), HATS-40 (Bento et al., 2018a), and WASP-165 (Lendl et al., 2019). The shaded grey region in Figure 4.11 marks the boundary (a $\leq$ 0.05 AU & $\log g_* \leq 4.1$ dex). At the age of $\sim$ 2.7 Gyr, TOI-1789 is considered a slightly evolved late F-type star with a surface gravity ($\log g_*$), radius, and mass of $\sim$ 3.9 dex, $\sim 2.2\ R_\odot$, and $\sim 1.5\ M_\odot$, respectively. The circular orbit of the planet in this system provides evidence of strong tidal interaction with its host star. This makes TOI-1789 b a rare and important system for understanding the evolution of close-in planets around slightly evolved stars.

4.4.2 The Heated Planet

Understanding the radius inflation mechanisms in hot Jupiters is indeed a significant aspect of exoplanetary science (see Chapter 1). Precise determination of stellar ages plays a crucial role in this context. The detection of inflated Jupiters during the end of the main sequence phase suggests the involvement of a deep heating mechanism. However, if inflated hot Jupiters are detected in the post-main sequence phase, it indicates that the heating is concentrated at deposition pressures equal to or exceeding 10^5 bars (Komacek et al., 2020). In a study conducted by Komacek et al. (2020), it was proposed that inflated Jupiters would be more commonly found around stars with masses ranging from $1.0M_\odot < M_* < 1.5M_\odot$. This observation aligns with the characteristics of TOI-1789, as it has a stellar mass of $1.507^{+0.059}_{-0.14}\ M_\odot$ and the planet exhibits a radius of $1.44^{+0.24}_{-0.14}\ R_J$. In Figure 4.12, all the transiting hot Jupiters' radii against their equilibrium temperatures are plotted. The data is taken from the TEPcat database[††]. The size of each data point corresponds to the mass of the planet. The position of TOI-1789 b is highlighted with a red asterisk symbol. It is worth mentioning that TOI-1789 b exhibits a relatively inflated radius compared to its mass. The estimated equilibrium temperature for the planet, assuming no albedo and perfect redistribution, is 1927^{+27}_{-17} K. Several studies, including Guil-

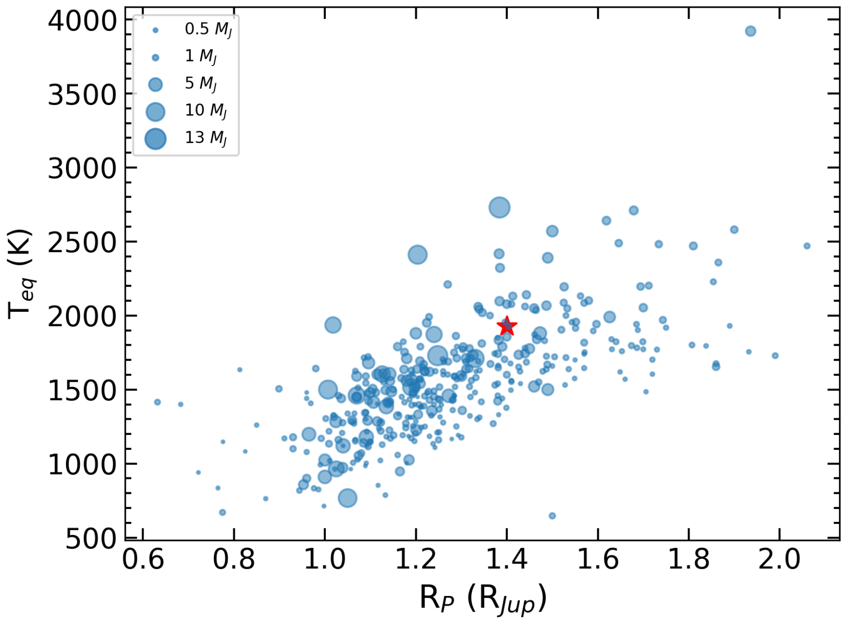

Figure 4.12: The planetary radius versus equilibrium temperature for known transiting hot Jupiters are plotted. The data is sourced from the TEPcat database[††], and only planets with uncertainties in masses and radii below 25% are included. The size of each data point corresponds to the planet's mass in M_J. The red asterisk symbol represents the position of TOI-1789 b in the plot.

lot & Showman (2002); Tremblin et al. (2017); Sainsbury-Martinez et al. (2019), suggest that the inflation observed in hot Jupiters is primarily caused by the high incident flux they receive from their host stars. TOI-1789 b, in particular, receives a total incident flux of $3.13^{+0.18}_{-0.11} \times 10^9$ erg s^{-1} cm^{-2}. This flux exceeds the threshold (2×10^8 erg s^{-1} cm^{-2}) described in Demory & Seager (2011b) by 15 times, indicating a high probability of finding inflated hot Jupiters in such conditions.

4.5 Summary of the Results for TOI-1789 System

The important results for TOI-1789 are summarized here as follows:

- The spectroscopic parameters of TOI-1789 were determined using a high SNR ($\sim$ 65 per pixel) TCES spectra. A number of methods were employed to ascertain these parameters, as outlined in section 4.3.1.1. The `SpecMatch-Emp` code provide $T_{\rm eff} = 5804 \pm 110$ K, a stellar radius, $R_* = 2.078 \pm 0.180\ R_\odot$, and [Fe/H] $= 0.29 \pm 0.09$ (dex), while the `SME` package yield $T_{\rm eff}$, [Fe/H], and $\log g_*$ of 5894$\pm$142 K, 0.38$\pm$0.1 dex, and 4.2$\pm$0.2 dex, respectively. These parameter values are within the range of uncertainty and are consistent with each other.

- High-resolution spectroscopy observations were conducted using the PARAS and TCES spectrographs. The transit light curves were obtained from TESS archival data and PRL's 0.43 m telescope data. Both the RV and transit light curves were simultaneously fitted to determine the physical parameters of the planet. The RV semi-amplitude for TOI-1789 was found to be 72^{+17}_{-16} m s^{-1}, yielding a planet mass of $M_p = 0.70 \pm 0.16\, M_{\rm J}$. A transit depth of 4.6 ppt provides estimation of the planet's radius as $1.44^{+0.24}_{-0.14}\, R_{\rm J}$. Hence, the density of the planet can be calculated as $0.28^{+0.14}_{-0.12}$ g cm^{-3}. These findings indicate that TOI-1789 b is an inflated hot Jupiter.

- Based on the modelling of the host star, TOI-1789 is found to have a mass, radius, metallicity, effective temperature, and surface gravity of $1.507^{+0.059}_{-0.14}$ $M_\odot$, $2.168^{+0.036}_{-0.034}$ $R_\odot$, $0.373^{+0.071}_{-0.086}$ dex, 5991 $\pm$ 55 K, and $3.943^{+0.023}_{-0.043}$ dex, respectively. These characteristics suggest that it is a metal-rich, slightly evolved, and late F-type star.

- Our results, as presented in section 4.4.2, indicate that TOI-1789 b might have already undergone circularization. This observation aligns with the calculated circularization timescale of 0.08 Gyr, which is shorter than the estimated age of the TOI-1789 planetary system (from this work).

- As of now[¶], only eight transiting hot Jupiters have been discovered, including TOI-1789 b. These exoplanets are hosted by stars that are either similar or more evolved than TOI-1789, and they orbit very close to their host stars (a $\leq$ 0.05 AU).

4.6 Appendix

Table 4.5: The priors, median values, and 68% confidence intervals for various physical parameters related to TOI-1789 as obtained from EXOFASTv2. Gaussian priors are denoted by $\mathcal{N}$, and Uniform priors are denoted by $\mathcal{U}$.

Parameter	Units	Adopted Priors	Values
Stellar Parameters:			
M_*	Mass (M)	–	$1.507^{+0.059}_{-0.14}$
R_*	Radius (R)	–	$2.168^{+0.036}_{-0.034}$
L_*	Luminosity (L)	–	$5.45^{+0.15}_{-0.14}$
ρ_*	Density (cgs)	–	$0.208^{+0.014}_{-0.020}$
$\log g$	Surface gravity (cgs)	–	$3.943^{+0.023}_{-0.043}$
$T_{\rm eff}$	Effective Temperature (K)	$\mathcal{N}$(5894, 142)	5991 ± 55
[Fe/H]	Metallicity (dex)	$\mathcal{N}$(0.38, 0.1)	$0.373^{+0.071}_{-0.086}$
Age	Age (Gyr)	–	$2.73^{+1.3}_{-0.51}$
EEP	Equal Evolutionary Point	–	404^{+45}_{-14}
A_V	V-band extinction (mag)	$\mathcal{U}$(0, 0.067)	$0.030^{+0.025}_{-0.021}$
σ_{SED}	SED photometry error scaling	–	$2.78^{+0.74}_{-0.52}$
$v \sin I$	Projected Rotational Velocity (km/s)	–	7.0 ± 0.5
ϖ	Parallax (mas)	$\mathcal{N}$(4.4743, 0.0181)	4.474 ± 0.018
d	Distance (pc)	–	$223.53^{+0.91}_{-0.90}$
Planetary Parameters:			b
P	Period (days)	–	3.208664 ± 0.000015
R_P	Radius ($R_{\rm J}$)	–	$1.44^{+0.24}_{-0.14}$
T_C	Time of conjunction ()	–	2458873.6537 ± 0.0006
a	Semi-major axis (AU)	–	$0.04882^{+0.00063}_{-0.0016}$
i	Inclination (Degrees)	–	$78.41^{+0.36}_{-0.58}$
T_{eq}	Equilibrium temperature (K)	–	1927^{+27}_{-17}
M_P	Mass ($M_{\rm J}$)	–	0.70 ± 0.16
K	RV semi-amplitude (m/s)	–	72^{+17}_{-16}
$logK$	Log of RV semi-amplitude	–	$1.861^{+0.090}_{-0.11}$
R_P/R_*	Radius of planet in stellar radii	–	$0.0680^{+0.011}_{-0.0061}$
a/R_*	Semi-major axis in stellar radii	–	$4.83^{+0.11}_{-0.16}$
δ	Transit depth (fraction)	–	$0.00463^{+0.0016}_{-0.00080}$
$Depth$	Flux decrement at mid transit	–	$0.00347^{+0.00020}_{-0.00018}$
T_{14}	Total transit duration (days)	–	0.0959 ± 0.0018
b	Transit Impact parameter	–	$0.972^{+0.017}_{-0.011}$
ρ_P	Density (cgs)	–	$0.28^{+0.14}_{-0.12}$
$logg_P$	Surface gravity	–	$2.91^{+0.14}_{-0.18}$
$\langle F \rangle$	Incident Flux (10^9 erg s^{-1} cm^{-2})	–	$3.13^{+0.18}_{-0.11}$
$M_P \sin i$	Minimum mass ($M_{\rm J}$)	–	$0.68^{+0.16}_{-0.15}$
M_P/M_*	Mass ratio	–	0.00045 ± 0.00010
Wavelength Parameters:		R	TESS
u_1	linear limb-darkening coeff	0.356 ± 0.035	$0.263^{+0.046}_{-0.047}$
u_2	quadratic limb-darkening coeff	$0.309^{+0.035}_{-0.034}$	0.284 ± 0.047
Telescope Parameters:		PARAS	TCES
$\gamma_{\rm rel}$	Relative RV Offset (m/s)	-93 ± 12	122^{+14}_{-13}
σ_J	RV Jitter (m/s)	26^{+14}_{-12}	51^{+14}_{-11}
σ_J^2	RV Jitter Variance	730^{+960}_{-510}	2700^{+1700}_{-1000}

Transit Parameters:		PRL ADR (R)	PRL TRI (R)	TESS (TESS)
σ^2	Added Variance	$0.00000252^{+0.00000025}_{-0.00000023}$	$0.00000015^{+0.00000018}_{-0.00000016}$	$0.0000000064^{+0.0000000018}_{-0.0000000017}$
F_0	Baseline flux	1.00006 ± 0.00010	$1.000509^{+0.000100}_{-0.000099}$	0.9999953 ± 0.0000061

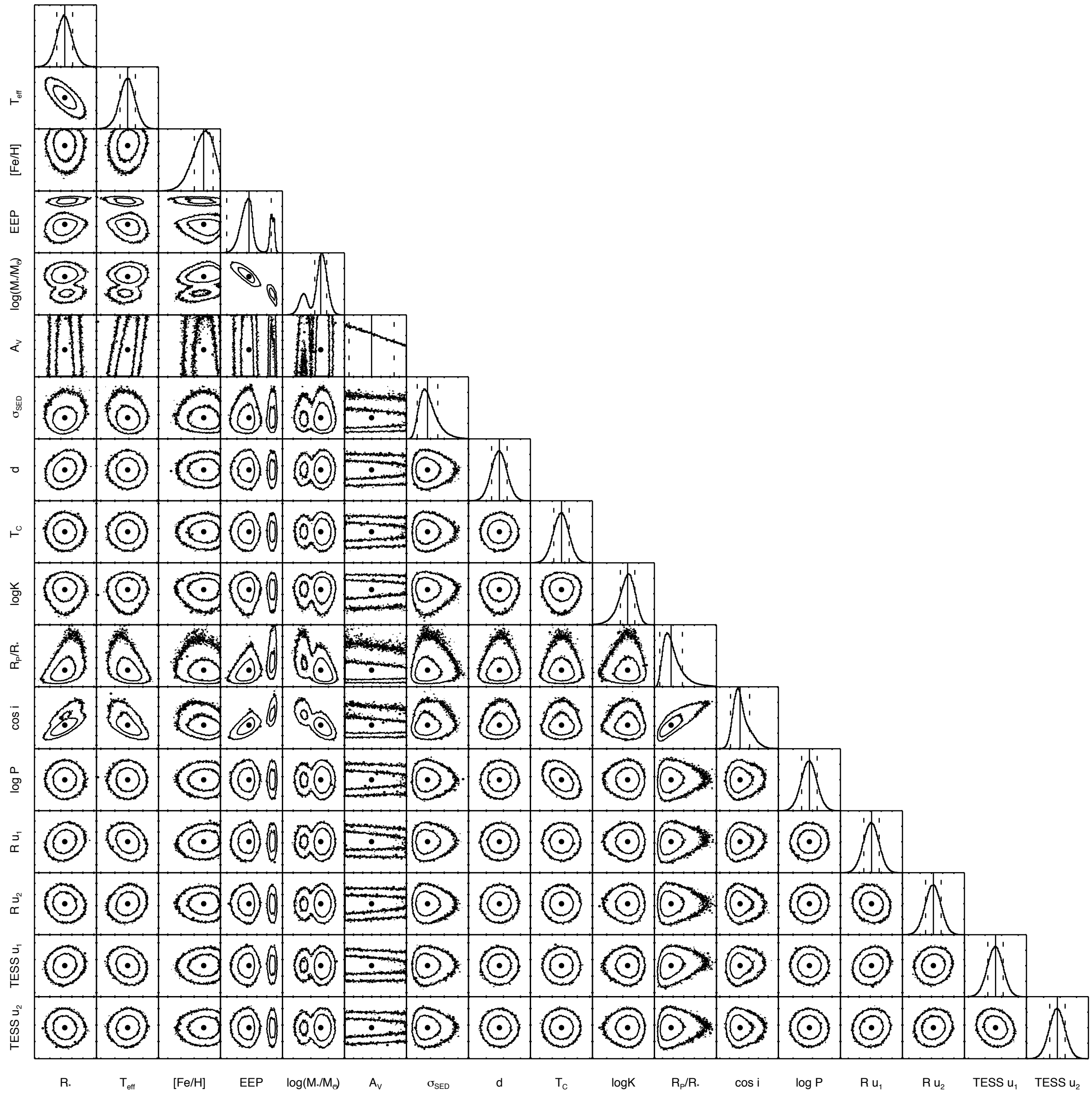

Figure 4.13: The corner plot showing the covariances for all the fitted parameters for the TOI-1789 global-fit from EXOFASTv2

BJD_{TDB} Days	Relative-RV m s^{-1}	σ-RV m s^{-1}	BVS m s^{-1}	σ-BVS m s^{-1}	EXP-TIME sec	Instrument
2459203.519645	-11.91	30.00	197.79	168.29	1800	PARAS*
2459236.471110	-91.76	28.13	267.54	64.79	1800	PARAS†
2459236.495532	-106.14	31.24	307.58	58.14	1800	PARAS†
2459264.241224	-34.16	26.40	972.78	93.32	1800	PARAS†
2459264.426243	-53.28	38.74	-83.81	79.54	1800	PARAS†
2459266.309799	-98.94	46.13	1751.67	220.13	1800	PARAS†
2459287.283471	-44.48	20.80	-551.95	30.95	1800	PARAS†
2459289.186833	-125.73	46.89	-982.45	153.12	1800	PARAS†
2459289.258414	-100.47	23.03	-100.73	87.37	1800	PARAS†
2459289.284072	-87.48	22.52	0.70	36.28	1800	PARAS†
2459289.324973	-134.37	23.88	-415.21	28.96	1800	PARAS†
2459290.195198	-31.61	25.76	175.88	36.30	1800	PARAS†
2459292.327774	-26.77	31.32	86.37	59.11	1800	PARAS†
2459293.265260	-38.99	25.86	-52.63	26.21	1800	PARAS†
2459293.288928	16.25	28.94	-80.99	101.90	1800	PARAS†
2459293.336772	-68.44	33.08	-79.96	90.14	1800	PARAS†
2459268.367086	55.72	30.32	-	-	1800	TCES
2459269.344931	4.01	28.88	-	-	1800	TCES
2459270.328739	211.94	31.26	-	-	1800	TCES
2459276.311054	142.06	37.66	-	-	1800	TCES
2459277.276355	133.96	37.06	-	-	1800	TCES
2459277.413716	115.03	32.70	-	-	1800	TCES
2459297.373577	42.26	14.10	-	-	1800	TCES
2459298.323521	-25.34	14.19	-	-	1800	TCES
2459297.462606	136.68	39.96	-	-	1800	TCES
2459298.451947	61.38	20.11	-	-	1800	TCES
2459299.393539	292.36	31.03	-	-	1800	TCES
2459300.315441	151.34	29.86	-	-	1800	TCES
2459303.279352	179.31	34.34	-	-	1800	TCES
2459303.300500	187.65	33.82	-	-	1800	TCES
2459303.436010	142.56	26.32	-	-	1800	TCES
2459303.457166	205.70	23.46	-	-	1800	TCES
2459305.274017	128.12	24.60	-	-	1800	TCES
2459305.295176	101.73	29.09	-	-	1800	TCES
2459309.278728	281.19	30.41	-	-	1800	TCES
2459309.300456	226.44	27.72	-	-	1800	TCES
2459310.422304	113.38	38.13	-	-	1800	TCES

* Spectra acquired simultaneously with ThAr HCL
† Spectra acquired simultaneously with UAr HCL

Table 4.4: RV measurements for TOI-1789, including BJD_{TDB}, relative RVs, RV errors, BVS, BVS errors, exposure time, and observation instruments.

Chapter 5

Discovery of a Massive Giant Planet TOI-4603 b

5.1 Introduction

The classification of massive giant planets (4 to $13M_J$) has always been a subject of debate, questioning whether they should be categorized as planets or brown dwarfs (BDs; Chabrier et al., 2014; Spiegel et al., 2011; Schlaufman, 2018). A few indirect ways have been proposed to differentiate between these massive giant planets and low-mass BDs. One such method relies on the deuterium burning mass limit, which suggests that an object can be considered a planet if its mass is not sufficient to sustain deuterium fusion at any stage of its lifetime. It was determined that the upper mass limit for this fusion is $\approx 13M_J$ for objects with solar metallicity (Boss et al., 2005a), regardless of how they formed. However, objects with masses less than $13M_J$ exhibit significant similarities in their properties with those having a mass of $13M_J$, irrespective of the terminology used to describe them. As a result, this definition based on a specific mass limit to distinguish between planets and BDs has led to disagreements (Chabrier et al., 2014), and various suggestions have been made to redefine the classification criteria. Spiegel et al. (2011) proposed that deuterium burning depends on the object's helium and other metal content, resulting in a deuterium burning mass limit ranging from 11 to $16M_J$. Other studies have recommended raising the upper mass limit to $\sim 25 M_J$ based on the "driest" region of the brown dwarf desert (Pont et al., 2005; Udry, 2010; Anderson et al., 2011). Another study by Hatzes & Rauer (2015) suggested a new classification, referring to objects in the 0.3–$60 M_J$ range as giant gaseous planets because they follow a distinct pattern in the mass-density diagram of all the known planets, sub-stellar objects and stars (see Figure 1 of Hatzes & Rauer 2015). The authors did not find any significant changes in this figure for objects within the 0.3–$60 M_J$ range and suggested that irrespective of how they formed, these objects should all be regarded as part of the same category, namely planets. However, the IAU recently proposed a working definition for exoplanets (Lecavelier des Etangs & Lissauer, 2022) that includes a mass ratio of the planet to the central object should be below the L_4/L_5 instability ($M/M_{central} < 2/(25+\sqrt{621}) \approx 1/25$) in addition to the $13 M_J$ mass limit.

Some researchers prefer using formation mechanisms as the basis to differentiate massive giant planets from BDs. The literature highlights two dominant formation mechanisms: core accretion and disk instability (as discussed in Section 1.4.1). However, the dominant planet formation mechanism depends on the disk mass and host star metallicity conditions (i.e., their initial environmental conditions; Adibekyan, 2019). As a result, it is currently unclear how to accurately trace the formation history of a planet, which leads to this classification approach being inadequate and problematic. Therefore, a detailed characterization of more objects in the transition region of massive giant planets and low-mass BDs is needed which will significantly enhance our understanding of the processes involved in planet formation. Moreover, the formation of close-in massive giants or giant planets is a subject of frequent debate. It is unclear whether they formed at their current short orbits (in-situ formation) or migrated from farther out orbits via gas-disk or HET migration (Batygin & Stevenson, 2010; Baruteau et al., 2014; Dawson & Johnson, 2018). See section 1.4.1 for a detailed overview. The prevailing scenario is likely a combination of these mechanisms contributing to the population of close-in giant planets.

This chapter presents our work on detecting and characterizing a close-in massive giant planet, TOI-4603 b. This planet falls within an overlapping mass region of BDs and massive giant planets. All the observations and analyses conducted for TOI-4603 are covered in this chapter. Finally, the results are discussed and summarized.

5.2 Photometric, Imaging, and Spectroscopic Observations of TOI-4603

5.2.1 TESS Observations

The star HD 245134 was initially identified as TOI-4603 on November 02, 2021. TOI-4603 was observed by the TESS in three sectors: 43, 44, and 45, with the 2-minute cadence mode almost continuously from September 16, 2021, to December 02, 2021, covering a time span of ~ 74 days. There was a gap of about 5.5 days in between, during which the data was transmitted from the spacecraft to the ground. The light curves were generated and analyzed for transit signals by the SPOC pipeline (consisting of SAP and PDCSAP fluxes) and are publicly accessible through the MAST. A total of 10 transits were detected by the SPOC

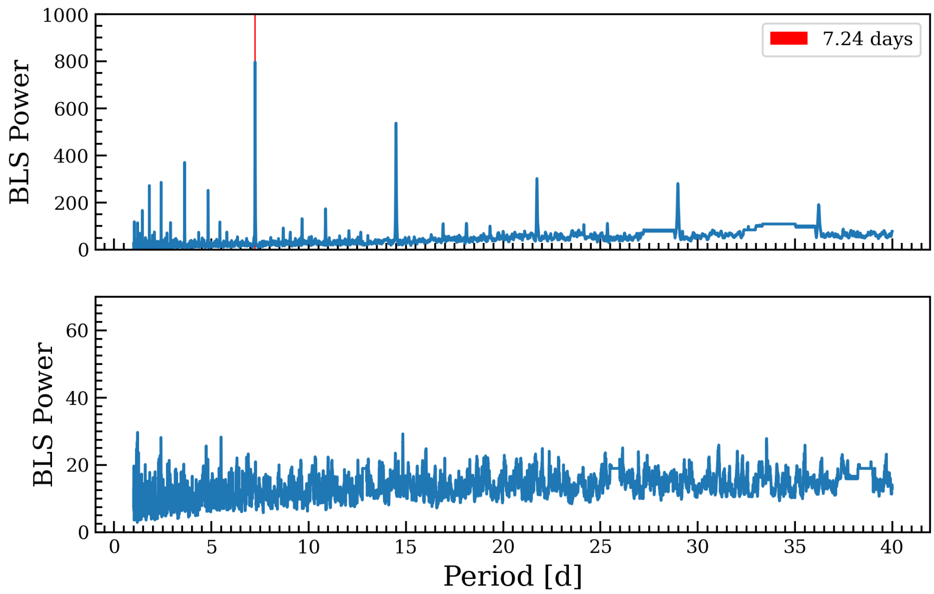

Figure 5.1: **Upper panel:** Box Least Square periodogram for TOI-4603. The peak can be seen at 7.24 days signal. **Bottom panel:** Residual periodogram.

pipeline, which have a depth, duration, and orbital period of $\sim$1020 ppm, $\sim$2.04

hours, and ∼7.24 days, respectively. Applying the BLS periodogram (Kovács et al., 2002) to the PDCSAP fluxes, the transit signals in the TESS lightcurves were successfully retrieved. The BLS periodogram is shown in Figure 5.1. The retrieved period of 7.244524 days is in quite good agreement with the value from the SPOC pipeline quoted above. Removing the transit signal at 7.244524 days and re-running the periodogram did not show the presence of any other significant peak in the data. This residual periodogram is shown in the bottom panel of Figure 5.1.

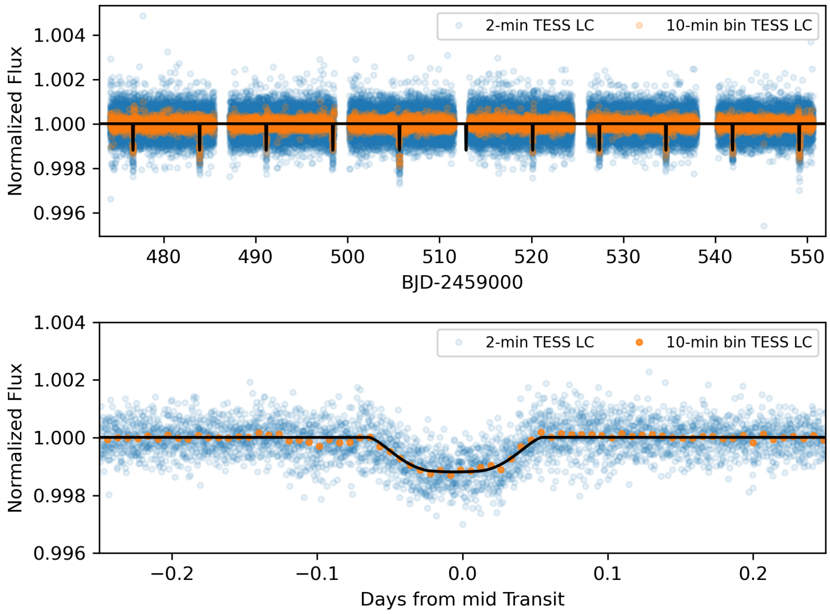

Figure 5.2: Normalized PDCSAP light curve (upper panel) and folded light curve (lower panel) for TOI-4603. The blue and orange dots in both panels represent the 2-minute and 10-minute binned data points, respectively. The black line corresponds to the best-fit transit model using EXOFASTv2 (see Section 5.3.3).

For further analysis, the PDCSAP fluxes were median-normalized and were additionally detrended using the `lightkurve` package (Lightkurve Collaboration et al., 2018), which fits a high-order polynomial over out-of-transit data. Figure 5.2 shows the normalized TESS light curve for TOI-4603. For all the observing sectors, the `tpfplotter` (Aller et al., 2020) was used to generate the TPFs of TOI-4603. These are plotted in Figure 5.3, where the orange squared region represents the aperture masks used to extract the photometry by the

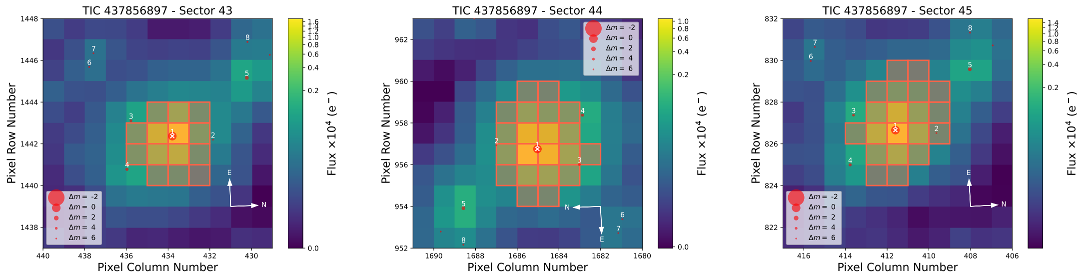

Figure 5.3: Target pixel file for TOI-4603 in sectors 43, 44, and 45 generated with `tpfplotter` (Aller et al., 2020). The squared region represents the aperture mask used in the photometry. Additionally, the size of red dots indicates the magnitude contrast (Δm) from TOI-4603. The location of TOI-4603 is labeled with '1'.

SPOC pipeline. The magnitude contrast (Δm) with TOI-4603 and the position of nearby stars from the Gaia DR2 catalogue are marked with red circles. In the aperture mask used for photometry in sector 43, no nearby stars within six magnitudes of TOI-4603 were found. However, in sector 44, two stars (labeled as '2' and '3' in Figure 5.3) were identified, and in sector 45, one star (marked as '2' in Figure 5.3) was observed within the aperture mask. The labeled '2' star is located at an angular distance of 44.64″with a 5.86 magnitude contrast, while the labeled '3' star is at an angular distance of 41.03″with a 4.01 magnitude contrast to TOI-4603. The PDCSAP light curves were already corrected for the dilution caused by nearby stars to prevent underestimating the transiting object radius. Radial velocity variations observed in spectroscopic observations match the orbital period from TESS, indicating that these nearby stars are not the cause of transits on TOI-4603.

5.2.2 High-resolution imaging*

TOI-4603 was observed with near-infrared adaptive optics (AO) imaging at Palomar Observatories in order to find the possible contamination of bound or unbound nearby companions on the calculated planetary radii (Ciardi et al., 2015). The observations were made on November 21, 2021, using the Palomar High Angular Resolution Observer (PHARO) instrument (Hayward et al.,

*The results of high-resolution imaging observations were made available by David R. Ciardi and Andrew Boyle, who served as co-author in Khandelwal et al., 2023.

2001) in conjunction with the natural guide star AO system P3K (Dekany et al., 2013). A standard five-point quincunx dither pattern with 5″ steps in the narrow band Brγ filter with a central wavelength of $\lambda_o = 2.1686$ and a bandwidth of $\Delta\lambda = 0.0326$ μm was used for the observations. Three separate observations were acquired for each dither position, with positional offsets of 0.5″ between them, resulting in a total of 15 frames. The integration time for each frame was set to 5.665 seconds, leading to a cumulative on-source observation time of 85 seconds. PHARO has a total field of view of $\sim$ 25″ with a pixel scale of 0.025″ per pixel. A custom set of IDL tools was employed to process and analyze the AO data. The science frames underwent flat-fielding and sky subtraction before combining them into a single image. This combination procedure utilized an intra-pixel interpolation technique that conserves flux, accurately aligns the individual dithered frames by appropriate fractional pixels, and then median-coadds these frames.

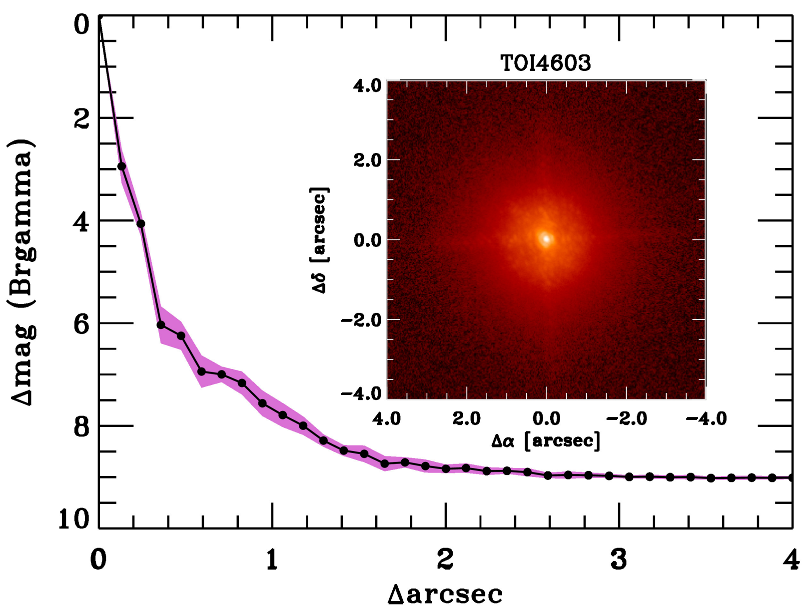

Figure 5.4: Palomar near-infrared AO imaging and sensitivity curves for TOI-4603 observed in the Brγ filter. The inset displays an image focusing on the central portion of the data, with the star precisely centered.

The final resolutions of these combined dithered images were estimated to be the FWHM of the PSFs, resulting in a value of 0.117″. To assess the sensitivities of the final combined AO image, simulated sources were injected azimuthally around the primary target every 20°, at separations equivalent to integer multiples of the central source's FWHM (Furlan et al., 2017). Each injected source's brightness was adjusted until it was detected with a significance of 5σ using standard aperture photometry. The contrast limits at each injection location were determined based on the resulting brightness of the injected sources relative to TOI-4603. At each separation, the final 5σ limit was determined by taking the average of all the determined limits. To account for uncertainty, the limit was set using the RMS dispersion of the azimuthal slices at the corresponding radial distance. Figure 5.4 displays the final sensitivity curve for TOI-4603, indicating that no additional stellar companions were detected.

Gaia assessment: In addition to high-resolution imaging, Gaia was utilized to identify any wide stellar companions that might be bound members of the system. Generally, these stars are already present in the TESS Input Catalog (TIC), and their flux dilution to the transit has been considered in the transit fits and associated derived parameters. Based upon similar parallaxes and proper motions (Mugrauer & Michel, 2020, 2021), no additional widely separated companions are identified by Gaia.

Additionally, the Gaia DR3 astrometry provides additional information on the possibility of inner companions that may have gone undetected by either Gaia or high-resolution imaging. The RUWE value from *Gaia* EDR3 for TOI-4603 is 0.998, indicating that the astrometric fits are consistent with those expected from a single-star model.

5.2.3 Spectroscopy

5.2.3.1 Radial Velocities with PARAS

The RV observations for TOI-4603 were acquired using the PARAS spectrograph from January 11, 2022, to November 02, 2022. A total of 27 spectra were obtained employing the simultaneous wavelength calibration mode with UAr HCL (Chakraborty et al., 2014; Sharma & Chakraborty, 2021). The exposure time for each spectra was set as 1800 seconds resulting in an SNR per pixel of

$\sim$ 9 to 18 at the 550 nm blaze wavelength. For detailed information about the observations and data analysis, please see Chapter 2. The uncertainties in the RVs were determined as per the procedures outlined in Section 2.6.4. The RVs and corresponding errors are listed in Table 5.1

5.2.3.2 Radial velocities with TRES[†]

A total of 13 spectra were obtained from November 03, 2021, to September 16, 2022, using the Tillinghast Reflector Echelle Spectrograph (TRES; Fűrész, 2008) for determining the RVs of TOI-4603. The TRES is a fiber-fed echelle spectrograph that is attached to the 1.5m Tillinghast Reflector telescope at Mount Hopkins, Arizona, USA. It has a resolving power of R=44000 and operates in the 390-910 nm wavelength range. Three sets of spectra were acquired, and ThAr HCL spectra surrounded each set. Combining the medians of these observed spectra effectively eliminated the cosmic rays. Each individual observation had an average exposure time of 290 seconds, resulting in an average SNR of 54.2 per resolution element. For optimal extraction of spectra, the procedure described in Buchhave et al. (2010) was used. The multi-order relative RVs were determined by cross-correlating the highest SNR spectrum order by order against all other spectra. For the RVs obtained from the TRES spectra, along with their corresponding errors, please refer to Table 5.1.

5.3 Data Analysis of TOI-4603

5.3.1 Spectroscopic Parameters of TOI-4603

The stellar parameter classification tool (SPC) (Buchhave et al., 2010; Buchhave et al., 2012; Buchhave et al., 2014) was used to determine the stellar parameters from TRES spectra. This tool employs the CCF technique between the observed spectrum and a grid of synthetic spectra created from Kurucz atmospheric models (Kurucz, 1992). Out of the 13 spectra, 12 passed the quality flag based on the SNR criteria. Using these selected spectra, the following stellar parameters

[†]RV measurements and spectroscopic analysis of TOI-4603 from TRES were provided by David W. Latham and Allyson Bieryla, who are the co-authors in Khandelwal et al., 2023.

were derived: effective temperature ($T_{\rm eff}$) of 6243 ± 50 K, metallicity ([m/H]) of 0.22 ± 0.08 dex, surface gravity ($\log g_*$) of 3.94 ± 0.10 cgs, and projected rotational velocity ($\rm vsin\,\it i$) of 25.70 ± 0.50 km s^{-1}.

Additionally, the stellar parameters were also derived with the high-SNR spectra (70 per resolution element at 550 nm) acquired from the TCES instrument. Each spectrum was observed with an exposure time of 1200 seconds. More information regarding the observations can be found in Guenther et al. (2009). To determine the stellar parameters from these TCES spectra, we employed the Zonal Atmospheric Stellar Parameters Estimator (`zaspe`) package (Brahm et al., 2017). `zaspe` determines precise stellar atmospheric parameters from high-resolution spectra by comparing observed data with synthetic spectra in sensitive zones. It computes realistic uncertainties by considering systematic mismatches between the observed and best-fitted synthetic spectra. The following stellar parameters were estimated: $T_{\rm eff} = 6273 \pm 101$ K, $[\rm Fe/H] = 0.34 \pm 0.04$ dex, $\log g_* = 3.73 \pm 0.26$ cgs, and $\rm vsin\,\it i = 23.18 \pm 0.37$ km s^{-1}. Notably, the stellar parameters obtained from the TRES and TCES spectra fall within the error bars, indicating good consistency between the two data sets.

Our analysis indicates that TOI-4603 is a metal-rich, F-type sub-giant star. In order to determine its rotation period, the GLS periodogram was computed over the out-of-transit TESS PDCSAP fluxes. The estimated rotation period is 5.62 ± 0.02 days, which closely matches with the rotation period (assuming i=90) derived using stellar radii of $2.738^{+0.048}_{-0.050}$ $R_\odot$ (Section 5.3.3) and $\rm vsin\,\it i$ of 23.18 ± 0.37 km s^{-1} (Section 5.3.1). At $\sim$2.28 days, an additional less significant peak was also observed in the periodogram. This secondary peak might be quasi-periodic and could be related or unrelated to half of the rotational period signals. While Pre-whitening the 5.62-day signal, the 2.28-day signal did not eliminated, possibly indicating that it originated from another active region on the stellar disk. Both the periodogram can be seen in Figure 5.5. However, in-depth analysis of the 2.28-day signal falls beyond the scope of this work.

The star was also studied for solar-like oscillations. Firstly, the expected frequency of the maximum oscillation amplitude (v_{max}) based on the previously derived values of $T_{\rm eff}$ and $\log g_*$ was calculated, using the seismic scaling relation

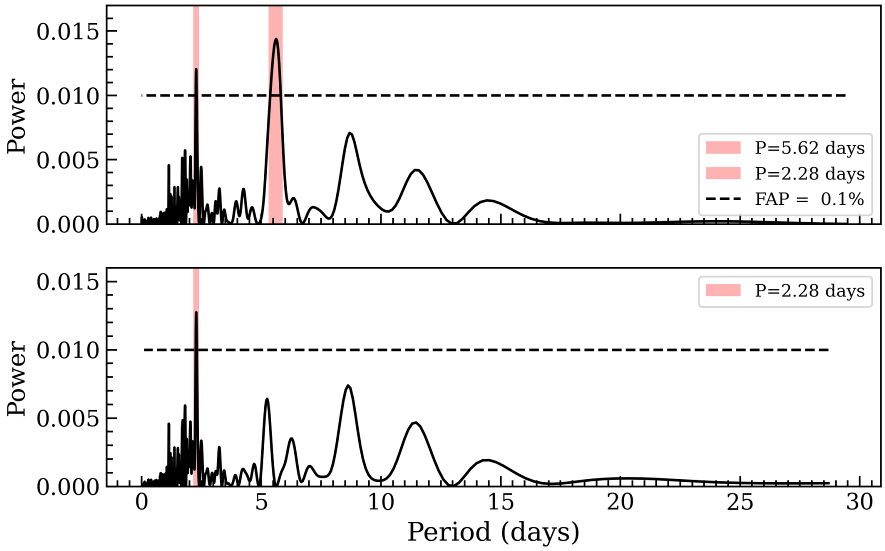

Figure 5.5: Upper panel: The GLS periodogram of TESS PDCSAP out-of-transit light curves of TOI-4603. The most significant peak can be seen at 5.62 days. There is another less significant peak at 2.28 days. Bottom panel: The GLS periodogram of residuals after removing the 5.62-day signal. The most significant peak is at 2.28 days. The black dashed line in both panels represents the FAP level of 0.1%.

(Lund et al., 2016). This computation yielded an approximate value of v_{max} at 700 μHz, which is smaller than the Nyquist frequency for the 2-minute cadence data ($\sim$4166 μHz). This shows that the TESS photometric data are well-suited for detecting these oscillations. The oscillation signals were analyzed employing the `lightkurve` package, and the power density spectra of the same TESS light curves were manually studied. Any significant solar-like oscillations in the star could not be detected.

5.3.2 Periodogram Analysis

Independent of photometry, the RV data from both spectrographs, PARAS and TRES, were analyzed for periodic signals using the GLS periodogram. Prior to analysis, instrumental offsets were corrected in the RVs. The resulting periodogram is displayed in panel 1 of Figure 5.6. To assess the significance of the signals, the FAP was calculated using equations described in Zechmeister &

Kürster (2009). The most significant signal appears at a period of 7.24 days, as

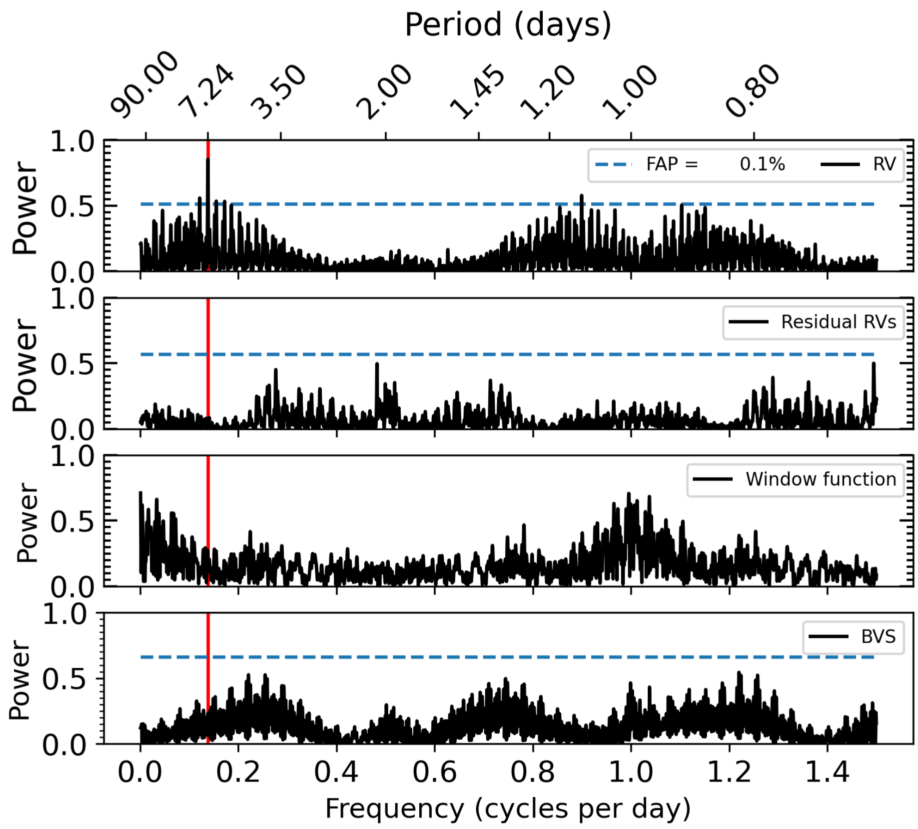

Figure 5.6: The GLS periodogram for the RV data, residual RVs, window function, and bisector slope for TOI-4603 are presented in panels 1, 2, 3, and 4 (from top to bottom), respectively. In panel 1, the main peak is observed at a period of approximately 7.24 days (indicated by the vertical red line), which aligns with the orbital period of the TOI-4603 b derived from photometry. The FAP level (horizontal dashed lines) of 0.1% for all the periodograms are shown in the legend of panels 1.

denoted by the vertical red line in Figure 5.6. This similar period was obtained from the transit data (see Section 5.2.1). The FAP of the 7.24-day signal was determined to be 0.007% based on a bootstrap method applied over a narrow range centered on this period. This provided robust confirmation of the periodic signal in our RV data set. Upon eliminating the 7.24-day periodic signal using the best-fit sinusoidal curve from the data sets, the other significant signals observed in the RV periodogram diminish, as demonstrated in the residual periodogram in panel 2.

The spectral window function is depicted in panel 3. The periodogram of bisectors (see panel 4) was computed to diagnose the origin of RV variations. Our analysis reveals no statistically significant signal of stellar activity or stellar contamination(with correlation coefficient ≈ 0.24, p-value $= 0.23$) in the data sets (see Chapter 3).

5.3.3 Global Modeling of TOI-4603 System

The parameters of the TOI-4603 system were constrained within the EXOFASTv2 framework. To determine the properties of the host star, SED fitting and MIST stellar isochrones were utilized. The SED fitting process involved using the broadband photometry data from various surveys, including Tycho BV (Høg et al., 2000), APASS data release (DR) 9 BV, SDSS gri (Henden et al., 2016), 2MASS JHK (Cutri et al., 2003), and ALL-WISE W1, W2, W3, and W4 (Cutri et al., 2021), as listed in Table 5.3. To ensure precise parameter estimation,

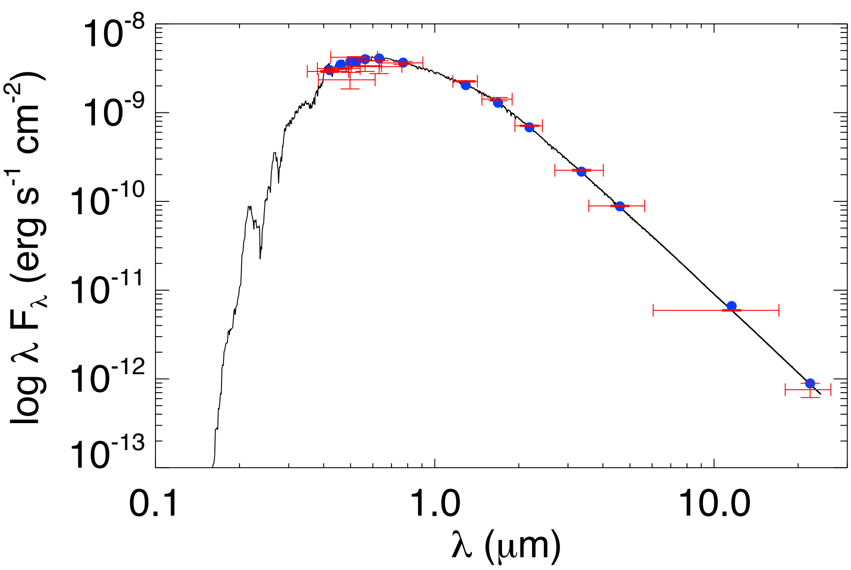

Figure 5.7: The spectral energy distribution (SED) curve of TOI-4603.

Gaussian priors on [Fe/H] and $T_{\rm eff}$ were incorporated, which were determined from spectroscopic analysis of the TCES spectra. Additionally, a Gaussian prior based on the parallax measurement from *Gaia* DR3 (Gaia Collaboration et al., 2022b) was applied, along with an upper limit of 1.59 on the V-band extinction, utilizing information from the Schlafly & Finkbeiner (2011) dust maps at the location of TOI-4603. Kurucz stellar atmospheric models (Kurucz, 1979) were used in the SED fitting process. The resulting best-fit SED model, considering the broadband photometry fluxes, is shown in Figure 5.7. In the plot, the

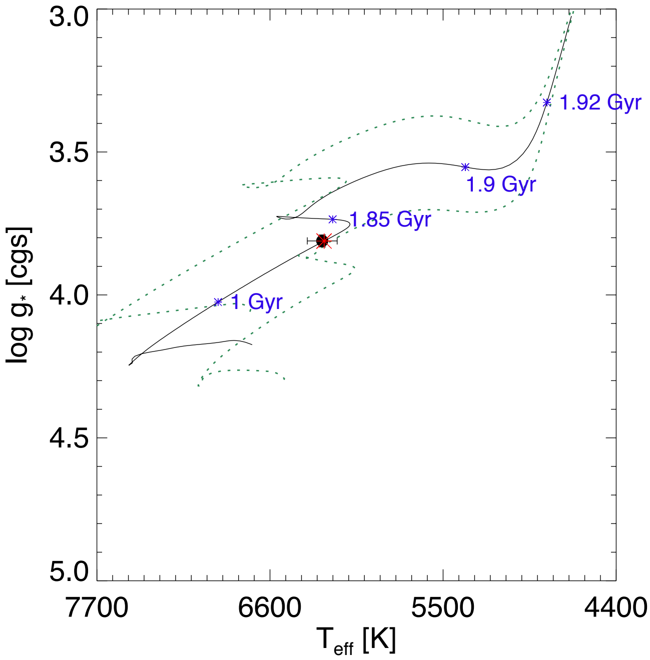

Figure 5.8: The MIST evolutionary track for TOI-4603 from EXOFASTv2 is shown by the solid black line. Two dashed lines represent the evolutionary tracks for 1.58 $M_{\odot}$ and 1.95 $M_{\odot}$ (representing the 3σ limits).

photometric measurements taken in each filter are represented by red markers with horizontal error bars, denoting their corresponding bandwidth. The vertical error bars indicate the uncertainty associated with these measurements. The black curve on the plot represents the best-fit Kurucz stellar atmosphere model and the model fluxes for each passband are depicted by blue circles placed along the curve. Moreover, EXOFASTv2 provided the most likely MIST evolutionary track, yielding an age of $1.64^{+0.30}_{-0.24}$ Gyr (refer to Figure 5.8).

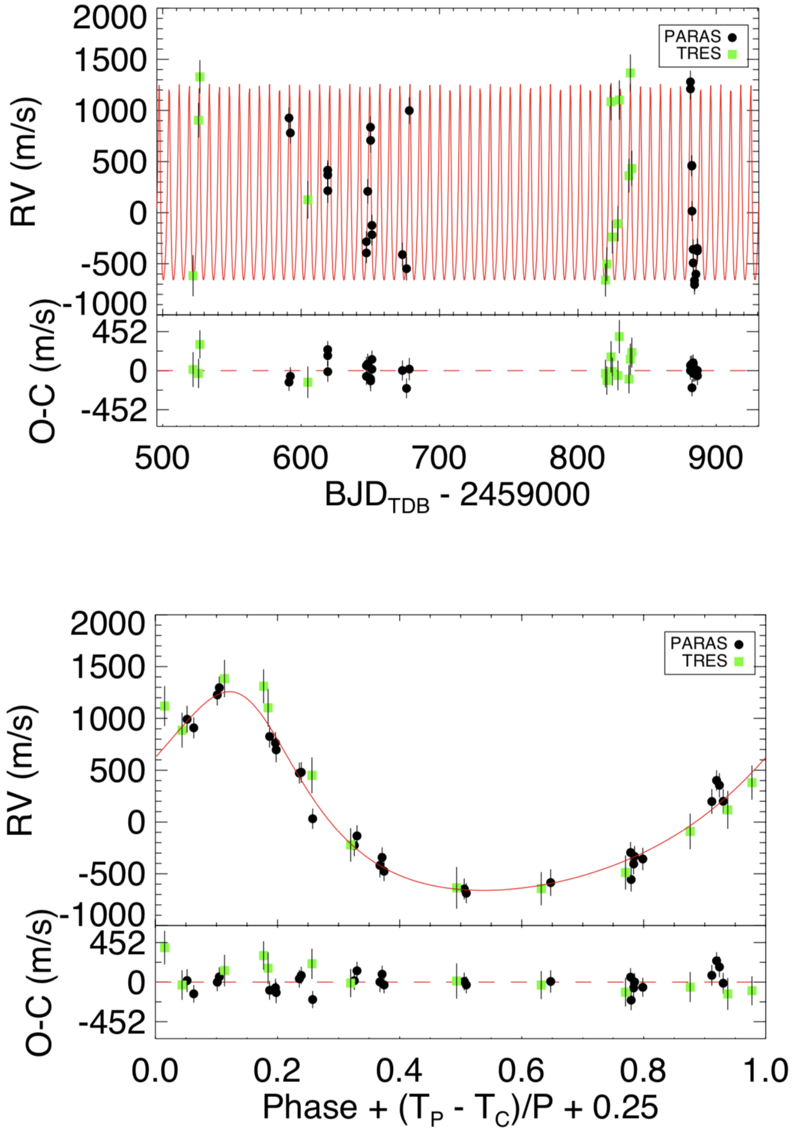

Figure 5.9: The RVs obtained from PARAS and TRES plotted against time (in upper panel) and an orbital phase of ∼7.24 days (in lower panel). The red line represents the best-fit RV model obtained using EXOFASTv2 (refer to Section 5.3.3). The bottom panel displays the residuals, showing the differences between the best-fit model and the actual data.

The adopted stellar parameters are as follows: $T_{\rm eff}$=6264^{+95}_{-94} K, [Fe/H]=$0.342^{+0.039}_{-0.040}$ dex, $\log g_*$=$3.810^{+0.021}_{-0.020}$ dex, M_*=1.765 ± 0.061 $M_\odot$, and R_*=$2.738^{+0.048}_{-0.050}$ $R_\odot$. All these parameters, along with their 1σ uncertainty, are summarized in Table 5.4.

Moreover, to determine the planetary parameters, simultaneous fitting of the RVs (PARAS and TRES RVs) and transit data (TESS light curves) was performed. All fitting parameters (e.g., b, i, R_p, a, K, ω, and e) were left unconstrained during the fitting process. Only the starting values of P and T$_c$, provided by the TESS QLP pipeline, were used as initial inputs. For the light curve fitting, the Mandel & Agol (2002) transit model was used, while a standard non-circular Keplerian orbit was used to model the RV data. In the analysis, the default quadratic limb-darkening law for the *TESS* passband was adopted, and the limb-darkening coefficients (u_1 and u_2) were computed using tables reported in Claret & Bloemen (2011) and Claret (2017). For each MCMC fit, 42 chains with 50000 steps were used, and the convergence of these fits was assessed using built-in Gelman-Rubin statistics (Gelman & Rubin, 1992; Ford, 2006). Figure 5.2 and Figure 5.9 display the transit and RV data alongside their respective best-fit models. Additionally, a long-term RV trend ($\dot{\gamma}$) in the RV data was also fitted, which resulted in a value of -0.14 ± 0.18 $ms^{-1}day^{-1}$ (see Section 5.4). However, it is important to note that this trend may not be significant due to its relatively high uncertainty. All the planetary parameters obtained through EXOFASTv2 are listed in Table 5.4.

5.4 Results and Discussion

5.4.1 Evolutionary Status of TOI-4603

The TOI-4603 has an effective temperature of 6268^{+94}_{-93} K, indicating it is an F7-type star (Pecaut & Mamajek, 2013). The Equal Evolutionary Point (EEP), which describes the common phases of evolutionary history, is ~ 400, suggesting that the star is still in the main sequence phase (See MIST documentation[‡]). It is less probable with respect to evolutionary timescales to observe a star in its turnoff point than to observe it near the middle of the main sequence phase. Also, it is possible that the star is still burning hydrogen but is likely to start its transition from MS to the RGB branch (Grieves et al., 2021b). However,

[‡]http://waps.cfa.harvard.edu/MIST/README_tables.pdf

the stellar radius of $2.736^{+0.049}_{-0.050}$ $R_\odot$ suggests that the star has a larger radius than predicted for the similar temperature main-sequence (MS) star, i.e., it is an evolved star, and the surface gravity $\log g_* = 3.811 \pm 0.021$ dex indicates that it is in sub-giant phase (Grieves et al., 2021b). The study by Reffert et al. (2015a) shows the host mass and planet occurrence relations, as discussed in 1.5.3 of Chapter 1. The authors found that as the stellar mass in the range from 1.0 to 1.9 $M_\odot$ increases, the giant-planet occurrence rate increased and rapidly dropped beyond 2.5 $M_\odot$ stellar mass. Even after this, other studies, particularly based on the stellar mass determination, have also shown the same results (Jones et al., 2016; Ghezzi et al., 2018). The TOI-4603 system follows a similar trend with the stellar mass of 1.767 ± 0.062 $M_\odot$ and hosts a massive planet ($M_P = 12.69^{+0.59}_{-0.60}$ M_J).

5.4.2 The Planetary Companion TOI-4603 b in Context

TOI-4603 b is found to have a mass, radius and density of $12.89^{+0.58}_{-0.57}$ M_J, $1.042^{+0.038}_{-0.035}$ R_J, and $14.1^{+1.7}_{-1.6}$ cgs, respectively. It transits a sub-giant F-type star in a 7.24599-day period. The discovery of TOI-4603 b is a significant contribution as it falls within the overlapping mass region (11 to $16 M_J$) of massive giant planets and low-mass BDs, based on the deuterium burning mass limit (Spiegel et al., 2011). The deuterium burning mass limit is $13 M_J$ for objects of solar metallicity, as defined by the IAU (Lecavelier des Etangs & Lissauer, 2022). However, this limit varies depending on factors like helium abundance, initial deuterium content, and the metallicity considered in the model. For instance, 10% of the initial deuterium can start burning at $11 M_J$ for a model with three times solar metallicity (Spiegel et al., 2011). Considering the metallicity of TOI-4603 b to be similar to its parent star (i.e., $0.342^{+0.039}_{-0.040}$ dex), the companion might have initiated deuterium fusion, thus not fulfilling the first criterion to be classified as a planet. However, based on the second criterion: TOI-4603 b has a mass ratio of 0.007 relative to the host star, placing it below the $L4/L5$ instability limit (<1/25), which supports its classification as an exoplanet. Distinguishing between planets and brown dwarfs in this mass range can be challenging (see Schneider et al. 2011 for a comprehensive overview). Many researchers, including Spiegel et al. (2011, and references therein), do not rigidly adhere to the deuterium burning mass limit as the fixed boundary for classifying planets and brown dwarfs. Instead, some studies propose alternative criteria, suggesting that a gas-giant planet's upper mass limit should be $25M_J$ (Pont et al., 2005; Udry, 2010; Anderson et al., 2011), or $60M_J$ (Hatzes & Rauer, 2015). As TOI-4603 b satisfies the criteria of a gas giant according to most of these definitions, we will refer to it as a planet in this context.

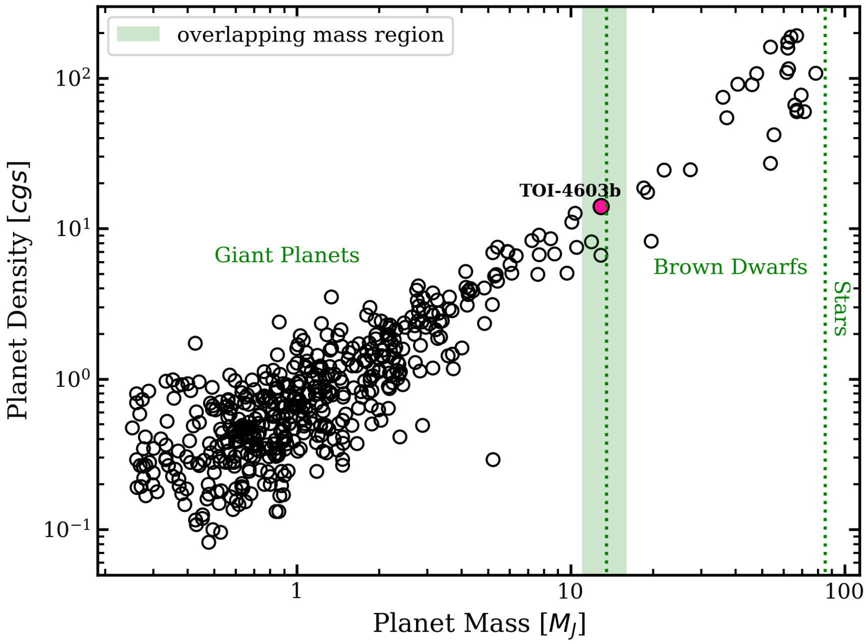

Figure 5.10: Planetary mass versus planetary density for all the transiting giant planets and BDs (0.25-85 M_J). The shaded green area in the plot shows the overlapping mass region of BDs and massive giant planets based on the deuterium burning limit, and the dotted vertical lines are at the mass M_P=$13M_J$ and M_P=$85M_J$. The magenta dot on the graph indicates the position of TOI-4603 b. Source: TEPcat database[††]

Figure 5.10 displays a mass versus density plot, including transiting gas-giant planets and BDs, with reported mass ranges between $0.25M_J$ (lower mass limit for gas giants from Dawson & Johnson, 2018) and $85M_J$ ($<0.08M_\odot$), where the mass and radius are determined with a precision better than 25%. There is a total of 5310 confirmed exoplanets, among which ∼1400 exoplanets have known masses[§]. Here we specifically focus on transiting giant planets with masses ranging from $0.25M_J$ to $13M_J$, leading to a subset of 477 transiting giant planets, including 35 massive giant planets ($M_P > 4M_J$)[††]. The plot highlights the overlapping mass region of massive giant planets and BDs ($11M_J < M_P < 16M_J$) based on deuterium burning with the shaded region. Notably, only three close-in transiting objects ($a < 0.1$ AU) have been discovered within this mass range, including TOI-4603 b from our study, along with HATS-70 b (Zhou et al., 2019a), and XO-3 b (Johns-Krull et al., 2008). This emphasizes the significance of TOI-4603 b as an important addition to the population of known giant planets within this mass range.

5.4.3 Internal structure[¶]

The heavy element content of TOI-4603 b was estimated following the approach described in Sarkis et al. (2021). Based on the planetary properties, the evolution model `completo21` (Mordasini et al., 2012) was used to calculate the planetary radius and we compared it with the observed radius. Our analysis assumes that the heavy elements in the envelope are homogeneously mixed, and these are modeled as water using the equation of state (EOS) of water ANEOS (Thompson, 1990; Mordasini, 2020). We did not include a central core like previous studies (Thorngren & Fortney, 2018; Komacek & Youdin, 2017). The envelope was coupled with a semi-gray atmospheric model, and the modeling of hydrogen and helium (He) was done using the SCvH EOS (Saumon et al., 1995) with a He mass fraction Y=0.27. A Bayesian approach was adopted to infer the planet's internal luminosity, which matches the observed radius given its mass and equilibrium temperature. A linear uniform prior for internal luminosity was provided, and heavy element content was informed by the relation from Thorngren et al. (2016). The planetary radius is well-reproduced in our analysis with a fraction of heavy elements of $0.13^{+0.05}_{-0.06}$. Considering the prior effect on the internal luminosity, the two values of heavy elements are consistent within the $1\,\sigma$ uncertainty range, as

[§] http://exoplanet.eu/

[¶] The interior modelling of the planet is done by Solene Ulmer-Moll, who is the co-author in Khandelwal et al. 2023.

noted in Sarkis et al. (2021). Using the derived fraction of heavy elements in the envelope, we calculated the metal enrichment of the planet to be Z_P/Z_{star}=$4.2^{+1.6}_{-2.0}$ (as done in Section 4.3 of Ulmer-Moll et al. 2022), and the total mass of heavy elements was estimated to be M_z=$532^{+205}_{-245}\,M_\oplus$. The posterior distribution of the fitted parameters is shown in Figure 5.13.

TOI-4603b presents an intriguing scientific opportunity to investigate planet formation processes at the transitional boundary between massive giant planets and BDs. According to Santos et al. (2017), two distinct populations of giant planets are categorized by masses above and below $\sim 4M_J$. In particular, their findings suggest a possible correlation between the formation of lower-mass giant planets and the core accretion process, with these planets often found in metal-rich host stars. On the other hand, higher-mass planets may arise from disk instability mechanisms and tend to orbit stars with lower average metallicity values. This theory was further supported by Schlaufman (2018) by finding that planets with masses $M_P < 4M_J$ predominantly orbit metal-rich hosts, while those with masses $M_P > 10M_J$ do not exhibit this trend. Despite its high metallicity ([Fe/H]=$0.342^{+0.039}_{-0.040}$ dex), TOI-4603 b does not conform to this trend and does not support the existence of any mass boundary at $4M_J$, as proposed by Adibekyan (2019). This suggests that irrespective of the metallicity of the host star, a massive giant planet can be formed through any processes (Adibekyan, 2019).

5.4.4 Eccentricity of TOI-4603 b and Tidal Circularization

TOI-4603 b is observed to be in an eccentric orbit (e=0.325 ± 0.020). Various processes, such as secular interactions, planet–disk interactions, planet-planet scattering, and HET migration, have been proposed to explain the orbital evolution of giant planets (for more details, refer to Section 2 of Dawson & Johnson 2018). In Figure 5.11, we present the observed population of transiting giant planets ($0.25M_J < M_P < 13M_J$) in the parameter space of eccentricity and semimajor axis (similar to Dong et al. 2021), utilizing data from the TEPcat database[††]. The region where HET migration could have occurred for planets following the constant angular momentum tracks are depicted in the shaded area, and the boundary of this region is defined by the Roche limit and the tidal circularization timescale, encompassing semimajor axes between 0.034 and 0.1 AU. The plot shows that the orbit of TOI-4603 b falls within this shaded area, indicating that the planet's orbit is currently undergoing the HET migration process.

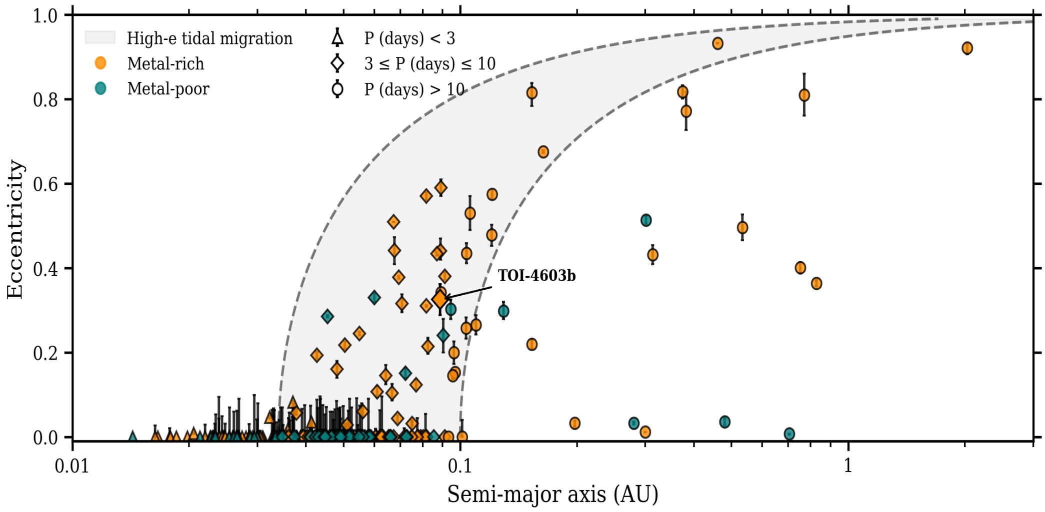

Figure 5.11: Plot of eccentricity vs. semimajor axis (AU) for transiting giant planets ($0.25M_J < M < 13M_J$) from TEPcat database[††] considering eccentricities are known with a precision better than 25%. Gray region shows the HET migration path (a=0.034-0.1 AU). The giant planets are color-coded according to their host's metallicity. Circles represent planets with $P > 10$ days, diamonds $3 < P < 10$ days, and triangles $P < 3$ days. TOI-4603 b's position is marked with an arrow.

Furthermore, the eccentricity distribution of giant planets (Figure 5.11) indicates that planets with orbital periods between 3 and 10 days have a broader range of eccentricities ($0.2 < e < 0.6$) compared to those with shorter periods ($e < 0.2$). The prevailing explanation for these moderate eccentricities is HET migration, which suggests that these eccentric giant planets are currently in the process of tidal circularization. Additionally, both circular and eccentric giants can be found at the same orbital periods, indicating that circular giant planets started their migration earlier than eccentric ones or experienced more efficient tidal dissipation effects. Some low eccentricities might be attributed to alternative formation channels, such as in situ formation or disk migration. Moreover, Figure 5.11 shows that most eccentric giant planets orbit metal-rich stars, while circular giant planets are found around both metal-poor and metal-rich stars. This observation aligns with the well-known correlation between the occurrence of giant planets and stellar metallicity, as established by Dawson & Murray-Clay (2013). Their findings support the idea of HET migration through planet–planet gravitational interaction. The eccentric orbit of TOI-4603 b and its metallic host star are consistent with this trend. Additionally, Kervella et al. (2019) reported the presence of a widely separated BD companion ($M_P \approx 20.52 M_J$) in the orbit of TOI-4603, which may contribute to this observed eccentricity. The shortest tidal circularization timescale (τ_{cir}) for TOI-4603 b was calculated to be 8.2 Gyr (for Q=10^5; Adams & Laughlin 2006), which exceeds the current age of the star determined in this work. This result aligns with tidal evolutionary theory, suggesting that the orbit of TOI-4603 b has not undergone circularization yet, which is consistent with our observations.

5.5 Summary of the Results for TOI-4603 System

The important results for TOI-4603 are summarized here as follows:

- Based on the global modeling of the TOI-4603 system, the planet is found to have a mass, radius, density, and temperature of $12.89^{+0.58}_{-0.57}$ M_J, $1.042^{+0.038}_{-0.035}$ R_J, $14.1^{+1.7}_{-1.6}$ cgs, and 1677 ± 24 K, respectively. The host star is an F-type ($T_{\rm eff}$=6264^{+95}_{-94} K), metal-rich ([Fe/H]=$0.342^{+0.039}_{-0.040}$ dex), sub-giant star ($\log g_*$=$3.810^{+0.021}_{-0.020}$ g cm^{-3}) that has a mass of 1.765 ± 0.061 $M_\odot$, radius of $2.738^{+0.048}_{-0.050}$ $R_\odot$, and age of $1.64^{+0.30}_{-0.24}$ Gyr (see Section 5.3.3).

- TOI-4603 b exhibits a measured eccentricity of 0.325 ± 0.020 and orbits at a distance of 0.0888 ± 0.0010 AU from its host star. These observations strongly suggest that the planet is undergoing HET migration (see

Section 5.4.4 and Figure 5.11).

- For the interior modeling of TOI-4603 b, a coreless model was considered, and the presence of heavy elements (water in this case) in the envelope was assumed to be homogeneously mixed. As a result, a fraction of heavy elements of $0.13^{+0.05}_{-0.06}$ and a metal enrichment of the planet (Z_P/Z_{star}) of $4.2^{+1.6}_{-2.0}$ were determined (see Section 5.4.3).

- The calculated shortest tidal circularization time scale is ~8.4 Gyr, which is higher than the estimated age of the system. This means that the orbit of TOI-4603 b has not been circularized, which is in agreement with our results.

- TOI-4603 b is one of the few known massive giant planets with an extreme density. Its location in the transition mass region between massive giant planets and low-mass brown dwarfs makes it a rare and valuable addition to the limited number of known objects in this specific mass range, which currently amounts to fewer than five (see Figure 5.10).

5.6 Appendix

Table 5.4: The priors, median values, and 68% confidence intervals for various physical parameters related to TOI-4603 as obtained from EXOFASTv2. Gaussian priors are denoted by $\mathcal{N}$, and Uniform priors are denoted by $\mathcal{U}$.

Parameter	Units	Adopted Priors	Values
Stellar Parameters:			
M_*	Mass ($M_\odot$)	–	1.765 ± 0.061
R_*	Radius ($R_\odot$)	–	$2.738^{+0.048}_{-0.050}$
L_*	Luminosity ($L_\odot$)	–	$10.40^{+0.65}_{-0.62}$
ρ_*	Density (cgs)	–	$0.1211^{+0.0077}_{-0.0071}$
$\log g$	Surface gravity (cgs)	–	$3.810^{+0.021}_{-0.020}$
$T_{\rm eff}$	Effective Temperature (K)	$\mathcal{N}$(6169, 128)	6264^{+95}_{-94}
[Fe/H]	Metallicity (dex)	–	$0.342^{+0.039}_{-0.040}$
Age	Age (Gyr)	–	$1.64^{+0.30}_{-0.24}$
EEP	Equal Evolutionary Point	–	$395.7^{+10.}_{-9.2}$
A_V	V-band extinction (mag)	$\mathcal{U}$(0, 1.5965)	$0.272^{+0.089}_{-0.090}$
σ_{SED}	SED photometry error scaling	–	$3.64^{+0.95}_{-0.66}$
$v \sin i$	Projected Rotational Velocity (km s^{-1})	–	23.18 ± 0.37
ϖ	Parallax (mas)	$\mathcal{N}$(4.4613, 0.01947)	4.462 ± 0.020
d	Distance (pc)	–	224.12 ± 0.99
$\dot{\gamma}$	RV slope (m/s/day)	–	-0.14 ± 0.18
Planetary Parameters:			b
P	Period (days)	–	$7.24599^{+0.00022}_{-0.00021}$
R_P	Radius ($R_{\rm J}$)	–	$1.042^{+0.038}_{-0.035}$
T_C	Time of conjunction ()	–	2459549.1260 ± 0.0014
a	Semi-major axis (AU)	–	0.0888 ± 0.0010
i	Inclination (Degrees)	–	$80.21^{+0.39}_{-0.41}$
e	Eccentricity	–	0.325 ± 0.020
ω_*	Argument of Periastron (Degrees)	–	$20.4^{+4.6}_{-4.7}$
T_{eq}	Equilibrium temperature (K)	–	1677 ± 24
M_P	Mass ($M_{\rm J}$)	–	$12.89^{+0.58}_{-0.57}$
K	RV semi-amplitude (m/s)	–	962^{+37}_{-35}
$logK$	Log of RV semi-amplitude	–	2.983 ± 0.016
R_P/R_*	Radius of planet in stellar radii	–	$0.0391^{+0.0012}_{-0.0010}$
a/R_*	Semi-major axis in stellar radii	–	6.97 ± 0.14
δ	Transit depth (fraction)	–	$0.001528^{+0.000091}_{-0.000079}$
$Depth$	Flux decrement at mid-transit	–	$0.001528^{+0.000090}_{-0.000079}$
T_{14}	Total transit duration (days)	–	0.1189 ± 0.0022
b	Transit Impact parameter	–	$0.9521^{+0.0044}_{-0.0049}$
ρ_P	Density (cgs)	–	$14.1^{+1.7}_{-1.6}$
$logg_P$	Surface gravity	–	$4.469^{+0.036}_{-0.037}$

$\langle F \rangle$	Incident Flux (10^9 erg s^{-1} cm^{-2})	–	$1.622^{+0.097}_{-0.092}$
T_P	Time of Periastron ()	–	$2459548.363^{+0.075}_{-0.083}$
$ecos\omega_*$		–	0.303 ± 0.019
$esin\omega_*$		–	0.113 ± 0.027
$M_P \sin i$	Minimum mass (M_J)	–	$12.70^{+0.57}_{-0.56}$
M_P/M_*	Mass ratio	–	$0.00698^{+0.00028}_{-0.00027}$
Wavelength Parameters:		TESS	
u_1	linear limb-darkening coeff	0.237 ± 0.050	
u_2	quadratic limb-darkening coeff	0.318 ± 0.050	
Telescope Parameters:		PARAS	TRES
$\gamma_{\rm rel}$	Relative RV Offset (m/s)	376^{+23}_{-24}	147^{+59}_{-56}
σ_J	RV Jitter (m/s)	95^{+25}_{-20}	185^{+68}_{-51}
σ_J^2	RV Jitter Variance	9100^{+5400}_{-3400}	35000^{+30000}_{-16000}
Transit Parameters:		TESS (TESS)	
σ^2	Added Variance	0.0000000151 ± 0.0000000018	
F_0	Baseline flux	1.0000094 ± 0.0000024	

BJD$_{TDB}$ Days	Relative-RV m s^{-1}	σ-RV m s^{-1}	BIS m s^{-1}	σ-BIS m s^{-1}	EXP-TIME s	Instrument
2459591.245018	1301.87	57.30	-2207.44	268.35	1800	PARAS
2459592.214846	1155.71	62.52	1217.54	199.04	1800	PARAS
2459619.190349	791.20	52.30	-92.82	249.29	1800	PARAS
2459619.224340	744.52	82.10	413.35	278.35	1800	PARAS
2459619.269151	589.99	83.52	236.22	255.28	1800	PARAS
2459647.154375	91.81	58.45	-22.06	128.41	1800	PARAS
2459647.190552	-18.86	54.08	-331.87	91.57	1800	PARAS
2459648.118842	584.50	84.86	-1495.12	285.70	1800	PARAS
2459650.113942	1211.70	66.83	-1008.67	149.20	1800	PARAS
2459650.191793	1082.77	86.56	-1048.42	206.49	1800	PARAS
2459651.119375	160.29	62.99	-451.66	147.03	1800	PARAS
2459651.150425	251.80	58.78	-991.27	247.10	1800	PARAS
2459673.160786	-35.14	82.03	259.99	224.52	1800	PARAS
2459676.145032	-172.45	79.06	-2088.29	231.24	1800	PARAS
2459678.118658	1374.26	99.56	-745.09	421.19	1800	PARAS
2459881.366954	1586.09	59.53	-1033.86	151.34	1800	PARAS
2459881.390763	1655.28	70.41	-1160.88	206.22	1800	PARAS
2459882.340429	831.30	56.21	-414.69	100.21	1800	PARAS
2459882.363486	838.82	52.98	248.93	439.60	1800	PARAS
2459882.498600	390.78	50.84	-417.80	230.02	1800	PARAS
2459883.322491	16.65	48.72	-1154.95	86.43	1800	PARAS
2459883.346278	-116.47	44.56	-393.03	170.19	1800	PARAS
2459884.297863	-287.89	56.43	-2149.04	106.84	1800	PARAS
2459884.321626	-328.58	48.01	-1984.25	99.19	1800	PARAS
2459885.323514	-226.52	96.69	-4272.63	284.06	1800	PARAS
2459886.321280	25.85	55.50	-3578.19	330.80	1800	PARAS
2459886.418752	1.46	68.72	2356.22	159.67	1800	PARAS
2459521.904947	-509	130	–	–	90	TRES
2459525.893170	1012	69	–	–	180	TRES
2459526.860655	1436	54	–	–	450	TRES
2459604.831871	234	99	–	–	270	TRES
2459819.997097	-552	46	–	–	360	TRES
2459820.998886	-396	58	–	–	180	TRES
2459824.001461	1193	96	–	–	195	TRES
2459824.981289	-130	50	–	–	400	TRES
2459829.013338	0.00	78	–	–	720	TRES
2459830.019859	1210	116	–	–	300	TRES
2459836.992174	470	59	–	–	210	TRES
2459837.976241	1474	95	–	–	180	TRES
2459839.014168	540	78	–	–	240	TRES

Table 5.1: RV measurements for TOI-4603, including BJD$_{TDB}$, relative RVs, RV errors, BVS, BVS errors, exposure time, and observation instruments.

Parameter	Description (unit)	Value	Source
α_{J2000}	Right Ascension	05:35:27.82	(1)
δ_{J2000}	Declination	+21:17:39.62	(1)
μ_α	PM in R.A. (mas yr^{-1})	0.102 ± 0.021	(1)
μ_δ	PM in Dec (mas yr^{-1})	-22.866 ± 0.011	(1)
π	Parallax (mas)	4.4613 ± 0.0195	(1)
G	*Gaia* G mag	9.0831 ± 0.0027	(1)
T	TESS T mag	8.6554 ± 0.0062	(2)
B_T	Tycho B mag	9.964 ± 0.026	(3)
V_T	Tycho V mag	9.273 ± 0.019	(3)
B	APASS B-mag	9.915 ± 0.03	(6)
V	APASS V-mag	9.421 ±0.15	(6)
g	SDSSg mag	9.968 ± 0.23	(6)
r	SDSSr mag	9.310 ± 0.18	(6)
i	SDSSi mag	8.976 ± 0.04	(6)
J	2MASS J mag	8.089 ± 0.020	(4)
H	2MASS H mag	7.788 ± 0.047	(4)
K_S	2MASS K$_S$ mag	7.786 ± 0.017	(4)
$W1$	WISE1 mag	7.718 ± 0.028	(5)
$W2$	WISE2 mag	7.744 ± 0.02	(5)
$W3$	WISE3 mag	7.761 ± 0.02	(5)
$W4$	WISE4 mag	7.933 ± 0.198	(5)
L_*	Luminosity ($L_\odot$)	9.74 [9.65, 9.80]	(1)
$T_{\rm eff}$	Effective Temperature (K)	6189 [6185, 6193]	(1)
$\log g$	Surface gravity (cgs)	3.805 [3.801, 3.818]	(1)
[M/H]	Metallicity (dex)	-0.236 [-0.239, -0.232]	(1)
M_*	Mass ($M_\odot$)	1.752 ± 0.088	(1)
R_*	Radius ($R_\odot$)	2.722 ± 0.136	(1)
Age	Age (Gyr)	1.98 [1.73, 2.22]	(1)

Other identifiers:

HD 245134[7]
TIC 437856897[2]
TYC 1309-1102-1[3]
2MASS J05352782+2117396[4]
Gaia EDR3 3402980516507429888[1]

Note: The metallicity of TOI-4603 reported by *Gaia* is different from our spectroscopic analysis (see Section 5.3.1).
References. (1) Gaia Collaboration et al. (2021), (2) Stassun et al. (2018), (3) Høg et al. (2000), (4) Cutri et al. (2003), (5) Cutri et al. (2021), (6) Henden et al. (2016), (7) Cannon & Pickering (1993).

Table 5.3: Basic stellar parameters for TOI-4603.

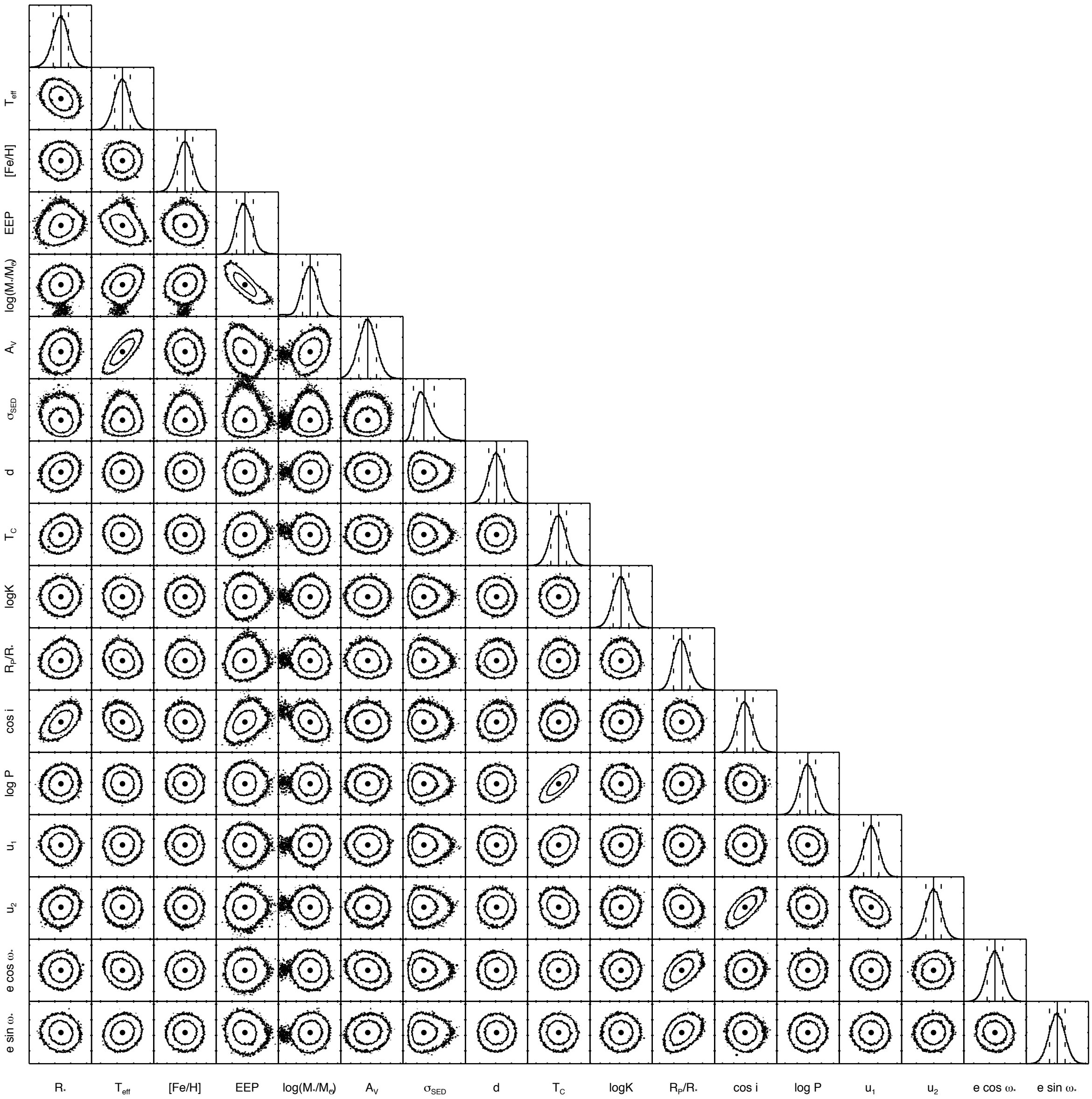

Figure 5.12: Corner plot summary of the posterior probability distribution showing the covariances for all the fitted parameters from EXOFASTv2 global fit for the TOI-4603.

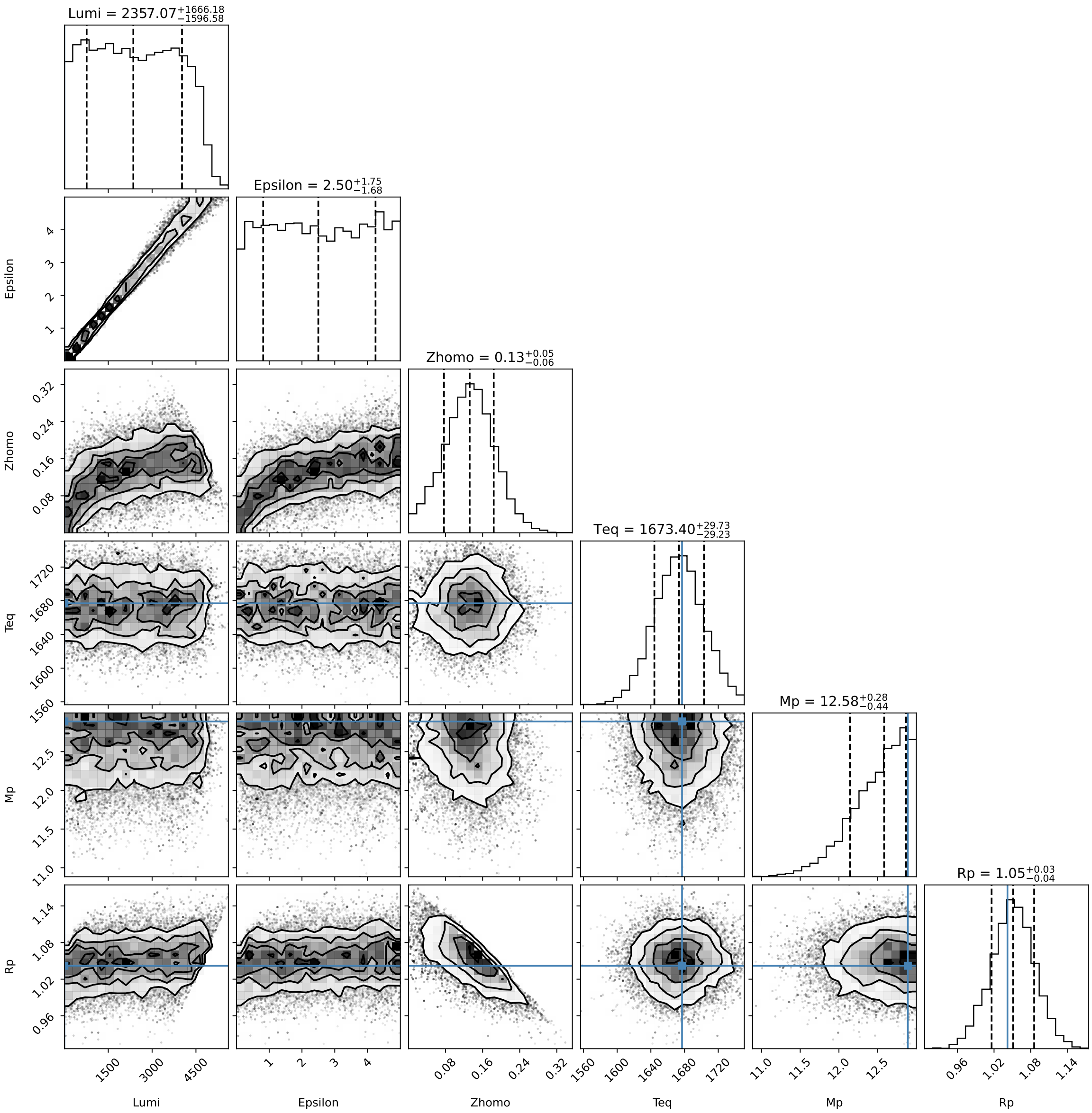

Figure 5.13: Corner plot summary of the posterior probability distribution for the interior modeling of TOI-4603 b.

Chapter 6

Summary and Future Work

6.1 Summary

The thesis focused on detecting and characterizing the close in giant planets (with periods $P \leq 10$), also known as hot Jupiters, around evolved stars. The motivation behind selecting potential evolved host candidates is elaborated in Chapter 1. It also provides insight into the historical evolution of exo-planetary science and various techniques for their detection, with the radial velocity method chosen as the primary approach for giant planet detection in this work. The chapter also discussed the formation, evolution, and migration mechanisms of close-in giant planets and presented the latest research on exoplanets around evolved stars.

To achieve the scientific objective of the thesis, precise RV measurements were obtained using the PARAS spectrograph. Chapter 2 provides a detailed description of the PARAS instrument, including its specifications, the RV precision limit, observation procedures, and the data reduction and analysis procedure. The candidates for RV follow-up observations were shortlisted from TESS photometric survey. Chapter 2 also discussed the candidate selection criteria for follow-up observations with PARAS. The candidates were shortlisted i) considering the candidates' observability in the night sky, taking into account their celestial coordinates during the non-monsoon months of the observing season at Mount Abu, India; ii) selecting candidates with spectral types of F, G, and K; and iii) with magnitudes of V<10. A total of 19[†] TOIs met the above criteria. Out of these 19, 8[‡] were previously ruled out as FPs, 2 were already declared as CPs (Schanche et al., 2020; Sha et al., 2021), and 2[‡] showed deviations from the expected photometric ephemeris. Consequently, only 7 out of the initial 19 candidates were left as PCs at that time. Subsequently, TESS confirmed 1 CP (Wittenmyer et al., 2021) and 2[‡] FPs among these 7 PCs. This led to a final selection of four candidates: TOI-1490, TOI-1684, TOI-1719, and TOI-1789. As TESS continued to release more candidates, 3 additional candidates were also shortlisted: TOI-2474, TOI-4543, and TOI-4603. In conclusion, seven candidates were shortlisted for this thesis work, as listed in Table 2.3. Three candidates (TOI-1789, TOI-4603, TOI-1490) out of the 7 exhibited RV variations. To investigate the origin of these RV variations, a Python script based on existing literature was developed for line bisector analysis, as discussed in Chapter 3. The results from the line bisector analysis provided supportive evidence for the presence of planetary companions around these stars. However, in the case of TOI-1490, additional RV observations are required to reach any conclusive results.

At the time of writing this thesis[¶], 17[‖] hot Jupiters have been discovered around evolved stars from TESS. It is noteworthy that at the outset of this research[†], only two hot Jupiters (Wang et al., 2019; Rodriguez et al., 2019) were known to orbit evolved stars with the TESS survey (Section 1.6). Subsequently, the sample has expanded with 15[‖] additional hot Jupiters, including two discovered by our study. The major contributions of this thesis are the successful detection of two close-in giant planets, TOI-1789 b and TOI-4603 b. The preceding chapters (Chapter 4 and Chapter 5) presented a detailed overview of the research conducted to obtain the physical and orbital parameters of these planetary systems. Table 6.1 presents a concise summary of the stellar and planetary parameters of both systems.

The host star TOI-1789 (V = 9.7) was followed-up using the PARAS and TCES spectrographs to measure the radial velocities and PRL's 0.43 m telescope to observe the transits. The planetary companion was found to have an orbital period of ∼3.20 days. The main stellar and planetary parameters

Parameters	TOI-1789	TOI-4603
M_* ($M_\odot$)	$1.507^{+0.059}_{-0.14}$	1.765 ± 0.061
R_* ($R_\odot$)	$2.168^{+0.036}_{-0.034}$	$2.738^{+0.048}_{-0.050}$
$T_{\rm eff}$ (K)	5991 ± 55	6264^{+95}_{-94}
[Fe/H] (dex)	$0.373^{+0.071}_{-0.086}$	$0.342^{+0.039}_{-0.040}$
$\log g_*$ (cgs)	$3.943^{+0.023}_{-0.043}$	$3.810^{+0.021}_{-0.020}$
M_P (M_J)	0.70 ± 0.16	$12.89^{+0.58}_{-0.57}$
R_P (R_J)	$1.44^{+0.24}_{-0.14}$	$1.042^{+0.038}_{-0.035}$
ρ_P (g cm^{-3})	$0.28^{+0.14}_{-0.12}$	$14.1^{+1.7}_{-1.6}$
P (days)	3.208664 ± 0.000015	$7.24599^{+0.00022}_{-0.00021}$

Table 6.1: Summary of giant planets discovered with PARAS as part of the thesis.

obtained through global modelling using EXOFASTv2 software are summarized in Table 6.1. The host star TOI-1789 is a metal-rich ([Fe/H] = $0.373^{+0.071}_{-0.086}$ dex) late F-type ($T_{\rm eff} = 5991 \pm 55$ K) slightly evolved ($\log g_*$ (cgs) $= 3.943^{+0.023}_{-0.043}$) star. The Table 6.1 shows that derived mass ($M_P = 0.70 \pm 0.16 M_J$) and radius ($R_J = 1.44^{+0.24}_{-0.14} R_J$) of TOI-1789 b exhibit a 4-σ significance and indicates an inflated radius compared to its planetary mass with a density of $0.28^{+0.14}_{-0.12}$ g cm^{-3}. As of now[††], eight exoplanets, including TOI-1789 b, orbit stars similar or more evolved than TOI-1789 at very close distances (a $\leq$ 0.05 AU) have been detected. Our findings indicate that the orbit of TOI-1789b might have already become circularized (section 4.4.2). This aligns with the estimated circularization timescale of 0.08 Gyr, which is shorter than the age of the system from this work. Despite the low occurrence of hot Jupiters around slightly evolved stars, TOI-1789 b appears to be entirely consistent with most of the evolutionary models in place, making it a non-anomalous case.

On the other hand, the follow-up radial velocity measurements for host star TOI-4603 ($V = 9.2$) were obtained using the PARAS and TRES spectrographs. The TOI-4603 is also a metal-rich ([Fe/H] = $0.342^{+0.039}_{-0.040}$ dex) late F-type ($T_{\rm eff} = 6264^{+95}_{-94}$ K) star that is in the sub-giant ($\log g_* = 3.810^{+0.021}_{-0.020}$ cgs) evolutionary phase. The planet TOI-4603 b has a mass, radius, and density of $12.89^{+0.58}_{-0.57} M_P$, $1.042^{+0.038}_{-0.035} R_J$ and $14.1^{+1.7}_{-1.6}$ g cm^{-3} respectively. This makes it one of the most densest and massive transiting giant planets discovered so far[¶]. It represents a valuable addition to the scarce population of only a few known massive close-in giant planets in the high-mass planet and low-mass BD overlapping region ($11M_J < M_P < 16M_J$; Spiegel et al., 2011). Discovering more such planets is crucial for comprehending the processes involved in their formation. The planet exhibits an eccentric orbit with a value of 0.325 ± 0.020, and this eccentricity could potentially be attributed to the presence of the BD companion in the system. The combination of the observed eccentricity and its proximity to the host star at an orbital distance of 0.0888 ± 0.0010 AU suggests that the planet is likely undergoing high-eccentricity tidal migration. The shortest tidal circularization timescale of TOI-4603 b is calculated to be 8.2 Gyr (for Q=10^5) which is greater than the star's current age determined from our work. This indicates that the planet's orbit has not yet been circularized, which is consistent with our results.

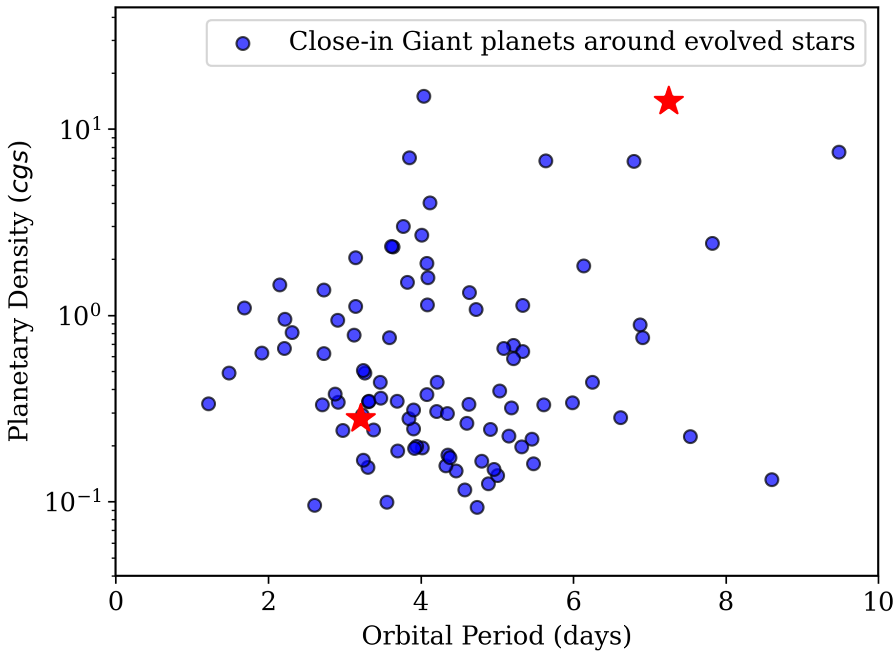

Figure 6.1: Planetary density versus planetary mass of close-in transiting giant planets around evolved stars. Only planets with estimates for both of these parameters with a precision better than 50% are included. The position of TOI-1789 b and TOI-4603 b are marked as red asterisks.

Moreover, the host stars TOI-1789 and TOI-4603 exhibit relatively similar properties (as depicted in Table 6.1), yet the planets orbiting them are remarkably distinct from one another. Figure 6.1 illustrates the orbital periods and planetary densities of all the known transiting hot Jupiters orbiting around evolved stars. The data is sourced from the TEPcat database[††], emphasizing the vast diversity in the density of these exoplanets. In the figure, the positions of TOI-1789b and TOI-4603b are marked as red asterisks. Notably, both of these discovered planets lie at the extreme ends of the density spectrum. This observation underscores the significant diversity within planetary systems. Further exploration of such systems will undoubtedly contribute to a deeper understanding of their origin and formation mechanisms.

6.2 Future Work

The detection of giant planets around evolved stars provides valuable insights into the interactions between planets and evolving stellar environments. However, the current number of such discovered planets remains limited (Figure 6.1). Studying them is crucial for learning more about these planets and improving the theoretical models. In the future, we will focus on detecting more of these systems. From the two detected planets as part of this thesis, there are several aspects one can study. The inflated planet, TOI-1789 b, provides an opportunity to investigate its atmospheric properties through transit observations (Charbonneau et al., 2005; Southworth, 2009; Winn, 2008). TOI-1789 b has a very low bulk density of $0.28^{+0.14}_{-0.12}$ g cm^3. The scale height of the atmosphere ($H = K_b T_{eq}/\mu g$), assuming it to be hydrogen-rich (μ of 2.3), was calculated to be 852 km (Madhusudhan et al., 2014). The Transmission Spectroscopy Metric (TSM) provided in TFOP observing notes is 129.2, but upon re-calculation using the parameters from this study and the formulation from Kempton et al. (2018), the TSM becomes 139.4. According to Kempton et al. (2018), TOI-1789 ranks in the top two quartiles among sub-Jovian planets, making it highly suitable for prioritized atmospheric characterization. Despite its favorable TSM and scale height values, the anticipated amplitude of spectral features in the transmission is only approximately 0.016%, mainly due to the large radii of the host star (Kreidberg, 2018). As a result, TOI-1789 may not be the most optimal target for ground-based transmission spectroscopy studies. However, it remains a suitable candidate for

JWST* or ARIEL studies (Tinetti et al., 2016).

Furthermore, TOI-1789 and TOI-4603, with their relatively bright magnitudes and unique positions in the evolutionary state, are well-suited candidates for studying the Rossiter-McLaughlin (R-M) effect. The R-M effect, first introduced by Rossiter (1924) and McLaughlin (1924), allows for investigating the projected stellar obliquity of planets. While most hot Jupiters align their orbits with the spin angle of their host stars, some may be found to be misaligned (Albrecht et al., 2012). Considering the v $\sin i$ of 7.0 ± 0.5 km s^{-1} and a larger stellar radius of $2.168^{+0.036}_{-0.034}$ $R_{\odot}$ for TOI-1789, the calculated R-M semi-amplitudes for the projected spin-orbit angle (λ) between 0° and 90° could range between 2.5 m s^{-1} and 16 m s^{-1}, respectively (Ohta et al., 2005). Moreover, TOI-4603 is a rapid rotator with a $v \sin i$ of 23.18 ± 0.37 km s^{-1} and a larger stellar radius of $2.738^{+0.048}_{-0.050}$ $R_{\odot}$, also making it a good choice for the R-M study. The RM semi-amplitude could range between 6.4 m s^{-1} and 31 m s^{-1} for the projected spin-orbit angle (λ) between 0° and 90°, respectively. Detecting the R-M effect for both stars is feasible through precise RV observations using moderate-sized telescopes (2.5-4 m aperture). For instance, PARAS-2 (Chakraborty et al., 2018b) at the 2.5 m telescope PRL is well-suited for conducting this research.

Moreover, one significant challenge in detecting Earth-like planets using RV measurements is the presence of stellar activity-induced RV signals that mimic or hide the planetary signal (Chapter 3). This contamination originates from the star itself and cannot be eliminated solely through improved instrumentation. Consequently, in order to discover planetary systems similar to our own Earth-Sun system where life could potentially exist, it is imperative to develop a more effective approach to identify and mitigate the effects of stellar activity from the stellar spectra. As a result, now, there is a focus on the development of stellar activity indicators (such as CaII H & K, Hα, and Na D) that are correlated with this contamination. By incorporating these indicators into the analysis models, mitigating the impact of stellar activity and enhancing the detection of low-mass planets is possible. In the future, this approach can be effectively applied to data obtained from the PARAS and PARAS-2 spectrographs.

*https://jwst.nasa.gov/science.html

Bibliography

Adams, F. C., & Laughlin, G. 2006, *The Astrophysical Journal*, 649, 1004 [Cited on pages 96 and 127.]

Adibekyan, V. 2019, Geosciences, 9, 105 [Cited on pages 108 and 125.]

Akaike, H. 1974, IEEE Transactions on Automatic Control, 19, 716 [Cited on page 93.]

Albrecht, S., Winn, J. N., Johnson, J. A., et al. 2012, *The Astrophysical Journal*, 757, 18 [Cited on page 140.]

Allen, L. E., Wright, J., Rajagopal, J., et al. 2018, in American Astronomical Society Meeting Abstracts, Vol. 231, American Astronomical Society Meeting Abstracts #231, 246.08 [Cited on page 16.]

Aller, A., Lillo-Box, J., Jones, D., Miranda, L. F., & Barceló Forteza, S. 2020, *Astronomy & Astrophysics*, 635, A128 [Cited on pages xii, xiv, 80, 110, and 111.]

Anderson, D. R., Collier Cameron, A., Hellier, C., et al. 2011, *The Astrophysical Journal Letters*, 726, L19 [Cited on pages 108 and 123.]

Andrews, J. J., Chanamé, J., & Agüeros, M. A. 2017, *Monthly Notices of Royal Astronomical Society*, 472, 675 [Cited on page 79.]

Armitage, P. J. 2020, Astrophysics of Planet Formation, 2nd edn. (Cambridge University Press), doi:10.1017/9781108344227 [Cited on page 20.]

Arras, P., & Socrates, A. 2010, *The Astrophysical Journal*, 714, 1 [Cited on page 23.]

Baglin, A., Auvergne, M., Boisnard, L., et al. 2006a, in 36th COSPAR Scientific Assembly, Vol. 36, 3749 [Cited on page 4.]

Baglin, A., Auvergne, M., Boisnard, L., et al. 2006b, in 36th COSPAR Scientific Assembly, Vol. 36, 3749 [Cited on page 75.]

Bailes, M., Bates, S. D., Bhalerao, V., et al. 2011, Science, 333, 1717 [Cited on page 14.]

Bailey, E., & Batygin, K. 2018, *The Astrophysical Journal Letters*, 866, L2 [Cited on page 19.]

Baraffe, I., Chabrier, G., Fortney, J., & Sotin, C. 2014, in Protostars and Planets VI, ed. H. Beuther, R. S. Klessen, C. P. Dullemond, & T. Henning, 763–786 [Cited on page 23.]

Baranne, A., Queloz, D., Mayor, M., et al. 1996, *Astronomy and Astrophysics Supplement Series*, 119, 373 [Cited on pages 16 and 52.]

Barclay, T., Pepper, J., & Quintana, E. V. 2018, *The Astrophysical Journal Supplement Series*, 239, 2 [Cited on page 41.]

Barenfeld, S. A., Carpenter, J. M., Ricci, L., & Isella, A. 2016, *The Astrophysical Journal*, 827, 142 [Cited on page 18.]

Baruteau, C., Crida, A., Paardekooper, S. J., et al. 2014, in Protostars and Planets VI, ed. H. Beuther, R. S. Klessen, C. P. Dullemond, & T. Henning, 667–689 [Cited on pages 20 and 108.]

Batygin, K., Bodenheimer, P. H., & Laughlin, G. P. 2016, *The Astrophysical Journal*, 829, 114 [Cited on page 19.]

Batygin, K., & Stevenson, D. J. 2010, *The Astrophysical Journal Letters*, 714, L238 [Cited on pages 23 and 108.]

Beleznay, M., & Kunimoto, M. 2022a, *Monthly Notices of Royal Astronomical Society*, 516, 75 [Cited on page 17.]

—. 2022b, *Monthly Notices of Royal Astronomical Society*, 516, 75 [Cited on page 26.]

Bento, J., Hartman, J. D., Bakos, G. Á., et al. 2018a, *Monthly Notices of Royal Astronomical Society*, 477, 3406 [Cited on pages 3 and 99.]

—. 2018b, *Monthly Notices of Royal Astronomical Society*, 477, 3406 [Cited on page 76.]

Bodenheimer, P., Lin, D. N. C., & Mardling, R. A. 2001, *The Astrophysical Journal*, 548, 466 [Cited on page 23.]

Borucki, W. J., Koch, D., Basri, G., et al. 2010, Science, 327, 977 [Cited on pages 4, 17, 33, and 75.]

Borucki, W. J., Koch, D. G., Basri, G., et al. 2011, *The Astrophysical Journal*, 736, 19 [Cited on page 15.]

Boss, A. P. 1997, Science, 276, 1836 [Cited on pages 17 and 18.]

Boss, A. P., Basri, G., Kumar, S. S., et al. 2003, in Brown Dwarfs, ed. E. Martín, Vol. 211, 529 [Cited on page 25.]

Boss, A. P., Butler, R. P., Hubbard, W. B., et al. 2005a, Proceedings of the International Astronomical Union, 1, 183–186 [Cited on pages 2 and 107.]

—. 2005b, Proceedings of the International Astronomical Union, 1, 183–186 [Cited on page 97.]

Bouchy, F., Díaz, R. F., Hébrard, G., et al. 2013, *Astronomy & Astrophysics*, 549, A49 [Cited on pages 38 and 65.]

Bouchy, F., Pepe, F., & Queloz, D. 2001, *Astronomy & Astrophysics*, 374, 733 [Cited on page 37.]

Bouchy, F., & Sophie Team. 2006, in Tenth Anniversary of 51 Peg-b: Status of and prospects for hot Jupiter studies, ed. L. Arnold, F. Bouchy, & C. Moutou, 319–325 [Cited on page 75.]

Bouchy, F., Wildi, F., & González Hernández, J. I. 2022, in European Planetary Science Congress, EPSC2022–937 [Cited on page 16.]

Bouchy, F., Udry, S., Mayor, M., et al. 2005, *Astronomy & Astrophysics*, 444, L15 [Cited on page 98.]

Bowler, B. P., Johnson, J. A., Marcy, G. W., et al. 2010, *The Astrophysical Journal*, 709, 396 [Cited on page 98.]

Brahm, R., Jordán, A., Hartman, J., & Bakos, G. 2017, *Monthly Notices of Royal Astronomical Society*, 467, 971 [Cited on page 115.]

Bruno, G. 1584, De l'Infinito, Universo e Mondi [Cited on page 2.]

Bruntt, H., Deleuil, M., Fridlund, M., et al. 2010, *Astronomy & Astrophysics*, 519, A51 [Cited on page 86.]

Buchhave, L. A., Bakos, G. Á., Hartman, J. D., et al. 2010, *The Astrophysical Journal*, 720, 1118 [Cited on page 114.]

Buchhave, L. A., Latham, D., Johansen, A., et al. 2012, Nature, 486, 375 [Cited on page 114.]

Buchhave, L. A., Bizzarro, M., Latham, D. W., et al. 2014, *Nature*, 509, 593 [Cited on page 114.]

Burnham, K. P., & Anderson, D. R. 2002, Model Selection and Multimodel Inference, 2nd edn. (New York: Springer-Verlag), doi:10.1007/b97636 [Cited on page 94.]

Burrows, A., Hubeny, I., Budaj, J., & Hubbard, W. B. 2007, *The Astrophysical Journal*, 661, 502 [Cited on pages 23 and 24.]

Butler, R. P., Marcy, G. W., Fischer, D. A., et al. 1999, *The Astrophysical Journal*, 526, 916 [Cited on page 3.]

Butler, R. P., Marcy, G. W., Williams, E., et al. 1996, *Publications of the Astronomical Society of the Pacific*, 108, 500 [Cited on page 85.]

Campante, T. L., Schofield, M., Kuszlewicz, J. S., et al. 2016, *The Astrophysical Journal*, 830, 138 [Cited on page 41.]

Campbell, B., & Walker, G. A. H. 1979, *Publications of the Astronomical Society of the Pacific*, 91, 540 [Cited on page 3.]

Cannon, A. J., & Pickering, E. C. 1993, VizieR Online Data Catalog, III/135A [Cited on pages 78 and 132.]

Carmichael, T. W., Quinn, S. N., Mustill, A. J., et al. 2020, *The Astronomical Journal*, 160, 53 [Cited on page 90.]

Carmichael, T. W., Quinn, S. N., Zhou, G., et al. 2021, *The Astronomical Journal*, 161, 97 [Cited on page 90.]

Castenmiller, M. J. M., Zwaan, C., & van der Zalm, E. B. J. 1986, , 105, 237 [Cited on page 58.]

Cegla, H. M., Watson, C. A., Shelyag, S., Mathioudakis, M., & Moutari, S. 2019, *The Astrophysical Journal*, 879, 55 [Cited on page 59.]

Chabrier, G., & Baraffe, I. 2007, *The Astrophysical Journal Letters*, 661, L81 [Cited on page 23.]

Chabrier, G., Johansen, A., Janson, M., & Rafikov, R. 2014, in Protostars and Planets VI, ed. H. Beuther, R. S. Klessen, C. P. Dullemond, & T. Henning, 619 [Cited on page 107.]

Chakraborty, A., Mahadevan, S., Roy, A., et al. 2010, in Society of Photo-Optical Instrumentation Engineers (SPIE) Conference Series, Vol. 7735, Ground-based and Airborne Instrumentation for Astronomy III, ed. I. S. McLean, S. K. Ramsay, & H. Takami, 77354N [Cited on pages xvii and 37.]

Chakraborty, A., Richardson, E., & Mahadevan, S. 2008, in Ground-based and Airborne Instrumentation for Astronomy II, Proceedings of SPIE - The International Society for Optical Engineering, ground-based and Airborne Instrumentation for Astronomy II ; Conference date: 23-06-2008 Through 28-06-2008 [Cited on page 37.]

Chakraborty, A., Roy, A., Sharma, R., et al. 2018a, *The Astronomical Journal*, 156, 3 [Cited on pages 34 and 38.]

Chakraborty, A., Thapa, N., Kumar, K., et al. 2018b, in Society of Photo-Optical Instrumentation Engineers (SPIE) Conference Series, Vol. 10702, Ground-based and Airborne Instrumentation for Astronomy VII, ed. C. J. Evans, L. Simard, & H. Takami, 107026G [Cited on page 140.]

Chakraborty, A., Mahadevan, S., Roy, A., et al. 2014, Publications of the Astronomical Society of the Pacific, 126, 133 [Cited on pages 38, 84, and 113.]

Chakraborty, A., Mahadevan, S., Roy, A., et al. 2014, *Publications of the Astronomical Society of the Pacific*, 126, 133 [Cited on pages v, x, xvii, 16, 34, 35, 36, 37, 47, and 49.]

Charbonneau, D., Brown, T. M., Latham, D. W., & Mayor, M. 2000, *The Astrophysical Journal Letters*, 529, L45 [Cited on page 3.]

Charbonneau, D., Brown, T. M., Noyes, R. W., & Gilliland, R. L. 2002, *The Astrophysical Journal*, 568, 377 [Cited on pages 4 and 24.]

Charbonneau, D., Allen, L. E., Megeath, S. T., et al. 2005, The Astrophysical Journal, 626, 523 [Cited on page 139.]

Chatterjee, S., Ford, E. B., Matsumura, S., & Rasio, F. A. 2008, *The Astrophysical Journal*, 686, 580 [Cited on page 21.]

Chaturvedi, P., Chakraborty, A., Anandarao, B. G., Roy, A., & Mahadevan, S. 2016, Monthly Notices of the Royal Astronomical Society, 462, 554 [Cited on page 34.]

Chaturvedi, P., Sharma, R., Chakraborty, A., Anandarao, B. G., & Prasad, N. J. S. S. V. 2018, The Astronomical Journal, 156, 27 [Cited on page 34.]

Chen, J., & Kipping, D. 2017, *The Astrophysical Journal*, 834, 17 [Cited on page 44.]

Choi, J., Dotter, A., Conroy, C., et al. 2016, *The Astrophysical Journal*, 823, 102 [Cited on page 90.]

Chubak, C., Marcy, G., Fischer, D. A., et al. 2012, arXiv e-prints, arXiv:1207.6212 [Cited on page 7.]

Ciardi, D. R., Beichman, C. A., Horch, E. P., & Howell, S. B. 2015, *The Astrophysical Journal*, 805, 16 [Cited on page 111.]

Claret, A. 2017, *Astronomy & Astrophysics*, 600, A30 [Cited on pages 93 and 121.]

Claret, A., & Bloemen, S. 2011, *Astronomy & Astrophysics*, 529, A75 [Cited on pages 93 and 121.]

Close, L. M., Puglisi, A., Males, J. R., et al. 2012, *The Astrophysical Journal*, 749, 180 [Cited on page 12.]

Collins, K. 2019, in American Astronomical Society Meeting Abstracts, Vol. 233, American Astronomical Society Meeting Abstracts #233, 140.05 [Cited on page 42.]

Collins, K. A., Kielkopf, J. F., Stassun, K. G., & Hessman, F. V. 2017, *The Astronomical Journal*, 153, 77 [Cited on page 82.]

Cosentino, R., Lovis, C., Pepe, F., et al. 2012, in Ground-based and Airborne Instrumentation for Astronomy IV, ed. I. S. McLean, S. K. Ramsay, & H. Takami, Vol. 8446, International Society for Optics and Photonics (SPIE), 84461V [Cited on page 16.]

Cumming, A., Butler, R. P., Marcy, G. W., et al. 2008, *Publications of the Astronomical Society of the Pacific*, 120, 531 [Cited on page 26.]

Curiel, S., Ortiz-León, G. N., Mioduszewski, A. J., & Sanchez-Bermudez, J. 2022, *The Astronomical Journal*, 164, 93 [Cited on pages 12 and 13.]

Cutri, R. M., Skrutskie, M. F., van Dyk, S., et al. 2003, VizieR Online Data Catalog, II/246 [Cited on pages 78, 90, 118, and 132.]

Cutri, R. M., Wright, E. L., Conrow, T., et al. 2021, VizieR Online Data Catalog, II/328 [Cited on pages 78, 90, 118, and 132.]

D'Angelo, G., Durisen, R. H., & Lissauer, J. J. 2010, in Exoplanets, ed. S. Seager, 319–346 [Cited on page 17.]

Davis, A. B., Cisewski, J., Dumusque, X., Fischer, D. A., & Ford, E. B. 2017, The Astrophysical Journal, 846 [Cited on page 57.]

Dawson, R. I., & Johnson, J. A. 2018, *Annual Review of Astronomy and Astrophysics*, 56, 175 [Cited on pages 16, 18, 97, 108, 123, and 125.]

Dawson, R. I., & Murray-Clay, R. A. 2013, *The Astrophysical Journal Letters*, 767, L24 [Cited on page 127.]

Dekany, R., Roberts, J., Burruss, R., et al. 2013, *The Astrophysical Journal*, 776, 130 [Cited on page 112.]

Demory, B.-O., & Seager, S. 2011a, *The Astrophysical Journal Supplement Series*, 197, 12 [Cited on pages 23 and 29.]

—. 2011b, *The Astrophysical Journal Supplement Series*, 197, 12 [Cited on page 100.]

Desidera, S., Gratton, R. G., Endl, M., et al. 2003, *Astronomy & Astrophysics*, 405, 207 [Cited on page 59.]

—. 2004, *Astronomy & Astrophysics*, 420, L27 [Cited on page 57.]

Dong, J., Huang, C. X., Zhou, G., et al. 2021, *The Astrophysical Journal Letters*, 920, L16 [Cited on page 125.]

Dotter, A. 2016, *The Astrophysical Journal Supplement Series*, 222, 8 [Cited on page 90.]

Doyle, A. P., Davies, G. R., Smalley, B., Chaplin, W. J., & Elsworth, Y. 2014, *Monthly Notices of Royal Astronomical Society*, 444, 3592 [Cited on page 86.]

Duffell, P. C., & Chiang, E. 2015, *The Astrophysical Journal*, 812, 94 [Cited on page 20.]

Dumusque, X. 2012, PhD thesis, University of Geneva, Astronomical Observatory [Cited on page 59.]

Dumusque, X. 2014, The Astrophysical Journal, 796 [Cited on page 57.]

Dumusque, X., Lovis, C., Udry, S., & Santos, N. C. 2011, in The Astrophysics of Planetary Systems: Formation, Structure, and Dynamical Evolution, ed. A. Sozzetti, M. G. Lattanzi, & A. P. Boss, Vol. 276, 530–532 [Cited on page 59.]

Durisen, R. H., Boss, A. P., Mayer, L., et al. 2007, in Protostars and Planets V, ed. B. Reipurth, D. Jewitt, & K. Keil, 607 [Cited on page 17.]

Eastman, J. D., Rodriguez, J. E., Agol, E., et al. 2019, arXiv e-prints, arXiv:1907.09480 [Cited on pages xii, 79, and 89.]

Endl, M., Kürster, M., & Els, S. 2000, *Astronomy & Astrophysics*, 362, 585 [Cited on page 85.]

Enoch, B., Collier Cameron, A., & Horne, K. 2012, *Astronomy & Astrophysics*, 540, A99 [Cited on page 23.]

Espinoza, N., Bayliss, D., Hartman, J. D., et al. 2016, *The Astronomical Journal*, 152, 108 [Cited on pages 3, 75, and 99.]

Eyer, L., & Grenon, M. 1997, in ESA Special Publication, Vol. 402, Hipparcos - Venice '97, ed. R. M. Bonnet, E. Høg, P. L. Bernacca, L. Emiliani, A. Blaauw, C. Turon, J. Kovalevsky, L. Lindegren, H. Hassan, M. Bouffard, B. Strim, D. Heger, M. A. C. Perryman, & L. Woltjer, 467–472 [Cited on page 66.]

Fabrycky, D., & Tremaine, S. 2007, *The Astrophysical Journal*, 669, 1298 [Cited on page 22.]

Fedele, D., van den Ancker, M. E., Henning, T., Jayawardhana, R., & Oliveira, J. M. 2010, *Astronomy & Astrophysics*, 510, A72 [Cited on page 18.]

Fűrész, G. 2008, PhD thesis, University of Szeged, Hungary [Cited on pages 16 and 114.]

Fischer, D. A., & Valenti, J. 2005a, *The Astrophysical Journal*, 622, 1102 [Cited on page 25.]

—. 2005b, *The Astrophysical Journal*, 622, 1102 [Cited on page 98.]

Fischer, D. A., Laughlin, G., Butler, P., et al. 2005, *The Astrophysical Journal*, 620, 481 [Cited on page 98.]

Fischer, D. A., Vogt, S. S., Marcy, G. W., et al. 2007, *The Astrophysical Journal*, 669, 1336 [Cited on page 96.]

Fischer, D. A., Anglada-Escude, G., Arriagada, P., et al. 2016, *Publications of the Astronomical Society of the Pacific*, 128, 066001 [Cited on page 34.]

Ford, E. B. 2006, *The Astrophysical Journal*, 642, 505 [Cited on pages 89 and 121.]

Ford, E. B., & Rasio, F. A. 2005, arXiv e-prints, astro [Cited on page 21.]

Fortney, J. J., Dawson, R. I., & Komacek, T. D. 2021, Journal of Geophysical Research (Planets), 126, e06629 [Cited on pages x, 19, and 23.]

Fortney, J. J., Marley, M. S., & Barnes, J. W. 2007, *The Astrophysical Journal*, 659, 1661 [Cited on page 24.]

Fortney, J. J., & Nettelmann, N. 2010, *Space Science Reviews*, 152, 423 [Cited on page 23.]

Franson, K., Bowler, B. P., Zhou, Y., et al. 2023, arXiv e-prints, arXiv:2302.05420 [Cited on page 12.]

Fressin, F., Torres, G., Charbonneau, D., et al. 2013, *The Astrophysical Journal*, 766, 81 [Cited on page 26.]

Fridlund, M., Gaidos, E., Barragán, O., et al. 2017, *Astronomy & Astrophysics*, 604, A16 [Cited on page 86.]

Frink, S., Quirrenbach, A., Fischer, D., Röser, S., & Schilbach, E. 2001, *Publications of the Astronomical Society of the Pacific*, 113, 173 [Cited on page 98.]

Fulton, B. J., Petigura, E. A., Howard, A. W., et al. 2017, *The Astronomical Journal*, 154, 109 [Cited on page 15.]

Furlan, E., Ciardi, D. R., Everett, M. E., et al. 2017, *The Astronomical Journal*, 153, 71 [Cited on page 113.]

Gaia Collaboration, Brown, A. G. A., Vallenari, A., et al. 2021, *Astronomy & Astrophysics*, 649, A1 [Cited on pages 78, 79, 90, and 132.]

Gaia Collaboration, Vallenari, A., Brown, A. G. A., et al. 2022a, arXiv e-prints, arXiv:2208.00211 [Cited on page 13.]

—. 2022b, arXiv e-prints, arXiv:2208.00211 [Cited on page 118.]

Gelman, A., & Rubin, D. B. 1992, Statistical Science, 7, 457 [Cited on pages 89 and 121.]

Ghezzi, L., Montet, B. T., & Johnson, J. A. 2018, *The Astrophysical Journal*, 860, 109 [Cited on pages 25, 28, and 122.]

Gold, Ambartsumian, V. A., Moroz, V. I., & Pariisky. 1973, in Communication With Extraterrestrial Intelligence, ed. C. Sagan, 8 [Cited on page 2.]

Goldreich, P., & Tremaine, S. 1980, *The Astrophysical Journal*, 241, 425 [Cited on page 20.]

Goldreich, P., & Ward, W. R. 1973, *The Astrophysical Journal*, 183, 1051 [Cited on page 17.]

Gonzalez, G. 1997a, *Monthly Notices of Royal Astronomical Society*, 285, 403 [Cited on page 25.]

—. 1997b, *Monthly Notices of Royal Astronomical Society*, 285, 403 [Cited on page 98.]

Gray, D. F. 1988, Lectures on spectral-line analysis: F,G, and K stars [Cited on pages 58 and 61.]

Grieves, N., Nielsen, L. D., Vines, J. I., et al. 2021a, *Astronomy & Astrophysics*, 647, A180 [Cited on page 90.]

—. 2021b, *Astronomy & Astrophysics*, 647, A180 [Cited on pages 121 and 122.]

Grunblatt, S. K., Huber, D., Gaidos, E., et al. 2019, *The Astronomical Journal*, 158, 227 [Cited on pages 26 and 29.]

—. 2018, *The Astrophysical Journal Letters*, 861, L5 [Cited on pages 28 and 29.]

Guenther, E. W., Hartmann, M., Esposito, M., et al. 2009, *Astronomy & Astrophysics*, 507, 1659 [Cited on pages 85 and 115.]

Guillot, T., & Showman, A. P. 2002, *Astronomy & Astrophysics*, 385, 156 [Cited on page 99.]

Haisch, Karl E., J., Lada, E. A., & Lada, C. J. 2001, *The Astrophysical Journal Letters*, 553, L153 [Cited on page 18.]

Hamers, A. S., Antonini, F., Lithwick, Y., Perets, H. B., & Portegies Zwart, S. F. 2017, *Monthly Notices of Royal Astronomical Society*, 464, 688 [Cited on page 22.]

Hansen, B. M. S. 2010, *The Astrophysical Journal*, 723, 285 [Cited on page 96.]

Hartman, J. D., Bakos, G. Á., Béky, B., et al. 2012, *The Astronomical Journal*, 144, 139 [Cited on page 75.]

Hartman, J. D., Bakos, G. Á., Bhatti, W., et al. 2016, *The Astronomical Journal*, 152, 182 [Cited on page 28.]

Hatzes, A. P. 2016, The Radial Velocity Method for the Detection of Exoplanets, ed. V. Bozza, L. Mancini, & A. Sozzetti (Cham: Springer International Publishing), 3–86 [Cited on page 59.]

Hatzes, A. P., & Cochran, W. D. 1992, in European Southern Observatory Conference and Workshop Proceedings, Vol. 40, European Southern Observatory Conference and Workshop Proceedings, 275 [Cited on page 37.]

Hatzes, A. P., Cochran, W. D., & Bakker, E. J. 1998, *The Astrophysical Journal*, 508, 380 [Cited on page 66.]

Hatzes, A. P., Cochran, W. D., Endl, M., et al. 2003, *The Astrophysical Journal*, 599, 1383 [Cited on page 96.]

Hatzes, A. P., & Rauer, H. 2015, *The Astrophysical Journal Letters*, 810, L25 [Cited on pages 108 and 123.]

Hayashi, C. 1981, Progress of Theoretical Physics Supplement, 70, 35 [Cited on page 17.]

Hayward, T. L., Brandl, B., Pirger, B., et al. 2001, *Publications of the Astronomical Society of the Pacific*, 113, 105 [Cited on page 111.]

Heintz, W. D. 1988, , 82, 140 [Cited on page 2.]

Hekker, S., & Meléndez, J. 2007, *Astronomy & Astrophysics*, 475, 1003 [Cited on page 25.]

Henden, A. A., Templeton, M., Terrell, D., et al. 2016, VizieR Online Data Catalog, II/336 [Cited on pages 78, 90, 118, and 132.]

Henry, G. W., Marcy, G. W., Butler, R. P., & Vogt, S. S. 2000, *The Astrophysical Journal Letters*, 529, L41 [Cited on pages 4 and 66.]

Hershey, J. L. 1973, *The Astronomical Journal*, 78, 421 [Cited on page 2.]

Hirano, T., Dai, F., Gandolfi, D., et al. 2018, *The Astronomical Journal*, 155, 127 [Cited on page 86.]

Høg, E., Fabricius, C., Makarov, V. V., et al. 2000, *Astronomy & Astrophysics*, 355, L27 [Cited on pages 78, 90, 118, and 132.]

Howard, A. W., Marcy, G. W., Bryson, S. T., et al. 2012, *The Astrophysical Journal Supplement Series*, 201, 15 [Cited on page 26.]

Howell, S. B., Everett, M. E., Horch, E. P., et al. 2016, *The Astrophysical Journal Letters*, 829, L2 [Cited on page 83.]

Howell, S. B., Everett, M. E., Sherry, W., Horch, E., & Ciardi, D. R. 2011, The Astronomical Journal, 142, 19 [Cited on page 83.]

Howell, S. B., Sobeck, C., Haas, M., et al. 2014, *Publications of the Astronomical Society of the Pacific*, 126, 398 [Cited on pages 4 and 33.]

Huang, C. X., Vanderburg, A., Pál, A., et al. 2020, Research Notes of the American Astronomical Society, 4, 204 [Cited on page 76.]

Ibrahim, I., Malasan, H. L., Djamal, M., et al. 2015, Publication of Korean Astronomical Society, 30, 235 [Cited on page 13.]

Ida, S., & Lin, D. N. C. 2005, *The Astrophysical Journal*, 626, 1045 [Cited on page 95.]

Ikwut-Ukwa, M., Rodriguez, J. E., Bieryla, A., et al. 2020, *The Astronomical Journal*, 160, 209 [Cited on page 90.]

Jacob, W. S. 1855, *Monthly Notices of Royal Astronomical Society*, 15, 228 [Cited on page 2.]

Jenkins, J., Twicken, J., McCauliff, S., et al. 2016, in Software and Cyber infrastructure for Astronomy IV [Cited on page 76.]

Jofré, E., Petrucci, R., Saffe, C., et al. 2015, *Astronomy & Astrophysics*, 574, A50 [Cited on page 25.]

Johns-Krull, C. M., McCullough, P. R., Burke, C. J., et al. 2008, *The Astrophysical Journal*, 677, 657 [Cited on page 124.]

Johnson, J. A., Aller, K. M., Howard, A. W., & Crepp, J. R. 2010a, *Publications of the Astronomical Society of the Pacific*, 122, 905 [Cited on pages 25, 26, and 27.]

Johnson, J. A., Howard, A. W., Bowler, B. P., et al. 2010b, *Publications of the Astronomical Society of the Pacific*, 122, 701 [Cited on page 96.]

Johnson, J. A., Marcy, G. W., Fischer, D. A., et al. 2008, *The Astrophysical Journal*, 675, 784 [Cited on page 96.]

Johnson, J. A., Fischer, D. A., Marcy, G. W., et al. 2007, *The Astrophysical Journal*, 665, 785 [Cited on page 96.]

Johnson, J. A., Payne, M., Howard, A. W., et al. 2011a, *The Astronomical Journal*, 141, 16 [Cited on page 89.]

Johnson, J. A., Clanton, C., Howard, A. W., et al. 2011b, *The Astrophysical Journal Supplement Series*, 197, 26 [Cited on page 96.]

Jones, M. I., Jenkins, J. S., Brahm, R., et al. 2016, *Astronomy & Astrophysics*, 590, A38 [Cited on pages 25, 26, 28, and 122.]

Jurgenson, C., Fischer, D., McCracken, T., et al. 2016, in Society of Photo-Optical Instrumentation Engineers (SPIE) Conference Series, Vol. 9908, Ground-based and Airborne Instrumentation for Astronomy VI, ed. C. J. Evans, L. Simard, & H. Takami, 99086T [Cited on page 16.]

Keenan, P. C., & McNeil, R. C. 1989, *The Astrophysical Journal Supplement Series*, 71, 245 [Cited on page 66.]

Kempton, E. M. R., Bean, J. L., Louie, D. R., et al. 2018, *Publications of the Astronomical Society of the Pacific*, 130, 114401 [Cited on page 139.]

Kennedy, G. M., & Kenyon, S. J. 2008, *The Astrophysical Journal*, 673, 502 [Cited on page 95.]

Kervella, P., Arenou, F., Mignard, F., & Thévenin, F. 2019, *Astronomy & Astrophysics*, 623, A72 [Cited on page 127.]

Kipping, D. M. 2010, *Monthly Notices of Royal Astronomical Society*, 408, 1758 [Cited on page 93.]

Komacek, T. D., Thorngren, D. P., Lopez, E. D., & Ginzburg, S. 2020, *The Astrophysical Journal*, 893, 36 [Cited on page 99.]

Komacek, T. D., & Youdin, A. N. 2017, *The Astrophysical Journal*, 844, 94 [Cited on page 124.]

Kovács, G., Zucker, S., & Mazeh, T. 2002, *Astronomy & Astrophysics*, 391, 369 [Cited on pages 77 and 110.]

Kozai, Y. 1962, *The Astronomical Journal*, 67, 591 [Cited on page 22.]

Kreidberg, L. 2018, Exoplanet Atmosphere Measurements from Transmission Spectroscopy and Other Planet Star Combined Light Observations, ed. H. J. Deeg & J. A. Belmonte, 100 [Cited on page 139.]

Kunimoto, M., & Matthews, J. M. 2020, *The Astronomical Journal*, 159, 248 [Cited on page 26.]

Kunitomo, M., Ikoma, M., Sato, B., Katsuta, Y., & Ida, S. 2011, *The Astrophysical Journal*, 737, 66 [Cited on page 96.]

Kurucz, R. L. 1979, *The Astrophysical Journal Supplement Series*, 40, 1 [Cited on pages 90 and 119.]

Kurucz, R. L. 1992, in The Stellar Populations of Galaxies, ed. B. Barbuy & A. Renzini, Vol. 149, 225 [Cited on page 114.]

—. 2013, ATLAS12: Opacity sampling model atmosphere program, ascl:1303.024 [Cited on page 86.]

Lai, D. 2012, *Monthly Notices of Royal Astronomical Society*, 423, 486 [Cited on page 23.]

Laughlin, G., Crismani, M., & Adams, F. C. 2011a, *The Astrophysical Journal Letters*, 729, L7 [Cited on page 23.]

—. 2011b, *The Astrophysical Journal Letters*, 729, L7 [Cited on page 75.]

Lecavelier des Etangs, A., & Lissauer, J. J. 2022, *New Astronomy Reviews*, 94, 101641 [Cited on pages 108 and 122.]

Léger, A., Rouan, D., Schneider, J., et al. 2009, *Astronomy & Astrophysics*, 506, 287 [Cited on page 4.]

Lendl, M., Anderson, D. R., Bonfanti, A., et al. 2019, *Monthly Notices of Royal Astronomical Society*, 482, 301 [Cited on page 99.]

Li, G., Naoz, S., Kocsis, B., & Loeb, A. 2014, *The Astrophysical Journal*, 785, 116 [Cited on page 22.]

Lidov, M. L. 1962, , 9, 719 [Cited on page 22.]

Lightkurve Collaboration, Cardoso, J. V. d. M., Hedges, C., et al. 2018, Lightkurve: Kepler and TESS time series analysis in Python, Astrophysics Source Code Library, ascl:1812.013 [Cited on pages 77 and 110.]

Lillo-Box, J., Barrado, D., & Correia, A. C. M. 2016, *Astronomy & Astrophysics*, 589, A124 [Cited on page 26.]

Lin, D. N. C., Bodenheimer, P., & Richardson, D. C. 1996, *Nature*, 380, 606 [Cited on page 20.]

Lissauer, J. J. 1993, Annual Review of Astronomy and Astrophysics, 31, 129 [Cited on page 3.]

Lloyd, J. P. 2011, *The Astrophysical Journal Letters*, 739, L49 [Cited on page 27.]

—. 2013, *The Astrophysical Journal Letters*, 774, L2 [Cited on page 27.]

Lopez, E. D., & Fortney, J. J. 2016, *The Astrophysical Journal*, 818, 4 [Cited on page 29.]

Lorimer, D. R. 2001, Living Reviews in Relativity, 4, 5 [Cited on page 13.]

Louden, T., & Wheatley, P. J. 2015, *The Astrophysical Journal Letters*, 814, L24 [Cited on page 17.]

Lovis, C., & Pepe, F. 2007, *Astronomy & Astrophysics*, 468, 1115 [Cited on page 50.]

Lubin, J., Robertson, P., Stefansson, G., et al. 2021, arXiv e-prints, arXiv:2105.07005 [Cited on page 57.]

Lund, M. N., Chaplin, W. J., Casagrande, L., et al. 2016, *Publications of the Astronomical Society of the Pacific*, 128, 124204 [Cited on page 116.]

Macintosh, B., Graham, J. R., Barman, T., et al. 2015, Science, 350, 64 [Cited on page 12.]

Madhusudhan, N., Knutson, H., Fortney, J. J., & Barman, T. 2014, in Protostars and Planets VI, ed. H. Beuther, R. S. Klessen, C. P. Dullemond, & T. Henning, 739 [Cited on page 139.]

Mahadevan, S., Ramsey, L., Bender, C., et al. 2012, in Society of Photo-Optical Instrumentation Engineers (SPIE) Conference Series, Vol. 8446, Ground-based and Airborne Instrumentation for Astronomy IV, ed. I. S. McLean, S. K. Ramsay, & H. Takami, 84461S [Cited on page 16.]

Makarov, V. V. 2010, *The Astrophysical Journal*, 715, 500 [Cited on page 59.]

Maldonado, J., Villaver, E., & Eiroa, C. 2013, *Astronomy & Astrophysics*, 554, A84 [Cited on page 25.]

Maldonado, J., Phillips, D. F., Dumusque, X., et al. 2019, *Astronomy & Astrophysics*, 627, A118 [Cited on pages 58 and 59.]

Mandel, K., & Agol, E. 2002, *The Astrophysical Journal Letters*, 580, L171 [Cited on pages 11, 93, and 121.]

Marcy, G., Butler, R. P., Fischer, D., et al. 2005, Progress of Theoretical Physics Supplement, 158, 24 [Cited on pages 17 and 26.]

Martínez Fiorenzano, A. F., Gratton, R. G., Desidera, S., Cosentino, R., & Endl, M. 2005, *Astronomy & Astrophysics*, 442, 775 [Cited on pages 55, 57, 60, and 61.]

Matsumura, S., Peale, S. J., & Rasio, F. A. 2010, *The Astrophysical Journal*, 725, 1995 [Cited on page 22.]

Matsuo, T., Shibai, H., Ootsubo, T., & Tamura, M. 2007, *The Astrophysical Journal*, 662, 1282 [Cited on page 18.]

Mayor, M., & Queloz, D. 1995, *Nature*, 378, 355 [Cited on page 3.]

Mayor, M., Pepe, F., Queloz, D., et al. 2003, The Messenger, 114, 20 [Cited on pages 16 and 75.]

Mayor, M., Marmier, M., Lovis, C., et al. 2011, arXiv e-prints, arXiv:1109.2497 [Cited on pages 17 and 26.]

Mazeh, T. 2008, in EAS Publications Series, Vol. 29, EAS Publications Series, ed. M. J. Goupil & J. P. Zahn, 1–65 [Cited on pages 96 and 98.]

McLaughlin, D. B. 1924, *The Astrophysical Journal*, 60, 22 [Cited on page 140.]

Meunier, N. 2021, arXiv e-prints, arXiv:2104.06072 [Cited on pages 55, 58, and 59.]

Meunier, N., & Lagrange, A. M. 2013, Astronomische Nachrichten, 334, 141 [Cited on page 59.]

Miller, N., & Fortney, J. J. 2011, *The Astrophysical Journal Letters*, 736, L29 [Cited on page 24.]

Moe, M., & Kratter, K. M. 2021, *Monthly Notices of Royal Astronomical Society*, 507, 3593 [Cited on page 26.]

Mordasini, C. 2020, *Astronomy & Astrophysics*, 638, A52 [Cited on page 124.]

Mordasini, C., Alibert, Y., & Benz, W. 2009, *Astronomy & Astrophysics*, 501, 1139 [Cited on page 21.]

Mordasini, C., Alibert, Y., Klahr, H., & Henning, T. 2012, *Astronomy & Astrophysics*, 547, A111 [Cited on pages 25 and 124.]

Mortier, A., Santos, N. C., Sousa, S. G., et al. 2013, *Astronomy & Astrophysics*, 557, A70 [Cited on page 25.]

Moulton, F. R. 1899, *The Astronomical Journal*, 20, 33 [Cited on page 2.]

Moutou, C., Loeillet, B., Bouchy, F., et al. 2006, *Astronomy & Astrophysics*, 458, 327 [Cited on page 98.]

Mugrauer, M., & Michel, K.-U. 2020, Astronomische Nachrichten, 341, 996 [Cited on page 113.]

—. 2021, Astronomische Nachrichten, 342, 840 [Cited on page 113.]

Naoz, S. 2016, Annual Review of Astronomy and Astrophysics, 54, 441 [Cited on page 22.]

Narayanan, A. 2010, , 45, 455 [Cited on page 1.]

Ohta, Y., Taruya, A., & Suto, Y. 2005, *The Astrophysical Journal*, 622, 1118 [Cited on page 140.]

Paardekooper, S. J., & Mellema, G. 2006, *Astronomy & Astrophysics*, 459, L17 [Cited on page 20.]

Pagano, I. 2013, Stellar Activity, ed. T. D. Oswalt & M. A. Barstow (Dordrecht: Springer Netherlands), 485–557 [Cited on page 58.]

Pasquini, L., Döllinger, M. P., Weiss, A., et al. 2007, *Astronomy & Astrophysics*, 473, 979 [Cited on page 25.]

Pecaut, M. J., & Mamajek, E. E. 2013, *The Astrophysical Journal Supplement Series*, 208, 9 [Cited on page 121.]

Pepe, F., Mayor, M., Galland, F., et al. 2002, *Astronomy & Astrophysics*, 388, 632 [Cited on pages 52 and 53.]

Pepe, F., Cristiani, S., Rebolo, R., et al. 2021, *Astronomy & Astrophysics*, 645, A96 [Cited on page 16.]

Pepper, J., Kane, S. R., Rodriguez, J. E., et al. 2020, *The Astronomical Journal*, 159, 243 [Cited on page 90.]

Perger, M., García-Piquer, A., Ribas, I., et al. 2017, *Astronomy & Astrophysics*, 598, A26 [Cited on page 55.]

Perruchot, S., Kohler, D., Bouchy, F., et al. 2008, in Society of Photo-Optical Instrumentation Engineers (SPIE) Conference Series, Vol. 7014, Ground-based and Airborne Instrumentation for Astronomy II, ed. I. S. McLean & M. M. Casali, 70140J [Cited on pages 16 and 65.]

Persson, C. M., Fridlund, M., Barragán, O., et al. 2018, *Astronomy & Astrophysics*, 618, A33 [Cited on page 86.]

Petigura, E. A., Marcy, G. W., Winn, J. N., et al. 2018, *The Astronomical Journal*, 155, 89 [Cited on page 26.]

Petrovich, C. 2015, *The Astrophysical Journal*, 805, 75 [Cited on page 22.]

Piddington, J. H. 1983, Astrophysics and Space Science, 90, 217 [Cited on page 58.]

Piskunov, N., & Valenti, J. A. 2017, *Astronomy & Astrophysics*, 597, A16 [Cited on page 86.]

Piskunov, N. E., & Valenti, J. A. 2002, *Astronomy & Astrophysics*, 385, 1095 [Cited on page 49.]

Pollacco, D. L., Skillen, I., Collier Cameron, A., et al. 2006, *Publications of the Astronomical Society of the Pacific*, 118, 1407 [Cited on page 81.]

Pollack, J. B., Hubickyj, O., Bodenheimer, P., et al. 1996, , 124, 62 [Cited on pages 17 and 18.]

Pont, F., Bouchy, F., Melo, C., et al. 2005, *Astronomy & Astrophysics*, 438, 1123 [Cited on pages 108 and 123.]

Povich, M. S., Giampapa, M. S., Valenti, J. A., et al. 2001, *The Astronomical Journal*, 121, 1136 [Cited on page 66.]

Queloz, D., Henry, G. W., Sivan, J. P., et al. 2001, *Astronomy & Astrophysics*, 379, 279 [Cited on pages 55, 57, 59, 60, and 65.]

Quirrenbach, A., Amado, P. J., Caballero, J. A., et al. 2014, in Society of Photo-Optical Instrumentation Engineers (SPIE) Conference Series, Vol. 9147, Ground-based and Airborne Instrumentation for Astronomy V, ed. S. K. Ramsay, I. S. McLean, & H. Takami, 91471F [Cited on pages 16 and 75.]

Rabus, M., Jordán, A., Hartman, J. D., et al. 2016, *The Astronomical Journal*, 152, 88 [Cited on pages 3, 26, and 99.]

Rafikov, R. R. 2005, *The Astrophysical Journal Letters*, 621, L69 [Cited on page 19.]

—. 2006, *The Astrophysical Journal*, 648, 666 [Cited on page 20.]

Rajpaul, V., Aigrain, S., Osborne, M. A., Reece, S., & Roberts, S. 2015, *Monthly Notices of Royal Astronomical Society*, 452, 2269 [Cited on page 57.]

Rasio, F. A., & Ford, E. B. 1996, Science, 274, 954 [Cited on pages 21 and 23.]

Raynard, L., Goad, M. R., Gillen, E., et al. 2018, *Monthly Notices of Royal Astronomical Society*, 481, 4960 [Cited on page 75.]

Reffert, S., Bergmann, C., Quirrenbach, A., Trifonov, T., & Künstler, A. 2015a, *Astronomy & Astrophysics*, 574, A116 [Cited on pages 25, 27, and 122.]

—. 2015b, *Astronomy & Astrophysics*, 574, A116 [Cited on pages 95 and 98.]

Ricker, G. R., Winn, J. N., Vanderspek, R., et al. 2015, Journal of Astronomical Telescopes, Instruments, and Systems, 1, 014003 [Cited on pages 4, 17, 33, 39, and 75.]

Robertson, P., & Mahadevan, S. 2014, *The Astrophysical Journal Letters*, 793, L24 [Cited on pages 57 and 59.]

Robertson, P., Roy, A., & Mahadevan, S. 2015, *The Astrophysical Journal Letters*, 805, L22 [Cited on pages 57 and 59.]

Robinson, S. E., Laughlin, G., Vogt, S. S., et al. 2007, *The Astrophysical Journal*, 670, 1391 [Cited on page 96.]

Rodriguez, J. E., Quinn, S. N., Huang, C. X., et al. 2019, *The Astronomical Journal*, 157, 191 [Cited on page 136.]

Rodriguez, J. E., Quinn, S. N., Zhou, G., et al. 2021, *The Astronomical Journal*, 161, 194 [Cited on pages 42 and 76.]

Rossiter, R. A. 1924, *The Astrophysical Journal*, 60, 15 [Cited on page 140.]

Roy, A., Chakraborty, A., Mahadevan, S., et al. 2016, in Society of Photo-Optical Instrumentation Engineers (SPIE) Conference Series, Vol. 9908, Ground-based and Airborne Instrumentation for Astronomy VI, ed. C. J. Evans, L. Simard, & H. Takami, 99086R [Cited on page 53.]

Ryabchikova, T., Piskunov, N., Kurucz, R. L., et al. 2015, , 90, 054005 [Cited on page 86.]

Saar, S. H., & Donahue, R. A. 1997, *The Astrophysical Journal*, 485, 319 [Cited on page 57.]

Safronov, V. S. 1960, Annales d'Astrophysique, 23, 979 [Cited on page 18.]

—. 1972, Evolution of the protoplanetary cloud and formation of the earth and planets. [Cited on page 17.]

Sahlmann, J., Lazorenko, P. F., Ségransan, D., et al. 2013, *Astronomy & Astrophysics*, 556, A133 [Cited on page 13.]

Sainsbury-Martinez, F., Wang, P., Fromang, S., et al. 2019, *Astronomy & Astrophysics*, 632, A114 [Cited on page 100.]

Santos, N. C., Israelian, G., & Mayor, M. 2001, *Astronomy & Astrophysics*, 373, 1019 [Cited on page 25.]

—. 2004a, *Astronomy & Astrophysics*, 415, 1153 [Cited on page 25.]

—. 2004b, *Astronomy & Astrophysics*, 415, 1153 [Cited on page 98.]

Santos, N. C., Mayor, M., Naef, D., et al. 2000, *Astronomy & Astrophysics*, 361, 265 [Cited on page 57.]

Santos, N. C., Adibekyan, V., Figueira, P., et al. 2017, *Astronomy & Astrophysics*, 603, A30 [Cited on page 125.]

Sarkis, P., Mordasini, C., Henning, T., Marleau, G. D., & Mollière, P. 2021, *Astronomy & Astrophysics*, 645, A79 [Cited on pages 124 and 125.]

Sarmiento, L. F., Reiners, A., Huke, P., et al. 2018, *Astronomy & Astrophysics*, 618, A118 [Cited on page 51.]

Saumon, D., Chabrier, G., & van Horn, H. M. 1995, *The Astrophysical Journal Supplement Series*, 99, 713 [Cited on pages 18 and 124.]

Schanche, N., Hébrard, G., Collier Cameron, A., et al. 2020, *Monthly Notices of Royal Astronomical Society*, 499, 428 [Cited on pages 42 and 136.]

Schlafly, E. F., & Finkbeiner, D. P. 2011, *The Astrophysical Journal*, 737, 103 [Cited on pages 90 and 119.]

Schlaufman, K. C. 2018, *The Astrophysical Journal*, 853, 37 [Cited on pages 107 and 125.]

Schlaufman, K. C., & Winn, J. N. 2013, *The Astrophysical Journal*, 772, 143 [Cited on pages 27 and 96.]

Schneider, J., Dedieu, C., Le Sidaner, P., Savalle, R., & Zolotukhin, I. 2011, *Astronomy & Astrophysics*, 532, A79 [Cited on page 123.]

Seager, S. 2010, Exoplanets [Cited on page 7.]

Seager, S., & Mallén-Ornelas, G. 2003, in Astronomical Society of the Pacific Conference Series, Vol. 294, Scientific Frontiers in Research on Extrasolar Planets, ed. D. Deming & S. Seager, 419–422 [Cited on page 10.]

Sebastian, D., Pedersen, P. P., Murray, C. A., et al. 2020, Development of the SPECULOOS exoplanet search project, doi:https://doi.org/10.1117/12.2563563 [Cited on page 81.]

See, T. J. J. 1896, *The Astronomical Journal*, 16, 17 [Cited on page 2.]

Sha, L., Huang, C. X., Shporer, A., et al. 2021, *The Astronomical Journal*, 161, 82 [Cited on pages 42 and 136.]

Sharma, R., & Chakraborty, A. G. 2021, Journal of Astronomical Telescopes, Instruments, and Systems, 7, 1 [Cited on pages 51, 84, and 113.]

Showman, A. P., & Guillot, T. 2002, *Astronomy & Astrophysics*, 385, 166 [Cited on page 23.]

Simola, U., Dumusque, X., & Cisewski-Kehe, J. 2018, Astronomy & Astrophysics [Cited on page 57.]

Simola, U., Dumusque, X., & Cisewski-Kehe, J. 2019, *Astronomy & Astrophysics*, 622, A131 [Cited on page 55.]

Sing, D. K., Pont, F., Aigrain, S., et al. 2011, *Monthly Notices of Royal Astronomical Society*, 416, 1443 [Cited on page 17.]

Sinukoff, E., Fulton, B., Scuderi, L., & Gaidos, E. 2013, *Space Science Reviews*, 180, 71 [Cited on page 14.]

Smalley, B., Anderson, D. R., Collier-Cameron, A., et al. 2012, *Astronomy & Astrophysics*, 547, A61 [Cited on page 99.]

Smith, A. M. S., Anderson, D. R., Bouchy, F., et al. 2013, *Astronomy & Astrophysics*, 552, A120 [Cited on page 99.]

Smith, J. C., Stumpe, M. C., Van Cleve, J. E., et al. 2012, *Publications of the Astronomical Society of the Pacific*, 124, 1000 [Cited on page 76.]

Socrates, A., Katz, B., Dong, S., & Tremaine, S. 2012, *The Astrophysical Journal*, 750, 106 [Cited on page 96.]

Soto, M. G., Díaz, M. R., Jenkins, J. S., et al. 2018, *Monthly Notices of Royal Astronomical Society*, 478, 5356 [Cited on page 75.]

Sousa, S. G., Santos, N. C., Israelian, G., Mayor, M., & Udry, S. 2011, *Astronomy & Astrophysics*, 533, A141 [Cited on page 25.]

Southworth, J. 2009, *Monthly Notices of Royal Astronomical Society*, 394, 272 [Cited on page 139.]

Southworth, J. 2011, Monthly Notices of the Royal Astronomical Society, 417, 2166 [Cited on page 97.]

Spiegel, D. S., Burrows, A., & Milsom, J. A. 2011, *The Astrophysical Journal*, 727, 57 [Cited on pages 107, 122, 123, and 138.]

Spiewak, R., Bailes, M., Barr, E. D., et al. 2018, *Monthly Notices of Royal Astronomical Society*, 475, 469 [Cited on page 14.]

Starovoit, E. D., & Rodin, A. E. 2017, Astronomy Reports, 61, 948 [Cited on page 14.]

Stassun, K. G., & Torres, G. 2016, *The Astrophysical Journal Letters*, 831, L6 [Cited on page 90.]

Stassun, K. G., Oelkers, R. J., Pepper, J., et al. 2018, *The Astronomical Journal*, 156, 102 [Cited on pages 78 and 132.]

Stassun, K. G., Oelkers, R. J., Paegert, M., et al. 2019, *The Astronomical Journal*, 158, 138 [Cited on pages v and 24.]

Stevens, D. J., & Gaudi, B. S. 2013, *Publications of the Astronomical Society of the Pacific*, 125, 933 [Cited on page 15.]

Stevens, D. J., Collins, K. A., Gaudi, B. S., et al. 2017, *The Astronomical Journal*, 153, 178 [Cited on pages 76 and 91.]

Struve, O. 1952, The Observatory, 72, 199 [Cited on page 2.]

Stumpe, M. C., Smith, J. C., Catanzarite, J. H., et al. 2014, Publications of the Astronomical Society of the Pacific, 126, 100 [Cited on page 76.]

Takeda, Y., Sato, B., & Murata, D. 2008, *Publications of the Astronomical Society of Japan*, 60, 781 [Cited on page 25.]

Temmink, M., & Snellen, I. A. G. 2023, *Astronomy & Astrophysics*, 670, A26 [Cited on page 26.]

Thompson, S. E., Fraquelli, D., Van Cleve, J. E., & Caldwell, D. A. 2016, Kepler Archive Manual, Kepler Science Document KDMC-10008-006 [Cited on page 79.]

Thompson, S. L. 1990, doi:10.2172/6939284 [Cited on page 124.]

Thorngren, D. P., & Fortney, J. J. 2018, *The Astronomical Journal*, 155, 214 [Cited on pages 23, 28, 75, and 124.]

Thorngren, D. P., Fortney, J. J., Murray-Clay, R. A., & Lopez, E. D. 2016, *The Astrophysical Journal*, 831, 64 [Cited on pages 24 and 124.]

Tilbrook, R. H., Burleigh, M. R., Costes, J. C., et al. 2021, *Monthly Notices of Royal Astronomical Society*, arXiv:2103.10302 [Cited on page 75.]

Tinetti, G., Drossart, P., Eccleston, P., et al. 2016, in Society of Photo-Optical Instrumentation Engineers (SPIE) Conference Series, Vol. 9904, Space Telescopes and Instrumentation 2016: Optical, Infrared, and Millimeter Wave, ed. H. A. MacEwen, G. G. Fazio, M. Lystrup, N. Batalha, N. Siegler, & E. C. Tong, 99041X [Cited on page 140.]

Toner, C. G., & Gray, D. F. 1988, *The Astrophysical Journal*, 334, 1008 [Cited on pages 58 and 61.]

Toomre, A. 1964, *The Astrophysical Journal*, 139, 1217 [Cited on page 18.]

Torres, G., Winn, J. N., & Holman, M. J. 2008, *The Astrophysical Journal*, 677, 1324 [Cited on page 90.]

Tremblin, P., Chabrier, G., Mayne, N. J., et al. 2017, *The Astrophysical Journal*, 841, 30 [Cited on page 100.]

Udry, S. 2010, in In the Spirit of Lyot 2010, ed. A. Boccaletti, E11 [Cited on pages 25, 108, and 123.]

Udry, S., Mayor, M., Queloz, D., Naef, D., & Santos, N. 2000, in From Extrasolar Planets to Cosmology: The VLT Opening Symposium, ed. J. Bergeron & A. Renzini, 571 [Cited on page 16.]

Ulmer-Moll, S., Lendl, M., Gill, S., et al. 2022, *Astronomy & Astrophysics*, 666, A46 [Cited on page 125.]

Valenti, J. A., Butler, R. P., & Marcy, G. W. 1995, *Publications of the Astronomical Society of the Pacific*, 107, 966 [Cited on page 85.]

Valenti, J. A., & Piskunov, N. 1996, *Astronomy and Astrophysics Supplement Series*, 118, 595 [Cited on page 86.]

van de Kamp, P. 1963, *The Astronomical Journal*, 68, 515 [Cited on page 2.]

—. 1969, *The Astronomical Journal*, 74, 757 [Cited on page 2.]

van den Bos, W. H. 1943, Monthly Notes of the Astronomical Society of South Africa, 2, 14 [Cited on page 2.]

van Dokkum, P. G. 2001, *Publications of the Astronomical Society of the Pacific*, 113, 1420 [Cited on page 50.]

Veras, D. 2016, Royal Society Open Science, 3, 150571 [Cited on page 28.]

Villaver, E., & Livio, M. 2009, *The Astrophysical Journal Letters*, 705, L81 [Cited on page 28.]

Villaver, E., Livio, M., Mustill, A. J., & Siess, L. 2014, *The Astrophysical Journal*, 794, 3 [Cited on page 28.]

Šubjak, J., Sharma, R., Carmichael, T. W., et al. 2020, *The Astronomical Journal*, 159, 151 [Cited on page 34.]

Wang, J., Fischer, D. A., Horch, E. P., & Huang, X. 2015, *The Astrophysical Journal*, 799, 229 [Cited on page 26.]

Wang, S., Jones, M., Shporer, A., et al. 2019, *The Astronomical Journal*, 157, 51 [Cited on page 136.]

Ward, W. R. 1997, , 126, 261 [Cited on page 20.]

Weidenschilling, S. J., & Marzari, F. 1996, *Nature*, 384, 619 [Cited on page 21.]

Weiss, L. M., Marcy, G. W., Rowe, J. F., et al. 2013, *The Astrophysical Journal*, 768, 14 [Cited on page 23.]

West, R. G., Hellier, C., Almenara, J. M., et al. 2016, *Astronomy & Astrophysics*, 585, A126 [Cited on page 99.]

White, R. J., Gabor, J. M., & Hillenbrand, L. A. 2007, *The Astronomical Journal*, 133, 2524 [Cited on page 65.]

Winn, J. N. 2008, Proceedings of the International Astronomical Union, 4, 99–109 [Cited on page 139.]

Wittenmyer, R. A., Butler, R. P., Tinney, C. G., et al. 2016, *The Astrophysical Journal*, 819, 28 [Cited on page 17.]

Wittenmyer, R. A., Clark, J. T., Trifonov, T., et al. 2021, *The Astronomical Journal*, 163, 82 [Cited on pages 42 and 136.]

Wolszczan, A., & Frail, D. A. 1992, *Nature*, 355, 145 [Cited on page 3.]

Wright, J. T. 2005, *Publications of the Astronomical Society of the Pacific*, 117, 657 [Cited on page 57.]

Wright, J. T. 2018, Radial Velocities as an Exoplanet Discovery Method, ed. H. J. Deeg & J. A. Belmonte (Cham: Springer International Publishing), 619–631 [Cited on page 7.]

Wright, J. T., & Eastman, J. D. 2014, *Publications of the Astronomical Society of the Pacific*, 126, 838 [Cited on page 52.]

Wright, J. T., Marcy, G. W., Howard, A. W., et al. 2012, *The Astrophysical Journal*, 753, 160 [Cited on pages 16 and 17.]

Wu, Y., & Lithwick, Y. 2011, *The Astrophysical Journal*, 735, 109 [Cited on page 22.]

Wu, Y., & Murray, N. 2003, *The Astrophysical Journal*, 589, 605 [Cited on page 22.]

Yee, S. W., Winn, J. N., Hartman, J. D., et al. 2023, The Astrophysical Journal Supplement Series, 265, 1 [Cited on page 26.]

Young, P. A., Highberger, J. L., Arnett, D., & Ziurys, L. M. 2003, *The Astrophysical Journal Letters*, 597, L53 [Cited on page 18.]

Zechmeister, M., Köhler, J., & Chamarthi, S. 2021, viper: Velocity and IP EstimatoR, ascl:2108.006 [Cited on page 85.]

Zechmeister, M., & Kürster, M. 2009, *Astronomy & Astrophysics*, 496, 577 [Cited on pages 87, 88, and 116.]

Zhou, G., Bayliss, D. D. R., Kedziora-Chudczer, L., et al. 2014, *Monthly Notices of Royal Astronomical Society*, 445, 2746 [Cited on page 17.]

Zhou, G., Bakos, G. Á., Bayliss, D., et al. 2019a, *The Astronomical Journal*, 157, 31 [Cited on pages 26 and 124.]

Zhou, G., Huang, C. X., Bakos, G. Á., et al. 2019b, *The Astronomical Journal*, 158, 141 [Cited on page 26.]

Ziegler, C., Tokovinin, A., Briceño, C., et al. 2020, *The Astronomical Journal*, 159, 19 [Cited on page 79.]